Alma Mater Studiorum · Università di Bologna

School of Universe Sciences
Department of Physics and Astronomy
Master's Degree in Astrophysics and Cosmology

Aging Galaxies in a Young Universe: Testing ΛCDM with JWST Observations of Quiescent Galaxies

Supervisor:
Prof. Michele Ennio Maria Moresco

Co-supervisor:
Prof. Sirio Belli
Elena Tomasetti

Presented by:
Alessia De Nigris

Academic Year 2024/2025

Contents

Bibliography

Abstract

Recent JWST observations have unveiled a surprising population of massive, quiescent galaxies at redshifts $z \sim 3-5$, whose ages and formation times challenge the conventional ΛCDM cosmological model. This tension, often referred to as the "impossibly early galaxy" problem, raises fundamental questions about how and when the first massive galaxies assembled in the Universe.

This thesis investigates the impact of the full-spectral fitting modeling assumptions, especially the role of age priors, on the inferred physical properties of these distant galaxies. By relaxing cosmological age constraints, the analysis explores whether observed star formation histories (SFHs) remain compatible with ΛCDM predictions or if they suggest alternative cosmological scenarios.

The results reveal a complex picture: while some galaxies show consistent ages and SFHs across different parameterizations, others display a variety of SFHs that produce indistinguishable spectra yet imply widely different stellar ages. When age priors are removed, some of these ages exceed the age of the Universe at the observed redshift. These results raise potential concerns about interpreting some inferred properties as being in tension with the ΛCDM framework. Nevertheless, it is noteworthy that the median stellar ages remain remarkably stable across different models, reinforcing their reliability for cosmological studies.

To clarify these findings, simplified theoretical models are developed to probe the degeneracies between old and young stellar populations in spectral fits. This work highlights the critical importance of modeling choices in interpreting early galaxy observations and contributes to the ongoing debate about massive galaxy formation in the young Universe. Moreover, it shows that detecting massive, passive galaxies at high redshift is promising, as younger stars reduce ambiguities and yield robust constraints, making them valuable probes of the ΛCDM model.

Thesis Outline

Recent observational advances, particularly those enabled by the James Webb Space Telescope (JWST), have led to the discovery of massive evolved galaxies at redshifts as high as $z \sim 3-5$ and even higher, indicating that these systems were already in place less than a billion years after the Big Bang. These findings have sparked considerable debate within the astrophysical community, as they appear to challenge the predictions of the standard cosmological model, ΛCDM. In particular, the "impossibly early galaxy problem" refers to the apparent discrepancy between the observed abundance and maturity of early massive galaxies and the hierarchical growth of structure predicted by ΛCDM. Although the model successfully explains a wide range of large-scale cosmological observations, these tensions have raised important questions about galaxy formation timescales, SFHs, and the underlying assumptions of stellar population synthesis (SPS) models.

This work builds upon high-quality, high signal-to-noise ratio (SNR) data from JWST, combining spectroscopic and photometric observations to enable detailed full-spectral fitting procedures that derive stellar ages and SFHs of high-redshift galaxies. A crucial assumption embedded in the `Bagpipes` fitting code, commonly used in these analyses, is that inferred stellar ages cannot exceed the age of the Universe at the observed redshift. Although this cosmological age constraint is physically well motivated, its influence on the resulting age estimates and SFHs remains insufficiently explored. To address this limitation, the `Bagpipes` code has been modified to relax this constraint, allowing stellar ages up to 5 Gyr even for galaxies observed at $z \sim 3-5$.

Using this modified tool, the thesis investigates whether current methods for deriving galaxy physical properties, particularly stellar ages and masses, adequately describe early galaxy evolution or inadvertently contribute to the observed tensions. This is accomplished through a detailed analysis of a sample of quiescent galaxies at $3 \lesssim z \lesssim 5$,

employing both Lick index measurements and full-spectral fitting techniques.

Full-spectral fitting is performed by exploring a variety of SFH models —including parametric and nonparametric forms — and testing different assumptions on stellar ages and other key parameters. This comprehensive approach enables assessment of the robustness of derived ages and masses, as well as potential biases embedded in typical fitting techniques.

To better interpret the results and explore spectral degeneracies, a set of simple theoretical models has been developed. These models clarify the degeneracies between young and old stellar populations, and their effects on the recovery of physical parameters from observed spectra.

The thesis is organized as follows:

Chapter 1 provides the theoretical background for the study. It presents the ΛCDM cosmological model and the standard picture of galaxy formation and evolution, and outlines the current observational challenges—often referred to as "ΛCDM breakers"—that motivate this work.

Chapter 2 describes the methodologies used for the analysis. This includes an overview of stellar population synthesis models, the methods for estimating galaxy ages, and the description of the code used to perform the full-spectral fitting (`Bagpipes`), including its various parameters and how it has been modified in order to have the age as a fully free parameter.

Chapter 3 presents the dataset under investigation. This section describes the selection criteria for the sample analyzed, which consists of quiescent galaxies observed with JWST, chosen based on their spectral and photometric properties indicative of suppressed star formation activity.

Chapter 4 reports the main results of the thesis. Two complementary approaches are adopted to derive stellar ages and metallicities: the classical Lick index method, which enables an initial selection in age and metallicity, and a more comprehensive approach based on full-spectral fitting, where particular emphasis is placed on exploring variations in the SFH. The chapter ends with a plot illustrating the ages obtained from different SFH models as a function of redshift, allowing a direct comparison with the expected evolution predicted by the ΛCDM cosmological model. The results are compared and critically assessed in the context of their implications for early galaxy evolution.

Chapter 5 discusses and interprets the findings. Using simple theoretical models, the analysis investigates the degeneracies in star formation histories and explores whether apparently old stellar ages could be mimicked by complex SFHs, thus alleviating the tension with cosmological expectations.

Chapter 6 summarizes the conclusions of the study, highlighting the spectral degeneracies and model-dependent uncertainties that affect the inferred ages and masses of high-redshift galaxies. The chapter concludes that the issue remains open and outlines the need for more advanced modeling techniques and future JWST-like observations.

Chapter 1

Introduction

1.1 ΛCDM Model

The expansion of the Universe is one of the most fundamental discoveries in modern cosmology. In the late 1920s, Edwin Hubble observed that distant galaxies are moving away from us, and their recession velocity is proportional to their distance, providing the first evidence that the Universe is expanding (Dodelson and Schmidt, 2024).

To quantify this expansion, it is useful to introduce the concept of spectroscopic redshift, defined as:

$$z = \frac{\lambda_{\text{observed}} - \lambda_{\text{emitted}}}{\lambda_{\text{emitted}}} \tag{1.1}$$

where λ_{emitted} is the wavelength of light emitted by a galaxy and $\lambda_{\text{observed}}$ is the wavelength we measure on Earth. An astrophysical object might experience a redshift or blueshift depending on its radial velocity with respect to the observer, but on cosmological scales the redshift measures how much light has been stretched due to the expansion of space.

For objects moving at speeds much less than the speed of light, the redshift can be approximated by the Doppler formula:

$$z \approx \frac{v}{c} \tag{1.2}$$

where v is the recession velocity and c is the speed of light.

Hubble found empirically that the recession velocity is proportional to the distance r of the galaxy (Hubble, 1929):

$$v = H_0\, r \tag{1.3}$$

where H_0 is the Hubble constant.

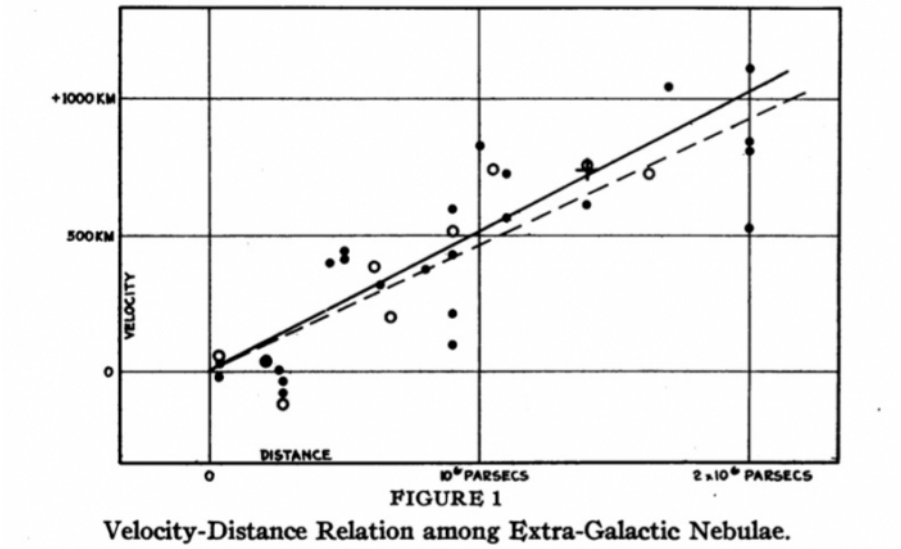

Figure 1.1: Original diagram published by Edwin Hubble in 1929, showing the relationship between the distance of galaxies and their radial velocity, derived from redshift measurements. This plot provided the first observational evidence for the expansion of the Universe (Hubble, 1929).

Combining the two expressions, for small redshifts, the redshift is approximately related to the distance by:

$$z \approx \frac{H_0\, r}{c} \tag{1.4}$$

It is important to note that this linear relation holds only for nearby galaxies (small z). At higher redshifts, the expansion of the Universe is better described by relativistic cosmology, and the simple Doppler interpretation is no longer valid.
Measuring the redshift of an object is relatively straightforward, but the real challenge lies in determining its distance when its intrinsic brightness is unknown. One of the

most widely used methods is the "standard candle" approach, which relies on classes of objects with a well-defined intrinsic brightness. In this way, any difference in their apparent brightness is due to their different distances from us. A classic example is Cepheid variable stars, whose intrinsic brightness is closely related to their pulsation period. The Hubble Space Telescope (HST) has measured the periods and fluxes of thousands of Cepheid variables in 42 galaxies hosting Type Ia Supernovae, reaching distances up to 40 Mpc. This has enabled astronomers to establish a robust local calibration of the cosmic distance ladder. In the most recent and comprehensive analysis, Riess et al. (2022) combined these Cepheid measurements with several independent geometric distance anchors —- including parallaxes from Gaia, megamasers in NGC 4258, and eclipsing binaries in the LMC —- to determine the absolute magnitude of Type Ia Supernovae.

Using this calibration, the SH0ES team extended the distance ladder to about 400 Mpc by including hundreds of SNe Ia from the Pantheon+ compilation. The result is a precise local measurement of the Hubble constant:

$$H_0 = 73.04 \pm 1.04 \text{ km s}^{-1} \text{ Mpc}^{-1},$$

with a total uncertainty of 1.4%. This value is in significant (5σ) tension with the prediction from Planck CMB data assuming a ΛCDM cosmology, which yields $H_0 \approx 67.4$ $\text{km s}^{-1} \text{ Mpc}^{-1}$.
Furthermore, observations of distant Type Ia supernovae (Perlmutter et al., 1999; Riess et al., 1998) revealed that the expansion of the Universe is not slowing down, as previously expected, but accelerating. This surprising discovery implied the existence of a new, repulsive component in the Universe's energy budget, commonly referred to as dark energy.

This accelerated expansion is well described by the Lambda Cold Dark Matter (ΛCDM) model, which has become the prevailing cosmological paradigm. It is based on the Cosmological Principle, which asserts that, on sufficiently large scales, the Universe is both homogeneous and isotropic. Homogeneity is the property of being identical everywhere in space, while isotropy is the property of looking the same in every direction(Peters Coles, 2003).
The ΛCDM model relies on General Relativity and assumes that the Universe is composed of: radiation 10^{-5}%, ordinary baryonic matter 4%, cold dark matter (CDM) 26%, and dark energy (Λ) 70% (Collaboration, 2020). Dark energy, represented by the cosmological constant (Λ), is responsible for the accelerated expansion of the Universe,

as confirmed by observations of distant supernovae and cosmic microwave background (CMB) radiation.

1.1.1 Einstein Field Equations

We briefly introduce here the formalisms at the base of the evolution of the Universe, following how it is discussed Moscardini (2023).
To describe the evolution of the Universe within the framework of General Relativity, it is necessary to consider the Einstein field equations, which relate the curvature of spacetime to its matter and energy content.
These equations form the theoretical basis of modern cosmology:

$$R_{ij} - \frac{1}{2} g_{ij} R - \Lambda g_{ij} = \frac{8\pi G}{c^4} T_{ij}, \tag{1.5}$$

where g_{ij} is the metric tensor, T_{ij} is the energy-momentum tensor, R_{ij} and R are the Ricci tensor and the Ricci scalar, respectively. T_{ij} describes the distribution of matter. For a perfect fluid, with pressure p and energy density ρ, it can be expressed as:

$$T_{ij} = (p + \rho c^2) U_i U_j - p g_{ij}. \tag{1.6}$$

The vector U_i is the fluid four-velocity:

$$U_i = g_{ij} U^j = g_{ij} \frac{dx^k}{ds}, \tag{1.7}$$

where $x^k(s)$ is the trajectory in space-time followed by the particle. The first term of the energy-momentum tensor describes the contribution of the energy density, and the second one of the pressure.

The strength of the Einstein equations lies in their ability to link the geometry of space-time, described by the metric tensor g_{ij}, to the distribution of matter and energy, encoded in the energy-momentum tensor T_{ij}. Equation 1.5 represents a formulation of Einstein's original field equations (1916) that does not include the cosmological constant Λ, as at the time a static Universe was widely assumed. However, such a static solution within General Relativity would require both negative energy density and pressure; conditions that imply a physically unrealistic fluid. To reconcile the theory with the idea of a static Universe, Einstein introduced an additional term, Λ, in 1917. Although initially conceived as a correction, this term has since become a fundamental component in modern cosmology, now interpreted as the energy density of the vacuum.

Because General Relativity is a geometrical theory, it is necessary to investigate the geometrical properties of homogeneous and isotropic space. The most general space-time metric describing a Universe in which the Cosmological Principle is obeyed is :

$$ds^2 = (cdt)^2 - a(t)^2[\frac{dr^2}{1-Kr^2} + r^2(d\theta^2 + sin^2\theta d\phi^2)], \tag{1.8}$$

called the Friedmann–Lemaître–Robertson–Walker (FLRW) metric where r, θ, and ϕ are spherical polar coordinates, t is the proper time, $a(t)$ is the cosmic scale factor or the expansion factor, K is the curvature parameter: 0 (flat space), $+1$ (positive curvature, spherical space) and -1 (negative curvature, hyperbolic space).

1.1.2 Friedmann Equations

Once the Einstein field equations are established, they can be solved under the assumption of homogeneity and isotropy (perfect fluid), leading to the Friedmann equations:

$$\ddot{a} = -\frac{4}{3}\pi G(\tilde{\rho} + 3\frac{\tilde{p}}{c^2})a \tag{1.9}$$

$$\dot{a} + Kc^2 = \frac{8}{3}\pi G\tilde{\rho}a^2, \tag{1.10}$$

where $\tilde{p}$ is the effective pressure

$$\tilde{p} = p - \frac{\Lambda c^4}{8\pi G} \tag{1.11}$$

and $\tilde{\rho}$ is the effective density

$$\tilde{\rho} = \rho + \frac{\Lambda c^2}{8\pi G}, \tag{1.12}$$

both dependent on Λ; $\dot{a}$ and $\ddot{a}$ are the first and second derivatives in time of the cosmic scale factor, and G is the gravitational constant. We can observe that H, being the ratio of the recession velocity and the proper distance between two points in the space-time, can be expressed as $H = \frac{\dot{a}}{a}$.
Let's introduce the density parameter

$$\Omega := \frac{\rho}{\rho_{crit}}, \tag{1.13}$$

and the corresponding value at t_0, today

$$\Omega_0 := \frac{\rho_0}{\rho_{crit,0}}, \tag{1.14}$$

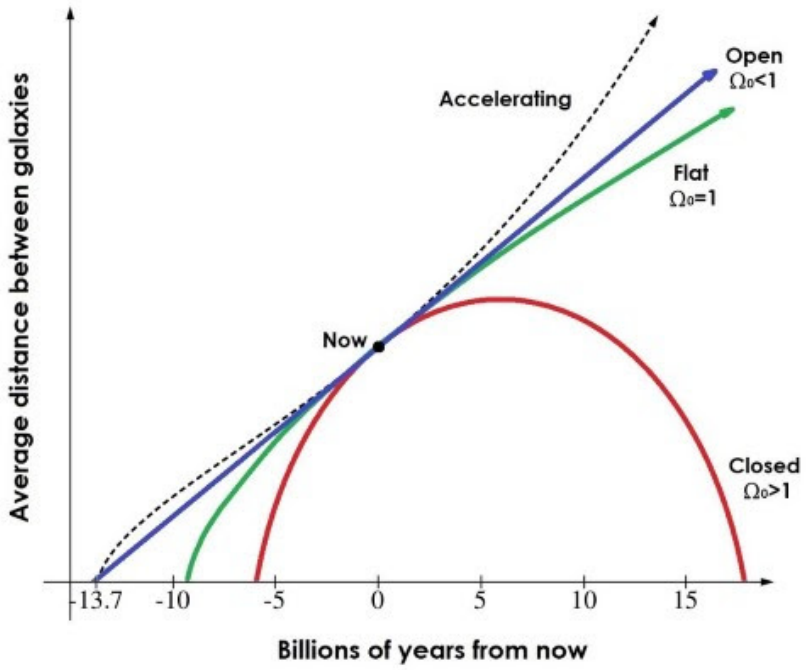

Figure 1.2: Evolution of the Universe's expansion over time, depending on the total density parameter Ω_0, which reflects the amount of matter and energy in the Universe. Image credit by NASA.

with $\rho_{crit} := \frac{3H^2}{8\pi G}$ and $\rho_{crit_0} := \frac{3H_0^2}{8\pi G}$, $H_0 = \frac{\dot{a}_0}{a_0}$.
It's possible to relate the curvature of the space to the density parameter using the second Friedmann equation 1.10 and the quantity just defined above

$$H_0^2(1 - \Omega_{0,tot}) = -\frac{Kc^2}{a_0^2}, \tag{1.15}$$

where $\Omega_{0,tot} := \sum \Omega_{0,i}$ (matter and dark energy component), so for $K = -1$ $\Omega_{0,tot} < 1$ (closed universe), for $K = 0$ $\Omega_{0,tot} = 1$ (flat universe), for $K = +1$ $\Omega_{0,tot} > 1$ (open universe). Starting from the first Friedmann equation with the assumption that p, the total pressure, is dominated today by Λ (p_M is negligible) and instead ρ, the total density, is $\rho_\Lambda + \rho_M$, one obtains:

$$\ddot{a} = -aH^2\frac{\Omega_M}{2} + aH^2\Omega_\Lambda, \tag{1.16}$$

with $\Omega_M = \frac{\rho_M}{\rho_{crit}}$ and$\Omega_\Lambda = \frac{\Lambda c^2}{3H^2}$. In order to have accelerated expansion, $\ddot{a} > 0$ is required: this condition is satisfied if $\Omega_\Lambda > \frac{\Omega_M}{2}$.

There are cases where it is possible to solve the Friedmann equations analytically, but in the most general case:

$$H^2(z) = H_0^2(1+z)^2[1 - \sum_i \Omega_{0,w_i} + \sum_i \Omega_{0,w_i}(1+z)^{1+3w_i}] = H_0^2 E^2(z) \tag{1.17}$$

with $1 + z = \frac{a_0}{a(t)}$.
The age of the Universe as a function of the redshift depends on the value of the Hubble constant at that time and on the cosmological model:

$$t(z) = \int_z^{+\infty} \frac{1}{H_0(1+z)^3[1 - \sum_i \Omega_{0,w_i} + \sum_i \Omega_{0,w_i}(1+z)^{1+3w_i}]} dz = \int_z^{+\infty} \frac{1}{H_0 E(z)(1+z)} dz. \tag{1.18}$$

Considering the approximation of the Universe as a perfect fluid (realistic for the Universe on a large scale), one can define the equation of state $p = \omega\rho c^2$ with $0 < \omega < 1$, the Zel'dovich range. For each component i of the fluid, ω_i assumes a different value.

At z=0, so today

$$t_0 = \frac{1}{H_0} \int_0^{+\infty} \frac{1}{E(z)(1+z')} dz' \tag{1.19}$$

The Lookback Time is the temporal distance of an event with respect to us (z=0):

$$t_{LB} := t_0 - t(z). \tag{1.20}$$

1.1.3 The flat ΛCDM model

The currently accepted cosmological model is the spatially flat ($k = 0$) ΛCDM model, in which the total energy density of the Universe exactly equals the critical density, implying a flat geometry ($\Omega = 1$) according to General Relativity. In this framework, the Universe is composed of matter (both baryonic and dark), a cosmological constant (Λ) associated with dark energy, and a negligible contribution from radiation at the present epoch. The best-fit values from multiple observational probes are approximately $\Omega_{0,M} \sim 0.3$, $\Omega_{0,\Lambda} \sim 0.7$, and $\Omega_{0,R} \sim 10^{-5}$, satisfying the flatness condition $\Omega_{0,M} + \Omega_{0,\Lambda} + \Omega_{0,R} \approx 1$.

Evidence supporting spatial flatness comes from several independent observations, including the position of the first acoustic peak in the cosmic microwave background (CMB) angular power spectrum (e.g. Collaboration (2020)), the large-scale structure of galaxy distributions as traced by baryon acoustic oscillations (e.g. Alam et al. (2017),

and distance measurements from type Ia supernovae (e.g. Brout et al. (2022)). These observational results are consistent with a spatially flat Universe and provide strong support for the ΛCDM model.

From a theoretical standpoint, the flatness condition has deep implications. Without a dynamical mechanism, such precise tuning of the energy density in the early Universe would appear unnatural, since any small deviation from the critical density would have been dramatically amplified over cosmic time. This is known as the flatness problem. Inflationary theory offers a natural solution by positing a brief epoch of exponential expansion in the early Universe, which would have diluted any initial spatial curvature, effectively driving the geometry towards flatness. This inflationary prediction is in excellent agreement with CMB data, which constrain the curvature parameter to $|\Omega| < 0.005$ (Collaboration, 2020), fully consistent with flatness.

1.2 Galaxy formation and Evolution

Building on the ΛCDM framework, this section explores galaxy formation and evolution, focusing on the role of dark matter halos and baryonic matter. Simulations show that structure formation follows a hierarchical evolution, known as the bottom-up scenario, where low-mass systems grow into high-mass systems by accreting matter. Before delving into the physical processes driving structure formation, it is useful to briefly introduce the main types of galaxies and how they are classified.

1.2.1 Galaxy Classification

The first systematic attempt to classify galaxies was introduced by Edwin Hubble in 1926, who proposed a morphological sequence—commonly known as the Hubble tuning fork diagram in which galaxies are divided into ellipticals, spirals, and lenticulars. Spiral galaxies are further subdivided into normal spirals (S) and barred spirals (SB), depending on the presence of a central bar structure. Although Hubble initially interpreted this sequence as indicative of an evolutionary progression, it is now primarily used to classify galaxies according to their observed morphology. In addition to these categories, Hubble also recognized a class of irregular galaxies (Irr), which do not fit into the regular morphological types and often show chaotic structures. Elliptical and lenticular galaxies are commonly referred to as early-type galaxies (ETGs), while spirals and irregulars are grouped as late-type galaxies (LTGs). This classification reflects general physical prop-

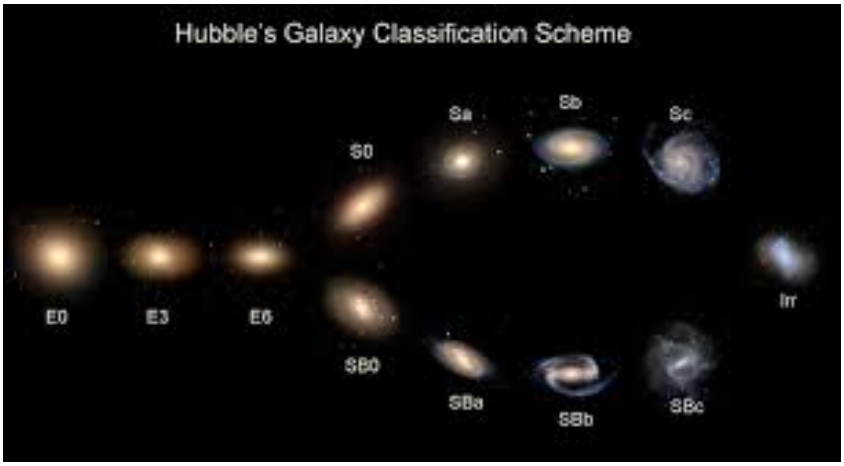

Figure 1.3: The Hubble tuning fork. Image credit: NASA/ESA

erties: ETGs tend to have smooth light profiles, older stellar populations, higher average stellar masses, and little or no star formation, whereas LTGs typically exhibit disk-like structures, ongoing star formation, bluer colors, and lower average stellar masses.

Although the Hubble morphological classification remains a valuable descriptive framework, it is now considered insufficient to fully characterize galaxy properties. Consequently, modern astrophysical studies increasingly rely on classification schemes based on physical parameters such as stellar mass, color, and star formation rate, which offer a more comprehensive understanding of galaxy evolution.

One of the most widely used methods is based on the observed bimodality in galaxy populations. When plotted in the color–magnitude or color–mass diagram, galaxies occupy two main regions: the blue cloud, where actively star-forming galaxies reside, and the red sequence, dominated by quiescent galaxies with older stellar populations. The intermediate green valley is thought to host galaxies in transition from star-forming to quiescent states.

This bimodal distribution reflects the underlying differences in star formation activity, gas content, and stellar population ages, and has become a key framework for understanding galaxy evolution (Baldry et al., 2004; Schawinski et al., 2014).

Kinematic analyses have introduced an additional classification scheme, particularly relevant for early-type galaxies, distinguishing between fast and slow rotators. Fast rotators exhibit ordered rotational support and often display disk-like features, while slow ro-

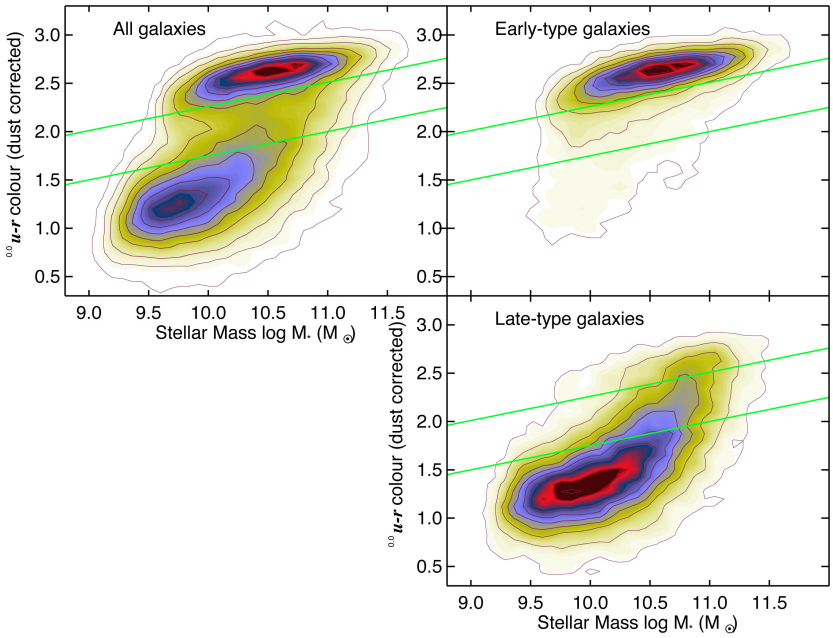

Figure 1.4: Bimodal distribution of galaxies in the color–magnitude diagram, showing a clear segregation into the "blue cloud," "green valley," and "red sequence". Image credit by Schawinski et al. (2014).

tators are dominated by random stellar motions and are typically more massive and spheroidal, reflecting different formation histories and merger events (Cappellari, 2016; Emsellem et al., 2011).

Moreover, with the advent of large spectroscopic and photometric surveys, spectral energy distribution (SED)- based classifications have become increasingly important. These methods allow galaxies to be categorized according to their star formation rates, stellar population properties, and the presence of active galactic nuclei (AGN), often using full SED fitting or emission-line diagnostics (Walcher et al., 2011).

In modern astrophysics, no single classification scheme is sufficient to fully capture the diversity of galaxy properties. Instead, a multi-dimensional approach (combining morphological, photometric, spectroscopic, and kinematic information) is commonly adopted to better understand galaxy formation and evolution across cosmic time.

Interestingly, while the ΛCDM model predicts a hierarchical growth of structures—where small systems merge to form larger ones, observations suggest that star formation in galaxies follows a different trend, often referred to as the downsizing scenario (Cowie

et al., 1996; Thomas et al., 2005; Cimatti et al., 2006). In this framework, the most massive galaxies appear to have formed their stars earlier and more rapidly than less massive ones, which continue forming stars at later times. This apparent anti-hierarchical behavior adds complexity to the interpretation of galaxy evolution and highlights the need for physically motivated classification schemes.

Having outlined the main galaxy classification schemes and their connection to observable properties, we now turn our attention to the physical processes that govern the formation of these structures within a cosmological framework. In this scenario, galaxies form as gas collapses and cools within dark matter (DM) halos, which themselves arise from the gravitational instability of DM and the growth of primordial perturbations in the matter density distribution of the Universe. Understanding the properties of DM halos thus requires a deep knowledge of the nature of dark matter. In the following, we will present the basic concepts related to dark matter and its properties, following the discussion in Cimatti et al. (2020).

1.2.2 Dark Matter and Structure Formation

Dark matter (DM) refers to the form of matter that does not emit, absorb, or reflect electromagnetic radiation, and is therefore invisible to traditional astronomical observations. A wide range of evidence — including galaxy rotation curves, gravitational lensing, and the cosmic microwave background (CMB) — indicates that DM constitutes most of the matter content in the Universe. Importantly, it must be non-baryonic, as it does not interact electromagnetically.

The nature of DM particles, especially their mass and velocity, influences the formation of large-scale structures. This leads to a classification into:

- **Cold Dark Matter (CDM)**: composed of massive, slow-moving particles that can cluster efficiently, forming structures from small to large scales (*bottom-up* scenario).
- **Hot Dark Matter (HDM)**: made of light, fast-moving particles that erase small-scale structures due to free-streaming, leading to a *top-down* formation scenario.

Numerical simulations show that CDM better reproduces the observed structure of the Universe. In particular, the presence of small-scale halos and the pattern of galaxy clustering are consistent with the CDM scenario, which forms the basis of the standard

ΛCDM cosmological model.

The collapse of a pregalactic gas into DM halos is one of the two fundamental requirements for the formation of luminous structures in the Universe. The second requirement is that the gas must be able to cool rapidly enough to condense into dense clouds, eventually forming the first stars. Both analytical estimates and numerical simulations indicate that the first luminous objects formed at redshifts $z \sim 20$–30, inside DM halos with typical masses of $\sim 10^6 M_\odot$—so-called "minihalos".

1.2.3 Halo Mass Function (HMF) and Stellar Mass Function (SMF)

Dark matter (DM) halos are characterized by significant substructure, primarily in the form of subhalos (smaller DM halos that orbit within larger halos). The subhalos of massive galactic halos can host satellite galaxies.

The properties of subhalos within a given DM halo are determined by both the characteristics of the subhalo population at the time of accretion and their subsequent evolution. Once subhalos fall into their host halos, they evolve through processes such as dynamical friction, tidal stripping, and interactions with other subhalos.

A key property of the DM subhalo population is its mass function, which can be estimated using cosmological N-body simulations and analytic methods based on the extended Press-Schechter formalism. For a given halo at a specific time t:

- The unevolved subhalo mass function refers to the mass distribution of subhalos at the time of accretion.
- The evolved subhalo mass function accounts for the mass distribution of subhalos at time t.

The evolved mass function (see Figure 1.5) differs from the unevolved one due to tidal stripping, which leads to the complete disruption or mass loss of some subhalos.

Cosmological N-body simulations show that the unevolved subhalo mass function is universal, meaning it is independent of host halo mass and redshift. The number of subhalos per unit logarithmic mass can be parametrized as:

$$\frac{dn}{dn\mu} = \gamma \mu^{\alpha} e^{-\beta \mu^{\omega}}, \tag{1.21}$$

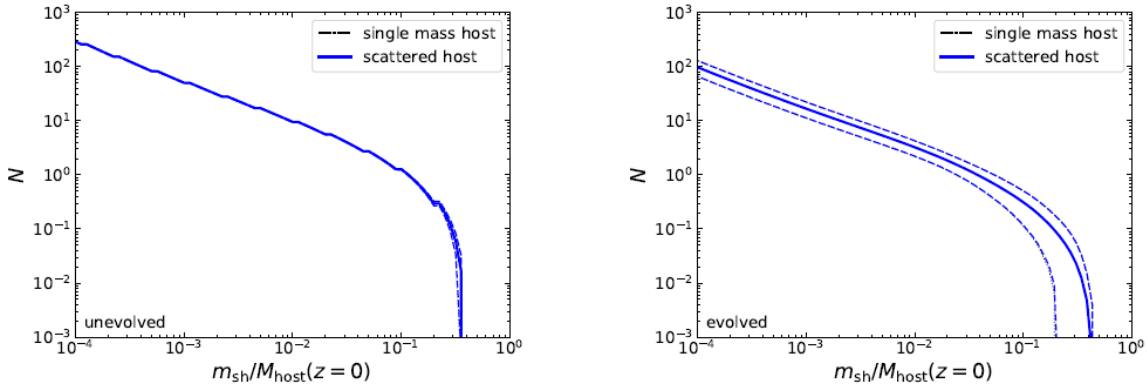

Figure 1.5: The unevolved (left) and evolved (right) subhalo mass functions are shown by combining contributions from host halos with $M_{200}(z=0) = 1.30 \pm 0.30\, M_\odot$. In each panel, the case of a single-mass host is also plotted with a dash-dotted line, which is nearly indistinguishable from the solid line that includes the effects of host mass scatter. Work done by Hiroshima et al. (2023).

where $\mu := \frac{M_{\rm sub}}{M_{\rm host}}$ is the ratio between the subhalo mass and the host halo mass, and α, β, γ, and ω are dimensionless parameters, with reference values $\alpha \sim -0.9$, $\beta \sim 6$, $\gamma \sim 0.2$, and $\omega \sim 3$. The evolved subhalo mass function can be described by the same functional form as the unevolved function, with the normalization γ decreasing with time.

The Halo Mass Function (HMF), which can be estimated analytically using the Press-Schechter formalism, evaluates the number of halos more massive than a given mass M:

$$\frac{dn}{dM}(M) = 2\frac{\overline{\rho}}{M}\left|\frac{dP}{dM}\right| = \sqrt{\frac{2}{\pi}}\frac{\overline{\rho}\delta_c}{M^2\sigma_k}e^{-\frac{\delta_c^2}{2\sigma_k^2}}\left|\frac{d\ln\sigma_k}{d\ln M}\right|. \tag{1.22}$$

This function decreases with mass as M^{-2}, indicating that there are more halos of smaller mass compared to those with larger mass. The function depends on $\overline{\rho}$, the mean density, δ_c, the critical overdensity that defines the contrast between the halo density and the average density of the Universe, and σ_k, the mass variance of the halos.

The mass distribution of CDM halos varies with the redshift as shown in Figure 1.6. The typical mass of cold dark matter halos increases over time due to the hierarchical merging of smaller halos into larger ones. The growth is faster in the early Universe when the matter density is high and slows down later due to the expansion of the Universe. After clarifying the mass density profile of CDM, it may be useful, for completeness, to also consider the stellar mass density profile, so that the two can be compared and their

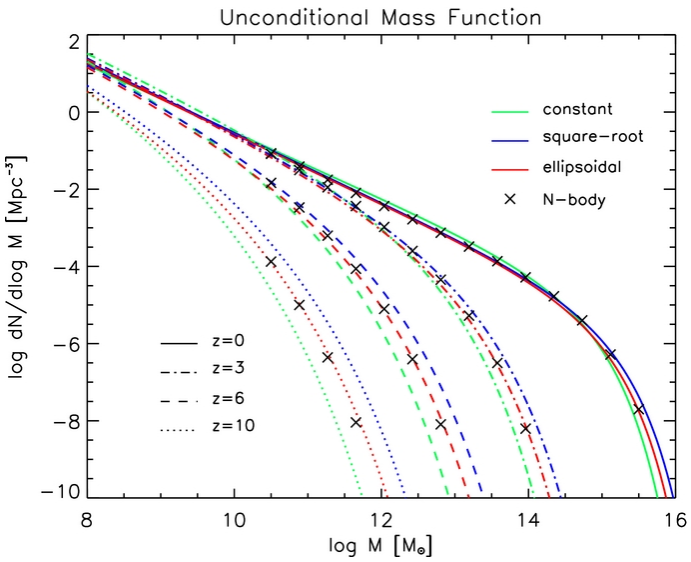

Figure 1.6: Unconditional mass function as a function of halo mass at different redshifts, for the constant (green), square-root (blue), and ellipsoidal (red) barriers. Crosses illustrate the outcomes of N-body simulations (fit to Tinker et al. 2008). A standard cold DM power spectrum has been adopted. This study is reported in (Lapi et al., 2013).

differences highlighted.

A double Schechter function can successfully reproduce the stellar mass function (SMF) of all galaxy types:

$$\Phi(M)dM = \left[\Phi_1^* \left(\frac{M}{M^*}\right)^{\alpha_1} + \Phi_2^* \left(\frac{M}{M^*}\right)^{\alpha_2}\right] e^{-\frac{M}{M^*}} d\left(\frac{M}{M^*}\right). \tag{1.23}$$

A single Schechter function well reproduces the SMF of the two main galaxy types (see Figure 1.7). In particular, the high-mass end is dominated by early-type galaxies (ETGs), while star-forming galaxies (SFGs) contribute more at smaller masses. The general features of the SMF, the relative contributions of ETGs and SFGs, and the absence of galaxies with $\log(M^*/M_\odot) > 12$ are critical tests for galaxy formation models.

An interesting comparison is between the SMF of present-day galaxies and the HMF predicted at $z = 0$ (see Figure 1.8). Considering for simplicity a model in which each halo hosts one galaxy, the typical halo mass $M_{\rm vir}$ corresponding to a given stellar mass $M_{\rm star}$ can be inferred by matching the SMF and the HMF, i.e., by finding the value of $M_{\rm vir}$ such that the number density of the HMF equals the number density of the SMF

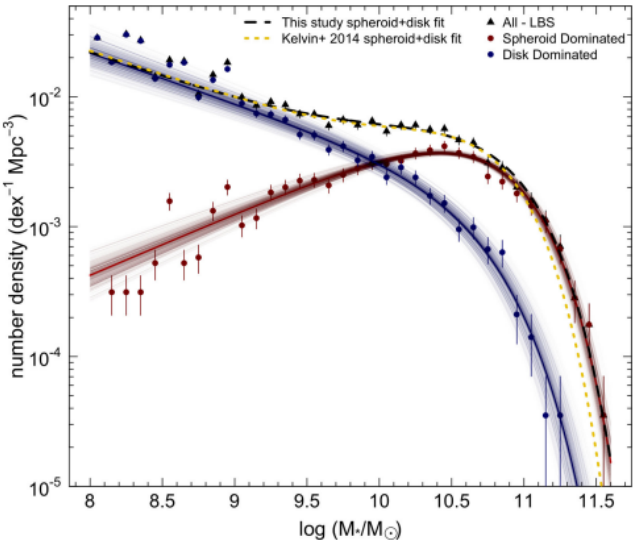

Figure 1.7: The stellar mass function (yellow line), and the two dominant components: spheroids (red) and disks (blue). Work done by (Moffett et al., 2016).

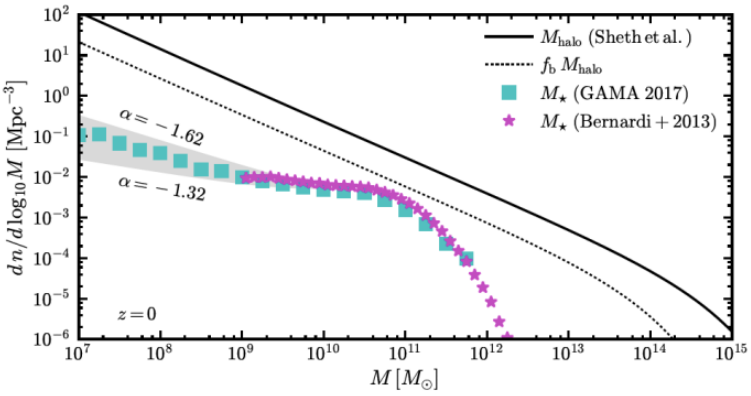

Figure 1.8: The number density of objects is shown as a function of their mass. Colored points represent galaxies. The solid line shows the predicted number of dark matter halos. The dotted line indicates the expected number of galaxies if all the normal matter associated with each dark matter halo were converted into stars. From the review by Bullock and Boylan-Kolchin (2017).

at mass $M_{\rm star}$. At a given number density, the halo mass is much higher than the stellar mass. This is primarily due to the fact that there is much more DM than baryonic matter in the Universe, so it is useful to rescale the HMF by multiplying it by $f_b = 0.16$, the baryon fraction.

Substantial differences become evident: at all masses, even rescaling by the baryon fraction, the SMF lies below the HMF. This happens because star formation is never 100% efficient, as quenching mechanisms like AGN feedback inhibit star formation. For this reason, while the knee of the HMF occurs at masses $> 10^{13} M_{\odot}$, the SMF knee shows already around $10^{11} M_{\odot}$, at least two orders of magnitude lower.

1.3 A challenge to the ΛCDM model?

As explained previously, according to the ΛCDM model, galaxy formation follows a hierarchical process where less massive halos assemble earlier in the Universe, and more massive halos form later. Thus, massive galaxies should primarily emerge in the later stages of the cosmic timeline, as their larger halos require more time to accumulate dark matter and gas. However, observations of galaxies at high redshifts ($z \sim 4 - 8$) present a significant challenge to this prediction, as described in Steinhardt et al. (2016). Several surveys, including CFHTLS, CANDELS, and SPLASH, have observed galaxies that appear fully formed and mature at these early epochs, with well-developed stellar populations and high metallicities—features typically associated with much older galaxies than predicted by ΛCDM. This discrepancy between theoretical predictions and observational data has led to what is now termed the "impossibly early galaxy problem" (Steinhardt et al., 2016).

Observations show that some massive galaxies appear to have formed too early in the Universe, defying the ΛCDM model's expectations of structure formation. For instance, galaxies at $z \sim 6 - 8$ with stellar masses of $M_* \sim 10^{11} - 10^{12} M_{\odot}$ seem to exist in dark matter halos that, according to ΛCDM, should not have had sufficient time to form at these redshifts. The halo mass function implied by observations at these high redshifts indicates a much higher abundance of massive dark matter halos ($M_h \sim 10^{12} - 10^{13} M_{\odot}$) than predicted by ΛCDM, suggesting that the number of massive galaxies observed in these early stages of the Universe cannot be explained by the model as it stands.

This situation raises several important questions: How can such massive galaxies form so early in the Universe? What modifications are required to reconcile the ΛCDM model with these observations?

One possibility is that stellar masses have been overestimated due to limitations in the

stellar population synthesis models used to interpret the data. Uncertainties in the assumed star formation histories, metallicities, dust extinction, or initial mass function (IMF) could bias the inferred stellar masses. However, the magnitude of the discrepancy seems too large to be fully accounted for by such systematic effects alone.

Another explanation is that star formation in the early Universe might have been significantly more efficient than currently modeled, potentially converting nearly all available baryonic matter into stars within very short timescales (e.g., 100–300 Myr). This would alter the stellar-to-halo mass relation at high redshift, allowing for more massive galaxies within a given halo mass. However, such high efficiencies would challenge our understanding of feedback processes that typically regulate star formation.

It has also been suggested that the ΛCDM model may underestimate the abundance and growth rates of massive DM halos at high redshift. If halo assembly occurs earlier or faster than currently expected, this could help explain the early appearance of massive galaxies.

Another possibility is the presence of selection biases in current surveys, preferentially detecting the most massive and luminous galaxies, while missing a more representative population. Yet, even accounting for such observational biases, the number density of observed massive galaxies remains difficult to reconcile with theoretical expectations.

Finally, the tension may reflect more fundamental issues with the standard cosmological model itself. Some authors, including Steinhardt et al. (2016), speculate that new physics or alternative cosmologies might be required.

Recent observations from JWST have further intensified this tension by uncovering additional examples of massive, evolved galaxies at high redshifts. In their paper, de Graaff et al. (2024) report the discovery of a massive quiescent galaxy, located at a redshift of 4.9, corresponding to 1.2 billion years after the Big Bang. Using observations from JWST, the authors confirmed that this galaxy has a stellar mass of approximately $10^{11} M_{\odot}$ and formed its stars rapidly within a short period of about 200 million years, after which star formation stopped. This challenges current models of galaxy formation, which typically predict that such massive galaxies should still be forming stars at this early cosmic age.

Further studies (Glazebrook et al., 2024) report the discovery of a massive galaxy at $z = 3.19$, which formed its stars at a redshift of approximately 11, around 500 million years after the Big Bang. Observations from JWST revealed that this galaxy is significantly redder than expected for its redshift, with spectral features indicating an older stellar

population.

Moreover, Carnall et al. (2024b) presents findings from the JWST EXCELS survey, which explores ultra-massive quiescent galaxies at redshifts between 3 and 5. These galaxies, with stellar masses greater than $10^{11} M_{\odot}$, challenge traditional models of galaxy formation. This sample includes the $z = 3.19$ galaxy studied by Glazebrook et al. (2024), which has an unexpectedly high stellar mass and metallicity for its age. This suggests that it formed much earlier than current models predict, pointing to faster-than-expected evolution of dark matter halos that could enable rapid star formation. Additionally, the paper reports two galaxies at $z = 4.62$ that formed the majority of their stars at even higher redshifts ($z \sim 8 - 10$). The authors find that, under typical assumptions, the existence of such galaxies is unlikely. However, if the galaxies formed with a nearly complete conversion of baryonic matter into stars, their rapid formation becomes plausible.

All these examples suggest that galaxy formation in the early Universe may have been more rapid and efficient than previously thought, requiring a reevaluation of the role of dark matter in early galaxy evolution.

1.4 Aim of the Thesis

This thesis investigates the tension between the observed properties of high-redshift galaxies and the predictions of the ΛCDM model, focusing on a sample of galaxies up to redshift $z \sim 4.6$. While previous studies have reported the existence of unexpectedly massive and evolved galaxies at early times, the role of modelling assumptions in driving these results remains an open question.

In this work, a detailed analysis of stellar population properties is carried out through a full-spectrum fitting approach using the `Bagpipes` code, comparing different SFH parameterizations. A distinctive aspect of the analysis is the removal of the cosmological prior on the maximum allowed stellar age, enabling the fitting procedure to explore solutions beyond the limits imposed by the ΛCDM model. This approach is completely novel in this framework, since evolutionary studies typically adopt a cosmological prior to reduce degeneracies between the inferred parameters. However, in this way it cannot be understood if the derived ages and mass formed are challenging the ΛCDM models because of this prior or intrinsically. This analysis therefore allows us to directly test whether the inferred galaxy ages naturally exceed the cosmic time available at their redshift when

such constraints are relaxed, and hence get hints if there is a problem with the ΛCDM model or with Stellar Population Synthesis models.

By systematically comparing results obtained with and without the cosmological prior, and under different SFH models, this thesis aims to evaluate the robustness of the claimed tensions and to assess whether they originate from true physical discrepancies or from model degeneracies.

Chapter 2

Methods

2.1 Stellar Population Synthesis Model

A lot of essential characteristics of unresolved stellar populations are embedded in their SEDs as described by Conroy (2013). These include the SFH, the metallicity and abundance patterns of stars, the initial mass function (IMF), the total stellar mass, and the physical conditions and quantity of dust and gas. Over the decades, significant effort has been made to extract information from SEDs, using data from the far ultraviolet (FUV) to the far infrared (FIR).
The UV and IR regions are challenging to probe due to atmospheric interference, but space-based observatories have enabled a detailed study of these wavelengths. Dust significantly affects the UV and IR light, absorbing UV and re-emitting it in the IR.

Stellar evolution theory was integrated into synthesis models to predict the range of stellar types at different ages and metallicities. This approach became the standard one for modeling galaxy SEDs in the 1990s, now known as Stellar Population Synthesis (SPS).

2.1.1 SPS Model Ingredients

- **Isochrones**: An isochrone defines the position of stars with a common age and metallicity on the Hertzsprung-Russell (HR) diagram, which displays stellar luminosity as a function of surface temperature, used to trace the evolutionary phases of stars. They are derived from stellar evolution calculations for stars ranging from

the hydrogen-burning limit (around 0.1 $M_{\odot}$) to the maximum stellar mass (around 100 $M_{\odot}$).

The process of creating isochrones is straightforward when stellar evolution tracks, the path of a single star in the HR diagram, are perfectly sampled in mass and time. However, since tracks are typically sampled discretely, there may be challenges in constructing isochrones during rapid evolutionary phases. Integrating isochrones into an SPS model is difficult because no single set covers the full range of ages, metallicities, and evolutionary stages. Typically, the Padova isochrones Bressan et al. (2012) are used for the majority of the age and metallicity range, while the Geneva Ekström et al. (2012) models are used to fill in the younger age ranges.

Besides the practical challenges of implementing current isochrone libraries, stellar evolution calculations involve several uncertainties that are important for SPS models. For instance, all the stellar models used necessitate approximations for inherently three-dimensional processes such as convection, rotation, mass-loss, and many others.

For this reason, more advanced models are developed to account for all these variables. However, these processes introduce significant uncertainties in the isochrones, which affect the predictions of the resulting SPS models.

- **Stellar remnants**: When a star reaches the end of its life, what remains is called remnant, and depending on the star's mass, it can be of different types: a white dwarf, a neutron star, a black hole, or it may not have a remnant at all. The stellar remnants are typically included in the total stellar mass calculation, and their contribution can be significant. Furthermore, the relationship between a star's initial mass and its final remnant mass is not well established, especially for massive stars, and it is also predicted to vary with metallicity, which adds complexity to the SPS models.

- **Stellar spectral libraries**: Stellar spectral libraries are essential to translate information from isochrones, such as surface gravities (g) and effective temperatures (T_{eff}) as a function of metallicity (Z), into observable SEDs. However, no single spectral library covers the full range of parameters needed to build SPS models. As a result, combining different libraries, which often vary in quality, is required. Spectral libraries can be either theoretical (generated from synthetic spectra using a defined set of input parameters) or empirical, meaning they are derived from actual observations of stellar spectra.

Theoretical spectral libraries offer the advantage of dense parameter space coverage and accurate spectra unaffected by observational issues, such as flux calibration and atmospheric absorption. However, their quality is limited by the accuracy of input atomic and molecular parameters and the assumptions made in model calculations. The empirical libraries instead provide observational spectra, but their coverage of parameter space is limited.

- **IMF**: The initial mass function (IMF), is the initial distribution of stellar masses along the main sequence. There are various parameterizations of the IMF (Salpeter 1955; Kroupa 2001; Chabrier 2005), but the most commonly used is the Salpeter law:

$$\frac{dN}{dM} \propto M^{-2.35}, \tag{2.1}$$

where dN is the number of stars in a given mass range, dM is the mass interval, and M is the stellar mass in solar units.

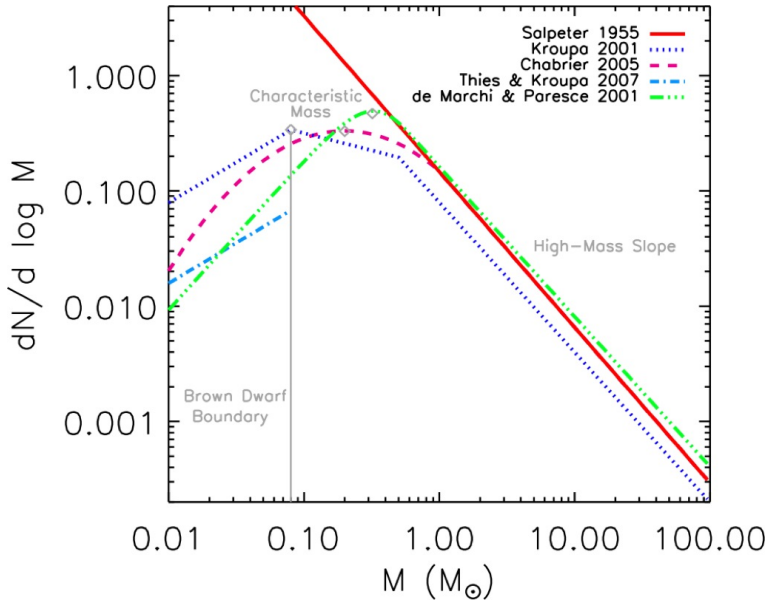

Figure 2.1: Comparison of commonly used stellar initial mass functions (IMFs), including those by Salpeter (1955), Kroupa (2001), and Chabrier (2003), among others. The plot highlights the differences in the slope and normalization of each IMF, especially at low stellar masses. Adapted from Offner et al. (2013)

This relation suggests that the number of stars decreases with increasing mass, meaning that low-mass stars are far more common than high-mass stars.

In the context of SPS, the IMF plays several key roles:(1) it sets the overall normalization of mass-to-light ratio (M/L) of a stellar population,(2) it influences how rapidly a passively evolving population dims over time,(3) it affects the spectral energy distribution of composite stellar populations and (4) it has a minor impact on the SED of single-age populations, as most of the light of a coeval population is dominated by stars at approximately the same mass, unless the IMF deviates significantly from Salpeter.

- **Dust**: Interstellar dust is found in nearly all galaxies, especially those with active star formation. In SPS, dust plays a critical role as it absorbs light in the UV to near-infrared (NIR) wavelengths and emits light in the IR: the two different processes, attenuation and extinction, are addressed separately because they depend on different properties of a galaxy.
  In the first process, the dust grains block light by absorbing and scattering starlight. Observing individual stars, one can estimate the total extinction along the line of sight by comparing the observed spectrum with the expected spectrum of the star in the absence of dust. Extinction thus measures the total loss of light along a given line of sight and is generally influenced by the optical properties of the dust grains, including their size and shape distribution.
  When modeling SEDs of galaxies, dust attenuation is an important factor, differing from extinction in two main ways: (1) light can be scattered both out of and back into the line of sight, and (2) the geometry of dust relative to the stars affects the resulting SED.
  To estimate dust attenuation, one compares the galaxy's observed spectrum with the expected spectrum without dust. However, dust attenuation is more complex to calculate than extinction.
  Although the dust attenuation curve's shape is influenced by factors such as star-dust geometry and grain size distribution, there are some general guidelines. In the simplest case of a uniform dust screen, the attenuation curve's shape is only weakly dependent on the total dust column density, with this weak dependence mostly due to scattered light. In more complex dust distributions, the attenuation curve generally becomes grayer (less steep) as the dust column density increases.
  Moreover, dust attenuation not only alters the shape of the SEDs but can also influence the physical properties derived from these models. For example, the choice of the dust attenuation curve can modify estimates of stellar mass, the age of the stellar population, and luminosity.

On the other hand, beyond 10 µm, the SEDs of normal galaxies are primarily influenced by dust emission, which results from dust grains exposed to varying levels of interstellar radiation. Models predict IR emission by combining grain size distributions, optical properties, and starlight models.
At longer wavelengths ($\lambda > 50$ µm), emission comes from dust grains at a steady temperature around 15 K, contributing about two-thirds of the total IR luminosity. Shorter wavelengths are dominated by single-photon heating of dust grains, including PAHs, accounting for the remaining third.

2.1.2 SSP Formalism

The foundation of any SPS model lies in the concept of a Simple Stellar Population (SSP), which represents the evolution of the SED of a single, coeval group of stars with the same metallicity and abundance pattern over time.
An SSP requires three inputs: stellar evolution theory (in the form of isochrones), stellar spectral libraries, and an IMF, each of which may depend on metallicity and/or abundance pattern. These elements are combined in the following way (Conroy, 2013):

$$f_{SSP}(t, Z) = \int_{m_{lo}}^{m_{up}} f_*\big(T_{\rm eff}(M), \log(g(M)) \mid t, Z\big)\Phi(M)\, dM, \tag{2.2}$$

where M is the initial stellar mass (zero-age main sequence), $\Phi(M)$ is the IMF, f_* is the stellar spectrum, and f_{SSP} is the time and metallicity-dependent SSP spectrum. The lower integration limit, m_{lo} is typically taken to be the hydrogen-burning limit (around 0.08 or 0.1 $M_\odot$, depending on the SPS code), and the upper limit is determined by stellar evolution. The isochrones provide the relationship between T_{eff}, $\log(g)$, and M for a given age and metallicity.

2.2 Composite Stellar Population Model

Composite Stellar Populations (CSPs) represent a more realistic approach to modeling galaxies compared to Simple Stellar Populations (SSPs). Unlike SSPs, CSPs account for three key factors: (1) they contain stars of various ages, as dictated by their SFH; (2) they include a range of metallicities, described by the time-dependent metallicity distribution function $P(Z, t)$; and (3) they incorporate the effects of dust. The overall SED of a CSP is determined by integrating over both stellar age and metallicity (Conroy,

2013):

$$f_{\mathrm{CSP}}(t) = \int_{t'=0}^{t'=t} \int_{Z=0}^{Z_{\max}} [\mathrm{SFR}(t-t')P(Z,t-t')f_{\mathrm{SSP}}(t',Z)e^{-\tau_d(t')} + Af_{\mathrm{dust}}(t',Z)]\, dt'\, dZ, \tag{2.3}$$

where $\tau_d(t')$, the optical depth of the dust models the time-dependent dust attenuation, and f_{dust} counts for the re-emission of absorbed light. The normalization constant A ensures the energy balance between the absorbed and re-emitted radiation. The SFH of a galaxy can be complex, but simple models are often used. The most common is the exponential one, where the star formation rate (SFR) declines over time $SFR \propto e^{-t/\tau}$, naturally arising in closed-box models.

Recently, rising SFHs have become popular for explaining high-redshift galaxy SEDs, as they align with hierarchical galaxy evolution theories. More advanced models combine an initial rise in SFR with a later decline ($SFR \propto t^{\beta}e^{-t/\tau}$), offering a more complete picture of galaxy formation. The metallicity treatment in CSP models is often simplified even further, with many studies assuming a single metallicity instead of using a full distribution $P(Z,t)$.

2.3 Age Determination

Determining the age of a galaxy is one of the fundamental challenges in astrophysics, and several (often complementary) methods are used. As described in Moresco (2024) the main methods are:

- **Full-spectrum Fitting (FSF)**: A statistical method used to determine the physical properties of galaxies by comparing their observed SED with a grid of theoretical SPS templates. This approach allows for joint constraints on multiple properties of a galaxy, such as stellar mass, metallicity, age, and SFH.
  The accuracy of the method improves with larger wavelength coverage, signal-to-noise ratio (SNR), and higher resolution of the data. By using FSF, astronomers can break parameter degeneracies and better constrain the physical characteristics of galaxies. Popular software tools are used to perform FSF, including Prospector Leja et al. (2017), Bagpipes (Bayesian Analysis of Galaxies for Physical Inference and Parameter EStimation; Carnall et al. (2018)), pPXF (penalized Pixel-Fitting; Cappellari and Emsellem (2004)), Starlight (Cid Fernandes et al. (2005)), and ALF (Absorption Line Fitter; Conroy et al. (2018).

- **Lick indices**: A method used to extract physical properties of galaxies by focusing on the absorption features of their spectra, rather than considering the full spectrum. These absorption lines provide valuable information on the galaxy's stellar population. For example, Balmer lines are strong indicators of the stellar population's age, iron lines reveal the metal content, and magnesium lines help constrain the enhancement of alpha-elements. The concept of Lick indices was introduced by Worthey (1994) and Worthey and Ottaviani (1997) as a standardized way to measure these absorption features and also to quantify the dependence of these indices on stellar age and metallicity. The Lick indices (measured in Ångström) are defined as equivalent widths (EW) over a given spectral feature as follows:

$$\text{Index} = \int_{\lambda_1}^{\lambda_2} \left(1 - \frac{F_\lambda}{F_{\lambda,\text{cont}}}\right) d\lambda,$$

  where F_λ is the observed flux in the feature band, and $F_{\lambda,\text{cont}}$ is the pseudo-continuum interpolated from adjacent blue and red sidebands. Further advancements, including work by Thomas et al. (2011b), Conroy and van Dokkum (2012), and Vazdekis et al. (2015), developed high-resolution models for Lick indices that account for age, metallicity, and varying element abundance ratios. These models allow astronomers to derive age estimates by comparing measured indices to model grids, helping to break the age-metallicity degeneracy by combining multiple indices.

  Public softwares are available to calculate Lick indices and support this analysis, e.g. PyLick (Borghi et al., 2023).

- **4000 Å break (D4000)**: A prominent feature in the spectra of massive, passive, and old galaxies. The D4000 feature is produced by the blending of various metallic lines below 4000 Å that is generated at increasing age and metallicity of the stellar population. Different definitions have been suggested to measure the D4000. Moresco et al. (2012)demonstrate a strong correlation between the D4000 feature (at fixed metallicity) and the galaxy's age.

2.3.1 Parameters Degeneracies

Stellar age is a particularly challenging parameter to constrain, mainly due to several degeneracies that affect the interpretation of galaxy spectral features. Among the most significant, there are the age-metallicity degeneracy, age-dust degeneracy, and age-SFH degeneracy. This means that different combinations of parameters can produce very

similar observed spectra, making it difficult to disentangle the effects and accurately determine the age.

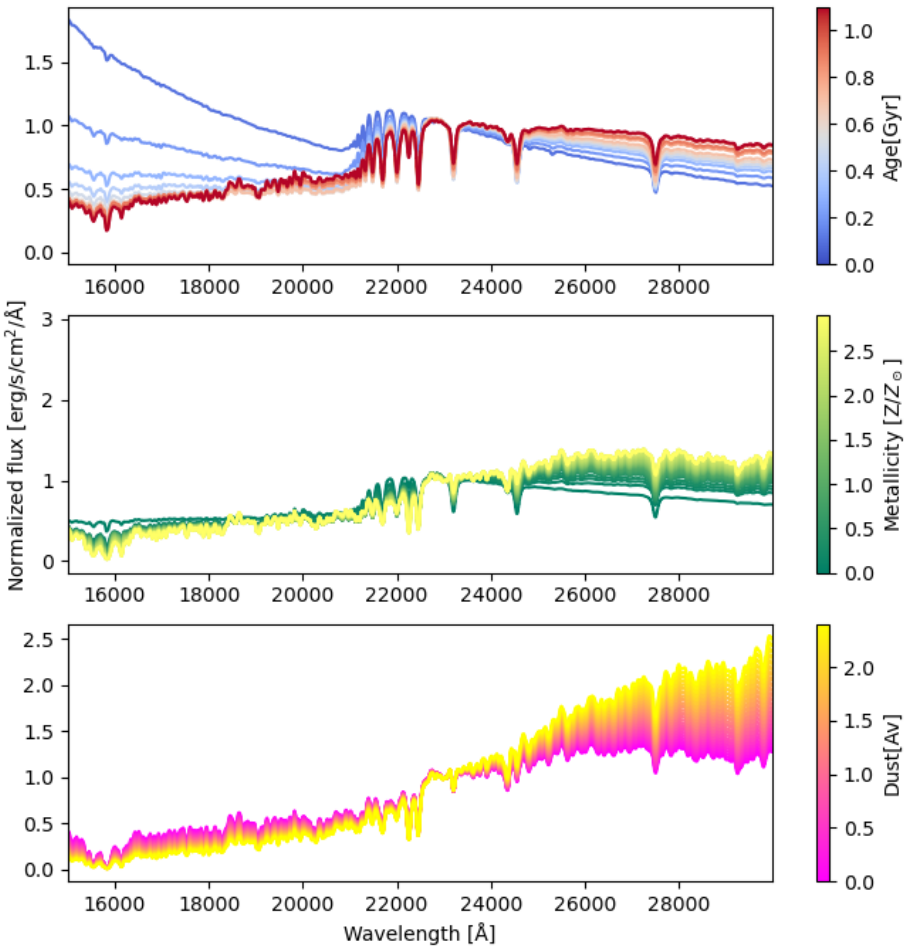

Figure 2.2: In this figure, we explore the degeneracies between parameters, exploring how a change in age (top panel), metallicity (middle panel), and dust attenuation (bottom panel) affect the spectrum of a galaxy. The reference model considered is a galaxy at redshift $z \sim 4.6$, typical for the objects considered in this Thesis; the age spans from 0 to 1 Gyr, the metallicity from 0 to 2.5 $Z_{\odot}$, and the dust attenuation (A_V) from 0 to 2 mag.

Figure 2.2 shows how a spectrum varies as a function of three fundamental parameters: age, metallicity, and dust.
In the first panel, it is shown how a spectrum characterized by an older age (red line) is dominated by older (and thus cooler) stars that emit less flux in the UV and more in the IR, reddening the spectrum. Conversely, the blue line shows how the spectrum of a younger galaxy (hotter stars) is bluer, with a strong emission in the UV and a depression in the IR. Additionally, the Balmer absorption lines in the spectrum are deeper and more pronounced in galaxies with a younger age.
The second panel shows how the metallicity influences the spectrum of a galaxy. A high metallicity (yellow line) generates a redder spectrum (cooler stellar population) and more prominent absorption lines, whereas a low metallicity (green line) results in a bluer spectrum (hotter stellar population) with less pronounced absorption lines.
The third panel shows how a model is modified by the presence of dust, specifically by Av, which quantifies the attenuation (in the visible band) of the flux. In general, the effect of dust on a spectrum generates strong absorption at shorter wavelengths (UV) and a re-emission of the flux at longer wavelengths (IR). More specifically, the graph shows how a high value of Av exaggerates this trend, causing a greater depression of the spectrum in the UV and a strong increase in the IR region.

Thus, it is clear the degeneracy of the three parameters, i.e., how different parameters (age, metallicity, dust) can produce the same effects on the spectrum. In fact, as discussed earlier, a higher age, metallicity, or amount of dust will all produce similar effects: they will attenuate the flux in the bluer part of the spectrum and enhance the emission at longer wavelengths.

2.4 Bayesian Full-Spectral Fitting with Bagpipes

The core of the analysis developed in this work is based on FSF, performed by modelling the observed galaxy spectra and photometry using the Bayesian Analysis of Galaxies for Physical Inference and Parameter Estimation (`Bagpipes`) code (Carnall et al., 2018). It is a widely used tool to infer the physical properties of galaxies, such as: stellar mass, age, metallicity, and SFH.
`Bagpipes` adopts a Bayesian approach —a statistical method used to estimate physical parameters by comparing observational data with theoretical models— that is grounded

in Bayes' theorem.

$$P(\boldsymbol{\theta} \mid D) = \frac{P(D \mid \boldsymbol{\theta}) \cdot P(\boldsymbol{\theta})}{P(D)}, \tag{2.4}$$

where

- $\boldsymbol{\theta}$ is the set of parameters to be estimated (mass, age, dust content...);
- $\boldsymbol{D}$ are the observed data;
- $P(\boldsymbol{\theta} \mid \boldsymbol{D})$ is the posterior probability: the probability of the parameters given the data;
- $P(\boldsymbol{D} \mid \boldsymbol{\theta})$ is the likelihood: how probable it is to observe those data given specific parameters;
- $P(\boldsymbol{\theta})$ is the prior: what is known or assumed about the parameters;
- $P(\boldsymbol{D})$ is a normalization constant.

In the code, a dictionary of instructions is used to define the parameters to be fitted (stellar mass, age...), the physical ranges over which each parameter is explored and the chosen prior: a distribution that represents prior knowledge (or assumptions) about the parameters, such as a uniform, Gaussian, or power-law distribution.

The following section provides a description of the parameters employed in the fitting procedures.

2.4.1 Fitting Parameters

The parameters derived using `Bagpipes` include both physical parameters and calibration parameters that account for technical issues in the observed spectra.

- **Physical Parameters:**
  - **Mass**: The total stellar mass formed, expressed in solar mass units. Stellar mass is a crucial parameter for understanding a galaxy's formation and evolution, as it reflects the amount of gas that has been converted into stars over time. This value is derived from modeling the galaxy's spectral energy distribution and star formation history. In this work, a uniform prior distribution is assumed on this parameter.

- **Age**: The age of the galaxy. It represents the time elapsed since the formation of the galaxy's stellar population. In this work, a uniform prior is adopted on age.
- **Metallicity**: The content of elements heavier than helium, reflecting the average abundance of heavy elements in the stellar population. It is expressed in solar units and estimated with a logarithmic prior distribution.
- **Star Formation History**: Describes how star formation has evolved over time in that galaxy. The SFH is a crucial component in understanding a galaxy's life cycle, as it provides insight into how gas has been converted into stars and how the galaxy's stellar population has developed over cosmic time. An SFH can be modeled in various ways using analytic functions:
  * **Constant** SFH: The galaxy formed stars at a constant rate between an initial and final time.
  * **Burst** SFH: The galaxy had a phase of intense star formation (a "burst") in a very short period.
  * **Delayed** SFH: Star formation began at a high rate and then gradually decreased over time

    $$\mathrm{SFH}_{\mathrm{delayed}}(t) = t\, e^{-t/\tau}, \tag{2.5}$$

    where t is the time since the onset of star formation and τ controls the timescale over which star formation rises to a peak and subsequently declines. In fact, as shown in Figure 2.3, higher values of τ (yellow line) correspond to more extended SFHs, indicating that stars have been forming over a longer period of time. Conversely, lower values of τ (blue/purple lines) result in more peaked and shorter SFHs, reflecting a rapid and intense burst of star formation.

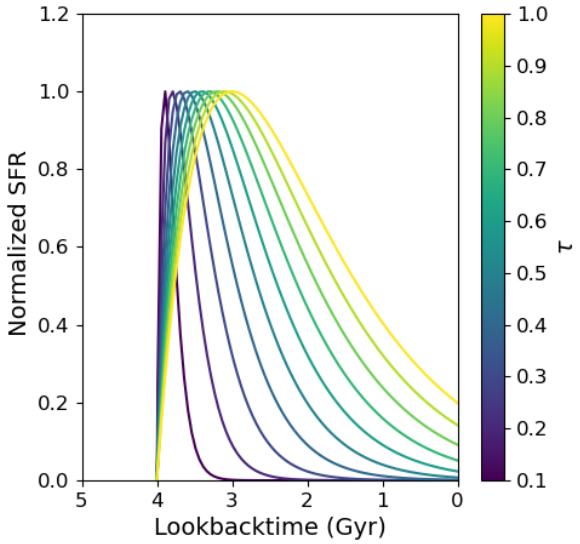

Figure 2.3: Evolution of the star formation rate over time: the parameter τ varies from 0 to 1 Gyr, highlighting its effect on the shape of the delayed star formation history.

* **Double-power law** SFH: Often used to describe galaxies with complex star formation histories. This model is parameterized by two distinct power-law components

$$\mathrm{SFH}_{\text{double power law}}(t) = \left[\left(\frac{t}{\tau}\right)^{\alpha} + \left(\frac{t}{\tau}\right)^{-\beta}\right]^{-1}, \tag{2.6}$$

that describe the increasing and decreasing slopes of the star formation rate (SFR) over time. This function is characterized by three parameters: α, β, τ. The parameter τ defines the point at which the slope of the function changes, α represents the steepness with which the function declines after the peak, and β represents the steepness with which it rises before the peak. Higher values of α and β indicate steeper slopes during the rise or fall, while lower values show progressively flatter profiles.

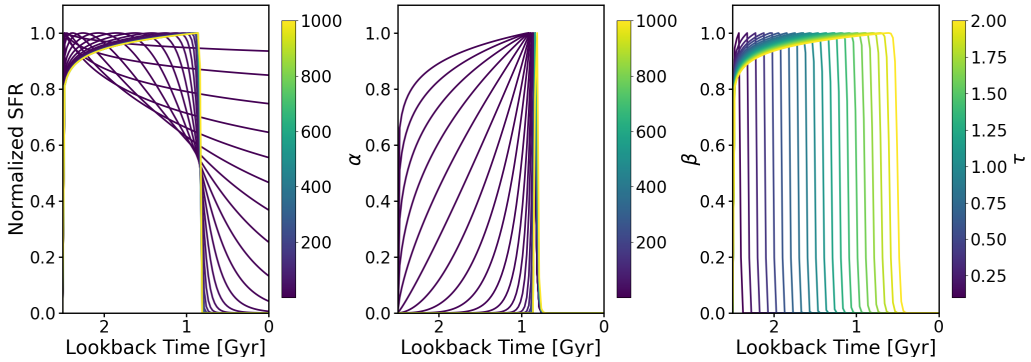

Figure 2.4: Effect of varying the parameters α, β, and τ on the shape of the double power law SFH. The parameters control the rising slope (α), the declining slope (β), and the turnover timescale (τ). The SFHs are shown as a function of lookback time from 0 to 2.5 Gyr, highlighting how different parameter combinations result in diverse star formation histories, from rapid bursts to extended star-forming phases.

  - ∗ **Non-parametric** SFH: This model allows the star formation rate (SFR) to vary freely across different time bins, without assuming any specific functional form. It provides greater flexibility in reconstructing complex star formation histories that may not be well captured by standard parametric models, enabling a more detailed exploration of the degeneracies and features in the stellar populations.

- **Dust**: Parametrized by the Salim law (Salim et al., 2018) as shown in Figure 2.5 (a more general law compared to the Calzetti law, Calzetti et al. (2000)), the model explores the following components: A_V(the attenuation parameter), δ (the variation of the slope with respect to the Calzetti law), where $\delta < 0$ implies stronger attenuation in the UV band (see the light blue curve), $\delta > 0$ implies a flatter curve (blue curve), and $\delta = 0$ recovers the Calzetti law. B measures the strength of the bump at $\lambda = 2175$ Å, and η takes into account the fraction of young/old stars. Uniform prior is adopted for these parameters.

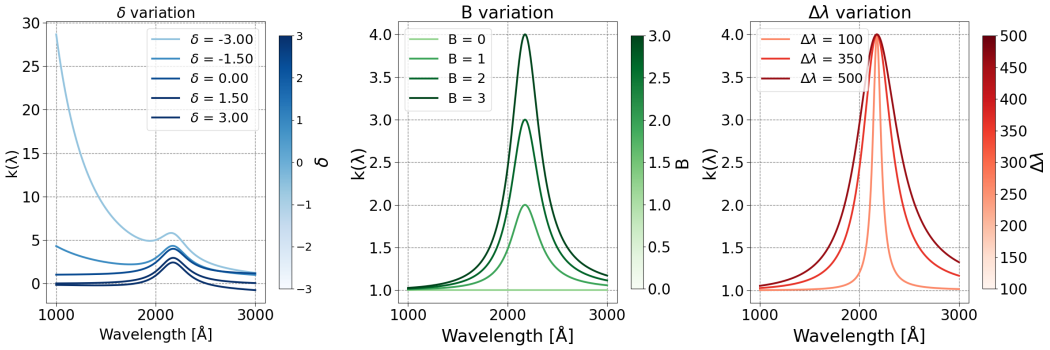

Figure 2.5: Effects of varying the parameters δ, B, and $\Delta\lambda$ of the Salim attenuation law on the resulting dust attenuation curve. Varying these parameters allows the model to reproduce a wide range of dust attenuation behaviors observed in galaxies.

The figure 2.6 presents a detailed visualization of how the dust parameters individually affect the resulting spectral model. As described earlier, the bump in the ultraviolet is related to strong absorption at 2175 Å (caused by the presence of carbon and PAHs), and as seen in the first panel of the figure 2.6, the greater the value of B (yellow color), the higher the bump's intensity. In the second panel, small values of δ show greater absorption at shorter wavelengths and more re-emission at longer wavelengths. The parameter A_V, shown in panel 3, represents the attenuation of the light flux, with greater attenuation for higher A_V values. Lastly, the η parameter is used to differentiate the attenuation of the spectrum caused by old stars or young stars. No difference between the two stellar populations means $\eta = 0$, while positive values indicate a significant contribution from young stars (more dust), whose light is more attenuated in the UV.

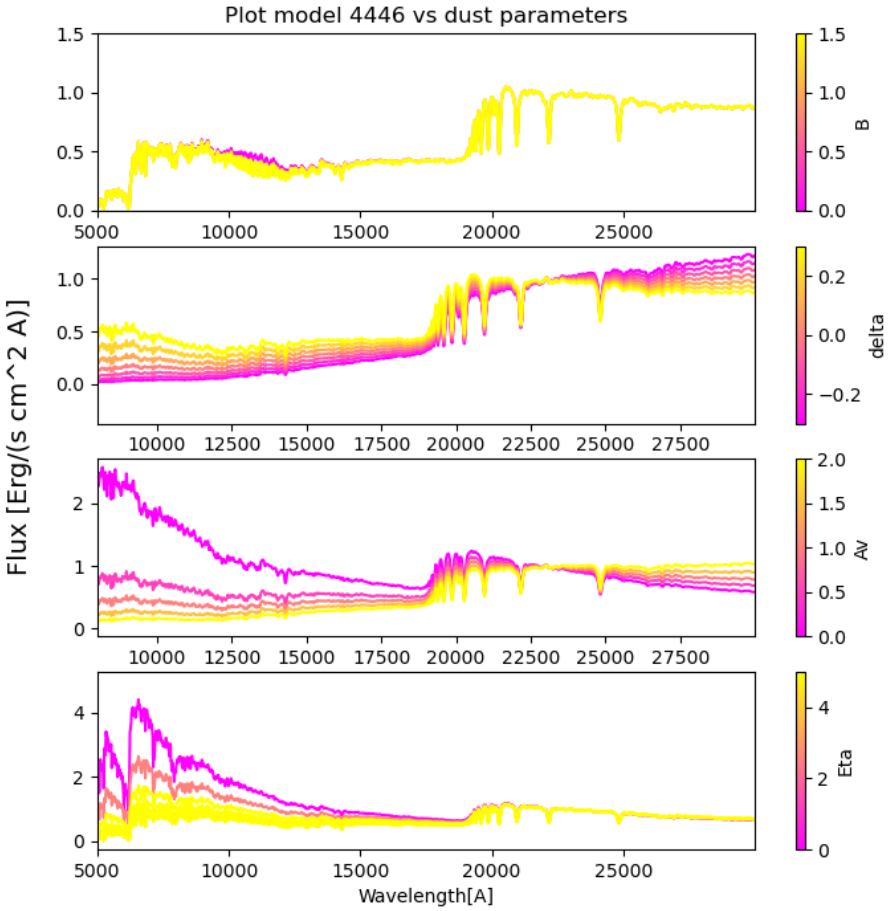

Figure 2.6: A detailed figure illustrating how variations in the parameters of the Salim attenuation law affect the resulting galaxy spectrum.

  - **Redshift** (z): Measures the shift of observed light to longer wavelengths due to the Universe's expansion. It provides information about the galaxy's distance and look-back time. A uniform prior distribution is used.
  - **Velocity dispersion** (σ): Measures the random motion of stars within the galaxy, providing insights into its dynamical mass and gravitational potential. A uniform prior distribution is adopted.

- **Calibration parameters:**

- **Noise Scaling**: Used to account for uncertainties or noise in the observational data during the fitting process, by scaling the errors on the data points. This helps improve the match between the model and the observations. A uniform prior distribution is adopted.
- **Spectrum shape calibration**: A second-order polynomial is used to correct, when combining photometry and spectroscopy, possible offsets caused by extraction losses and differences in calibration between the two data types, ensuring a more accurate fit. This polynomial correction accounts for instrumental and observational effects such as continuum normalization and flux calibration differences. The polynomial has the form

$$P(x) = \text{calib0} + \text{calib1} \cdot x + \text{calib2} \cdot (2x^2 - 1),$$

where x is the normalized wavelength. The coefficients calib0, calib1, and calib2 adjust the overall flux level (vertical offset), the linear slope of the continuum, and the curvature of the continuum shape, respectively. These coefficients are outputs of the fitting procedure performed by `Bagpipes`.

The values for all these parameters are specified within the `Bagpipes` code and are allowed to vary within a defined range, based on the current knowledge about galaxies and following the priors previously described.

The tables 2.1 and 2.2 summarize all the parameters discussed above. Table 2.1 lists the common set of parameters and priors adopted throughout the analysis, while Table 2.2 presents the various SFHs explored. For each model run, one of the SFHs described in Table 2.2 is considered both with and without a cosmological prior on the age. For nonparametric models, the SFH is discretized into a set of time bins, and the star formation rate is assumed to be constant within each bin. This approach removes constraints imposed by analytical functional forms, allowing the model to follow the intrinsic shape of the star formation history directly. The stellar mass formed in each time interval (bin) is estimated based on the fitting results. When using cosmological priors, the bins span the range from 0 to the age of the Universe at the galaxy's redshift; otherwise, they cover a fixed interval from 0 to 5 Gyr.

Component	Parameter	Symbol / Unit	Prior	Range
General	Redshift	z	uniform	$z_{\rm obs} \pm 0.1$
	Stellar velocity dispersion	σ/km s^{-1}	uniform	30 – 500
	Total stellar mass formed	$M_*/M_\odot$	uniform	0 – 15
	Stellar metallicity	$Z_*/Z_\odot$	logarithmic	0.01 – 3
Dust	V-band attenuation	A_V/mag	uniform	0 – 2
	Deviation from Calzetti slope	δ	uniform	-0.3 – 0.3
	Strength of 2175 Å bump	B	uniform	0 – 5
	Attenuation ratio for birth cloud	ϵ	uniform	1 – 5
Calibration	Zero order	P_0	uniform	0.3 – 3
	First order	P_1	uniform	-1.5 – 1.5
	Second order	P_2	uniform	-0.5 – 0.5
Noise	White noise scaling	a	logarithmic	1 – 10

Table 2.1: Model parameters, priors, and allowed ranges used in the FSF.

SFH	Parameter	Symbol / Unit	Prior	Range
Delayed	Age	age / Gyr	uniform	0 – age$_{\rm univ}(z)$
	τ (SF timescale)	τ / Gyr	uniform	0 – age$_{\rm univ}(z)$
Double Power Law with cosmo prior	Falling slope	α	logarithmic	0.01 – 1000
	Rising slope	β	logarithmic	0.01 – 1000
	Turnover time	τ / Gyr	uniform	0 – age$_{\rm univ}(z)$
Double Power Law without cosmo prior	Falling slope	α	logarithmic	0.01 – 1000
	Rising slope	β	logarithmic	0.01 – 1000
	Turnover time	τ / Gyr	uniform	0.01 – 5
nonparametric with cosmo prior	Bins (ages)	Gyr	uniform	0 – age$_{\rm univ}(z)$
nonparametric without cosmo prior	Bins (ages)	Gyr	uniform	0 – 5

Table 2.2: Comparison of SFH parameters and priors for different models.

2.4.2 Fitting Procedure

Once the fitting instructions are provided, `Bagpipes` utilizes Bayesian inference to determine the parameter values that best match the observational data (photometry, spectroscopy, or both).

`Bagpipes` performs the fit using a sampling algorithm, by default, the nested sampling algorithm, which is based on the Markov Chain Monte Carlo (MCMC) method. This algorithm is particularly efficient at exploring the multidimensional parameter space defined by the priors, identifying regions where the likelihood is higher.

A Markov chain is constructed by `Bagpipes`, where each sample point depends only on the previous one. At each step of the algorithm, a new set of parameter values is proposed. This new value is then either accepted or rejected based on its probability in relation to the posterior distribution. This iterative process allows `Bagpipes` to explore the parameter space effectively and to estimate the posterior distributions for each parameter.

Since `Bagpipes` relies on Bayesian inference, the choice of prior distributions directly affects the inferred parameter values. It is therefore essential to adopt physically motivated priors, informed by theoretical predictions or previous studies, in order to avoid introducing biases. Different types of priors can be used depending on the nature of the parameter. A uniform prior assigns equal probability to all values within a specified range, and is typically used when no particular value is favored a priori. On the other hand, a logarithmic prior distributes equal probability across each decade, which is better suited for parameters that cover a wide range of values. This approach ensures that both lower and higher values are sampled more uniformly on a logarithmic scale.

Another critical consideration is the presence of parameter degeneracies. As described earlier, these degeneracies must be carefully evaluated and, when possible, mitigated by including broad wavelength coverage and additional observational constraints.

Therefore, a clear understanding of the impact of priors and degeneracies is crucial for correctly interpreting the derived galaxy properties and for evaluating the robustness of the fitting results.

Outputs of the Fitting Process

After the fitting procedure, `Bagpipes` provides several automatic outputs:

- The posterior distributions of all fitted parameters.
- The median values and the corresponding 68% confidence intervals.
- The best-fit parameter set, defined as the one maximizing the posterior probability.
- The synthetic spectrum associated with the best-fit solution.

These outputs form the basis for inferring the galaxy's physical properties and reconstructing its formation and evolution history.

In addition to these standard outputs, I extracted and analyzed several key quantities in post-processing. In particular, the SFHs for each galaxy were reconstructed using the best-fit parameters and their uncertainties, by imposing the analytical or nonparametric forms assumed for each model (e.g., delayed, double power law, non-parametric). This step allowed for the direct visualization and comparison of the inferred SFHs across different assumptions.

From these reconstructed SFHs, the mass-weighted stellar ages were derived. The age of a galaxy is defined as the time when it had formed half of its total stellar mass, corresponding to the 50th percentile (t_{50}) of the cumulative mass formed over time.

$$M(t) = \int_0^t \psi(t')\, dt',$$

where $\psi(t)$ is the SFH, see Appendix A for more details. The spread in age was estimated from the 10th and 90th percentiles of the same cumulative distribution (t_{10} and t_{90}, respectively), with the lower and upper error bars given by $t_{50} - t_{10}$ and $t_{90} - t_{50}$.

While it is common practice to report uncertainties using the 16th and 84th percentiles (corresponding to a 68% confidence interval, equivalent to 1-sigma error under Gaussian assumptions), the choice of the 10th and 90th percentiles was motivated by the specific goal of this work: to constrain both the onset and the timescale of the star formation history. In particular, the 10th percentile marks the epoch of the earliest significant star formation, while the 90th percentile indicates when most of the stellar mass had been assembled. These bounds provide a more physically meaningful time window, which is especially relevant when testing the consistency of galaxy ages with the predictions of the ΛCDM model. This approach is consistent with the methodology proposed by Iyer et al. (2019), who define the SFH through a series of quantile lookback times $t_{\rm X}$, including t_{10}, t_{50}, and t_{90}, and interpret the difference $t90 - t10$ as a measure of the effective duration of star formation. A detailed description of the methodology is provided in Appendix A.

Contour plots were extracted for all parameters, and in particular compared for common parameters considered in the various fits, assuming different SFHs, namely stellar metallicity, dust attenuation, velocity dispersion, and mass formed. These plots were useful for assessing the robustness of the inferred parameters and identifying possible degeneracies.

2.5 Modifications to the Bagpipes Code

In this work, two versions of the `Bagpipes` code were employed to perform the full-spectral fitting and extract galaxy parameters. The first version corresponds to the standard publicly available release, which applies a maximum age for the stellar populations based on the cosmological age at the redshift of each galaxy, in accordance with the ΛCDM model constraints.

To explore the impact of cosmological assumptions on the derived stellar ages, a second, modified version of `Bagpipes` was developed. In this version, the maximum allowed stellar age was fixed to 5 Gyr, independent of the galaxy redshift or cosmological constraints. This approach (introduced and extensively tested in Tomasetti et al. (2023) and Jiao et al. (2023)) was chosen to challenge the ΛCDM-based prior on stellar ages, allowing the fitting procedure to explore a wider parameter space and test the robustness of age estimates against cosmological assumptions.

This modification is particularly relevant for the analysis of high-redshift galaxies observed in JWST surveys, where stellar populations might appear older than allowed by the standard cosmological age limit, potentially indicating tensions with the standard cosmological model or requiring alternative interpretations.

Chapter 3

The oldest and most distant galaxies with JWST

3.1 The James Webb Space Telescope

The data used in this thesis were obtained with the JWST, one of the most advanced space observatories ever built. Launched on December 25, 2021, JWST is a joint mission of NASA, ESA (European Space Agency), and CSA (Canadian Space Agency), designed to observe the Universe in the infrared. Unlike the Hubble Space Telescope, which orbits the Earth, JWST operates near the second Sun-Earth Lagrange point (L2), approximately 1.5 million kilometers from Earth.

JWST covers a wide wavelength range from 0.6 to 28 microns, enabling it to detect the faint infrared signatures of the first galaxies, peer through dust-obscured star-forming regions, and characterize the atmospheres of exoplanets. Its large 6.5-meter segmented primary mirror - nearly three times the size of Hubble - provides significantly higher light gathering power and resolution. Equipped with advanced instruments such as the Near-Infrared Camera (NIRCam), the Near-Infrared Spectrograph (NIRSpec), and the Mid-Infrared Instrument (MIRI), the JWST enables unprecedented sensitivity and precision in the near- and mid-infrared regimes.

A major scientific goal of JWST is the study of high-redshift galaxies, pushing the observational frontier into the Epoch of Reionization and the era of early galaxy assembly. Its unique capabilities allow for detailed spectroscopic and photometric investigations of

galaxy structure, star formation histories, and stellar populations at redshifts up to $z \gtrsim 10$, as well as intermediate redshifts ($z \sim 1 - 5$), a regime that has historically been difficult to probe.

Although the mission was initially planned for a 5-10 year duration, successful launch and deployment have left sufficient propellant to support more than 20 years of operations.

3.1.1 JWST Extragalactic Surveys

The JWST legacy is being built through a number of extragalactic surveys, designed to probe the formation and evolution of galaxies across cosmic time, with particular focus on high-redshift, massive, and quiescent galaxy populations. Among these, only a subset provides the data analyzed in this thesis:

- **EXCELS (The Extremely Red, Compact, Early-type Legacy Survey)** is a Cycle 2 program targeting a carefully selected sample of galaxies at $z \sim 2 - 5$, using deep NIRSpec spectroscopy. One of its primary goals is to constrain the formation epochs, star formation histories, and structural properties of early-type galaxies in the early Universe (Carnall et al., 2024a).
- **BlueJay** is a JWST Cycle 1 program focused on the spectroscopic study of galaxies identified in pre-existing photometric catalogs. It combines medium-resolution NIRSpec spectroscopy with broad-band imaging to study their stellar content and physical properties (Park et al., 2024a).
- **PRIMER (Public Release IMaging for Extragalactic Research)** is a JWST Cycle 1 program designed to provide deep NIRCam imaging of legacy fields such as COSMOS and UDS. It enables the identification of high-redshift galaxy candidates, including quiescent systems at $z > 3$, which are then followed up spectroscopically by programs such as EXCELS (Dunlop et al., 2023).
- **COSMOS-Web** is the largest Cycle 1 program in terms of area, aiming to map ~ 0.6 deg^2 of the COSMOS field. While its depth is shallower compared to JADES or CEERS, its wide-area coverage is ideal for studying rare populations such as massive quiescent galaxies at $z > 3$ (Casey et al., 2023).

Specifically, the spectroscopic data are drawn from the EXCELS and BlueJay programs, while PRIMER and COSMOS-Web contribute photometric observations used for target selection and characterization.

These datasets, combined with the capabilities of JWST, allow for a detailed investigation of the stellar populations, star formation histories, and ages of galaxies during the early stages of cosmic history.

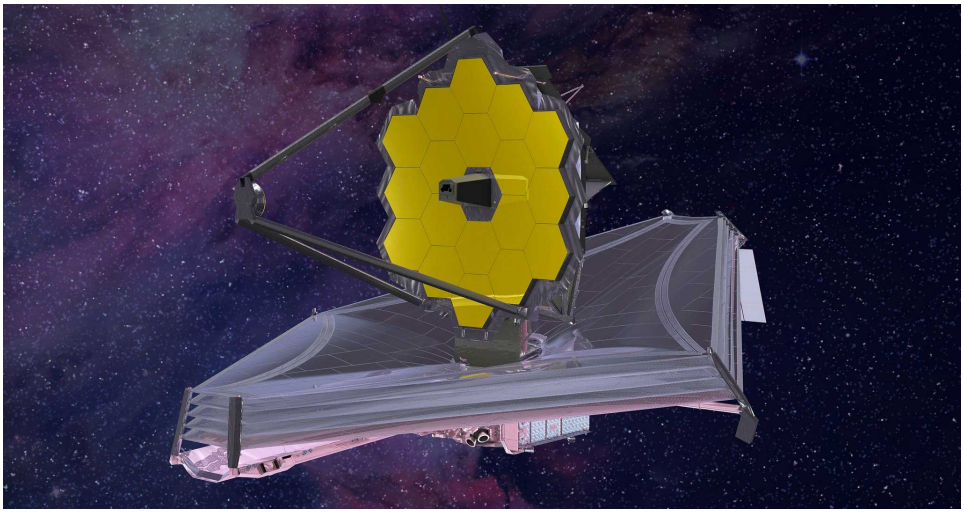

Figure 3.1: An illustration of the James Webb Space Telescope (credit:Northrop Grumman).

3.2 Selection Criteria

Although quiescent galaxies are typically identified using a combination of morphological, photometric, and spectroscopic criteria—such as red rest-frame colors, low specific star formation rates, and absence of emission lines as described in Moresco (2024) — this study does not apply such selection procedures directly. Instead, the analysis focuses on a curated sample of high-redshift passive galaxy candidates drawn from JWST spectroscopic surveys.

The initial sample was constructed by exploring publicly available data from JWST programs such as EXCELS and BlueJay, designed to target massive galaxies at cosmic noon and earlier epochs. BlueJay, in particular, provided an initial list of approximately ten passive galaxy candidates. However, most of these were located at redshifts below $z = 2.5$, making them less suitable for the scientific objectives of this work. As a result, only one object from BlueJay (ID 7549) was selected, as it displayed the oldest stellar population among the candidates and will be discussed in detail in a dedicated section. The galaxy 9209 instead was observed with NIRSpec as part of Cycle 1. We

also include the galaxy SNH0pe-NS274, observed with JWST NIRSpec during Cycle 1, which was not selected from a survey but studied as an isolated, massive quiescent galaxy. Additional galaxies were selected from the EXCELS survey, which provided medium-resolution NIRSpec spectra for a range of massive galaxies at $z > 3$.

3.3 Datasets Description

Having outlined the selection criteria for our sample, we now proceed to describe the dataset used in this study. The final sample consists of seven galaxies in the redshift range $3 < z < 5$, with medium-resolution NIRSpec spectroscopy and stellar masses $log_{10}(M_*/M_\odot) \sim 11$, and the BlueJay survey which provided one additional galaxy at $z \sim 2.62$, notable for its older stellar population and lower redshift compared to other candidates. Table 3.1 summarizes the selected galaxies.

Galaxy ID	z	Reference	Survey	Possible ΛCDM breakers
9209	4.66	Adam C. Carnall et al. (2023)	Individual target	×
109760	4.62	Adam C. Carnall et al. (2024)	EXCELS	×
117560	4.62	Adam C. Carnall et al. (2024)	EXCELS	×
SNH0pe-NS274	4.11	Po Feng Wu (2024)	Individual target	×
50789	3.99	Adam C. Carnall et al. (2024)	EXCELS	×
55410	3.19	Adam C. Carnall et al. (2024)	EXCELS	✓
7549	2.63	Minjung Park et al. (2024)	BlueJay	✓

Table 3.1: Description and properties of the considered JWST sample

The selected sample consists of galaxies that had already been studied in previous works, where fitting analyses had been performed. This allowed for a direct comparison with existing literature results and a critical assessment of the recovered physical parameters. In particular, two galaxies were included because they had been identified in earlier studies as potential ΛCDM breakers, which makes them especially relevant for this analysis.

3.3.1 Photometric and Spectroscopic Data Extraction

All raw JWST data are available via the Mikulski Archive for Space Telescopes (MAST `https://mast.stsci.edu/portal/Mashup/Clients/Mast/Portal.html`), while the photometric data were selected from the ASTRODEEP catalog (NIRCam `http://www.`

astrodeep.eu/astrodeep-jwst-catalogs/), by searching for the sample galaxies using the cross-match method of coordinates. This method allows for finding the considered galaxy within a catalog: starting from the celestial coordinates of the target, I set a tolerance radius of 1 arcsecond. Among all the galaxies in the catalog, the one closest to the specified coordinates is identified as the matched object.

Once the galaxy is identified, the corresponding flux measurements and uncertainties are extracted for each photometric band. The photometric filters used in this work include HST bands F435W, F606W, F775W, F814W and JWST/NIRCam bands F090W, F105W, F115W, F150W, F200W, F277W, F356W, F410M, F444W. For each filter, the effective wavelength and transmission curve are retrieved to properly model the photometric data. This allows for accurate convolution of the theoretical SED models with the filter response functions, ensuring a consistent comparison between observed and modeled fluxes.

An example of the spectrum of a galaxy is shown in Figure 3.2, together with its photometric points used in the fit. Photometric data are essential in this process because, as shown in the figure, they cover a much broader wavelength range compared to the spectroscopic data alone. This wider coverage strengthens the fit and helps constrain the model more reliably, especially in wavelength regions where the spectroscopic signal-to-noise ratio is low or where the spectral coverage is incomplete. Incorporating photometry reduces degeneracies in the model parameters by providing independent flux measurements across a broad spectral range. As shown in the previous chapter (see Fig. 2.2), several degeneracies — such as those between age, dust attenuation, and star formation history — remain unresolved when only the rest-frame optical spectrum is considered. By extending the wavelength coverage into the rest-frame UV and near-IR, photometric data help disentangle these effects.

In Figure 3.2, the observed spectrum is plotted in gray, while the photometric points are shown in black. The blue spectrum represents the calibrated data after applying the polynomial calibration correction. This polynomial correction accounts for instrumental and observational effects, such as slit losses and throughput variations, which can cause the observed spectrum to deviate from the true flux level.

It is important to note that the photometric points tend to shift the spectrum upward. This shift occurs because the telescope's spectroscopic observations only capture a fraction of the total light emitted. In contrast, the photometry samples the integrated flux more completely. Therefore, the photometric data serve as a crucial anchor for cali-

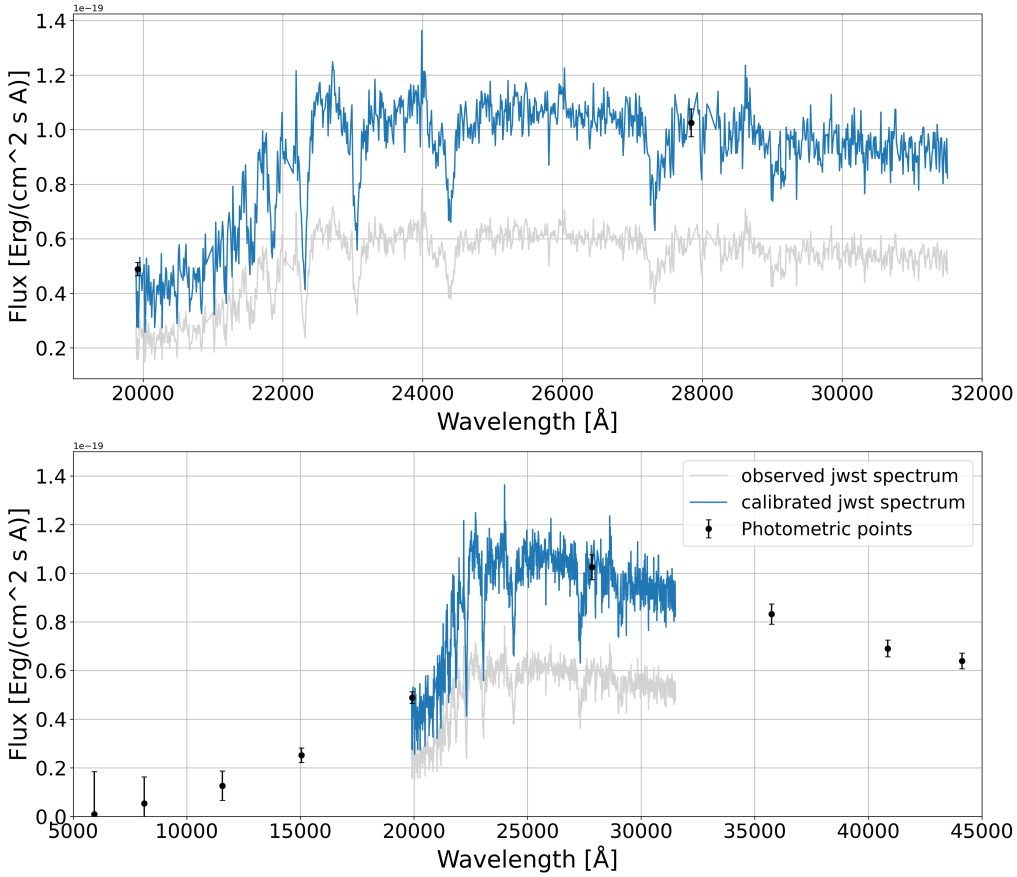

Figure 3.2: Example of a galaxy spectrum 117560 used in this work. The original observed spectrum is shown in gray, representing the uncalibrated NIRSpec data. The black points correspond to the photometric flux measurements extracted from multiple HST and JWST filters. The blue curve represents the calibrated spectrum after applying the polynomial calibration correction.

brating and scaling the spectral data correctly. This calibration step ensures that the final model reproduces both the high-resolution spectral features and the broadband photometric fluxes consistently.

A concise review of the existing information concerning the galaxy sample adopted in this work is presented in the following section. The observed spectra of the galaxies in the sample are shown in Figure 3.3

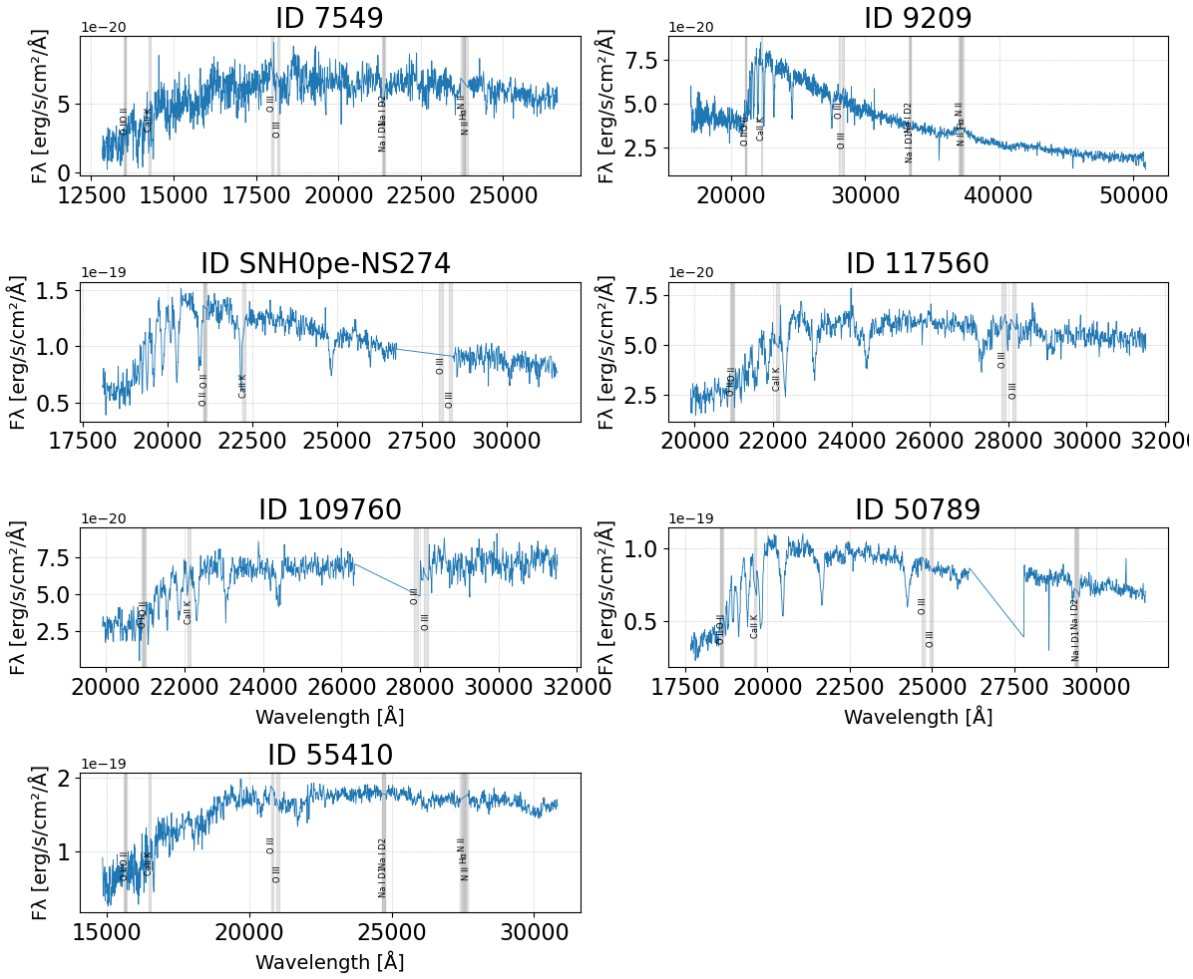

Figure 3.3: Observed spectra of the seven galaxies in the sample, shown as specific flux (F_λ) as a function of observed wavelength. The grey shaded regions mark the main emission and absorption lines ([O II], [O III], Hα, [N II], Ca II K, Na I D), which are masked as they are not associated with star formation, as will be discussed later.

3.3.2 Galaxy 9209

In their 2023 study, Carnall et al. (2023) presented the discovery and detailed analysis of GS-9209 (observed under JWST Programme ID 9209, PI: Carnall), a massive quiescent galaxy observed at a redshift of $z = 4.658$, approximately 1.25 billion years after the Big Bang. Thanks to the capabilities of JWST, such distant and faint galaxies can now be observed with unprecedented accuracy.

The key findings and characteristics are reported below.

- **Stellar Mass and Age**: GS-9209 has a stellar mass of $M_* = 3.8 \times 10^{10} M_\odot$, and its stellar population formed primarily between 600 and 800 million years after the Big Bang, over a period of only 200 Myr. This rapid star formation suggests an efficient mechanism for creating massive galaxies in the early Universe.
- **Quenching of Star Formation**: The galaxy transitioned to a quiescent state at around $z \sim 6.5$, marking the cessation of active star formation just 800 million years after the Big Bang.
- **Compact Structure**: GS-9209 has an effective radius of ∼215 parsecs, making it one of the most compact galaxies observed at such high redshifts.
- **Active Galactic Nucleus (AGN)**: The presence of broad $H\alpha$ emission lines and an unusually high [NII]/Hα ratio indicates the presence of an active supermassive black hole $M_{BH} = 5 \times 10^8 M_\odot$. This AGN likely played a role in the quenching of the galaxy's star formation, possibly through feedback mechanisms.

The discovery of GS-9209 provides important insights into the processes that drive galaxy formation and quenching in the early Universe. Its existence challenges the standard models of galaxy evolution, showing that massive quiescent galaxies may have formed much earlier than previously thought, and that AGN feedback may have been a key driver of early star formation suppression.

3.3.3 Galaxy SNH0pe-NS274

In their 2024 study, Wu (2024) presented a massive recently quenched galaxy at redshift $z = 4$. This galaxy, which had recently transitioned to a quiescent state, is used as a key example to demonstrate the role of AGN feedback in shutting down star formation at early cosmic times.
The key findings and characteristics are reported below.

- **Stellar Mass and Star Formation History**: The galaxy has a stellar mass of $M_* = 1.2 \times 10^{11} M_\odot$.The star formation rate (SFR) was observed to be in rapid decline, with the galaxy having entered a quiescent phase only 50 million years ago, a very short timescale for such a significant transition.
- **AGN Activity and Feedback Mechanism**: The spectrum revealed clear signatures of an AGN, with strong [Ne III]/[O II] and [O III]/Hβ ratios, consistent with the presence of an active black hole at the center of the galaxy. The study also found significant evidence of an outflow of neutral gas, characterized by absorption lines of Fe II and Mg II, which are blueshifted by $\sim$250 km/s relative to the stellar continuum. This outflow is thought to be driven by the AGN and is responsible for expelling gas from the galaxy.
- **AGN-Driven Outflow:** The outflow rate was found to be approximately 7 times higher than the current star formation rate, indicating that the AGN feedback mechanism is capable of rapidly depleting the gas reservoir necessary for star formation.

The study underscores the critical role of AGN feedback as a mechanism that can rapidly quench star formation in high-redshift galaxies, challenging the traditional view of slow, continuous quenching processes.

3.3.4 Galaxy 7549

Park et al. (2024b) analyzed a sample of 14 massive quiescent galaxies ($M_* > 10^{10} M_\odot$) at redshift $z \sim 2$, selected from the Blue Jay Survey, using deep spectroscopy obtained from JWST. The goal was to understand the SFH and the quenching mechanisms in these galaxies during the cosmic noon period, when star formation and galactic mergers reach their peak.
Galaxy 7549, which is analyzed in this work, is part of this sample. Their key results are reported below:

- **Target galaxies classification**: galaxies are divided into three groups according to the timing of their formation and quenching. Galaxy 7549, observed at z=2.63, belongs to Group 1, characterized by early formation and early quenching. Group 2 includes galaxies that also formed early but quenched only recently, whereas Group 3 comprises galaxies that underwent both formation and quenching at more recent epochs.

- **Evolving Ancient Galaxies**: Two galaxies in the sample (7549 is one of the two) show star formation and quenching at $z > 6$, suggesting that these may be descendants of early post-starburst galaxies. However, the other galaxy was excluded from further analysis due to the lower quality of its spectrum.

The presence of gas outflows suggests that AGN plays an active role in regulating star formation. The predictions for the number density support the idea of early formation and quenching of these galaxies, offering important insights into the evolution of galaxies in the young Universe.

3.3.5 Galaxies 109760, 117560, 50789, and 55410

The study by Carnall et al. (2024b) is part of the JWST EXCELS survey (Early eXtragalactic Continuum and Emission Line Science), which uses NIRSpec onboard the James Webb Space Telescope to obtain deep spectroscopic observations of distant galaxies. The focus here is on four ultra-massive, quiescent galaxies in the redshift range $3 < z < 5$, corresponding to cosmic ages between approximately 1 and 2 Gyr.

Galaxies 109760 and 117560:
Two of the galaxies identified at $z = 4.62$ have stellar masses exceeding $10^{11} M_{\odot}$ and are separated by ∼860 kpc, suggesting they belong to a larger cosmic structure. Spectroscopic analysis indicates that both galaxies formed the bulk of their stellar mass between redshifts z∼8 and z∼10, i.e. within the first 500 Myr after the Big Bang. Despite their similar ages and masses, the galaxies exhibit different stellar metallicities, pointing to divergent chemical enrichment histories.
Galaxies 50789 and 55410:
The other two galaxies, located at $z = 3.99$ and $z = 3.19$, had already been identified in previous works. In particular, the galaxy 55410 has been the subject of intense discussion due to its old stellar population and high mass (Glazebrook et al., 2024). The new JWST spectra confirm a high stellar metallicity and a significant α-element enhancement ([Mg/Fe] $\sim +0.42$), consistent with an extremely rapid star formation timescale (<0.5 Gyr).
To quantify the tension with ΛCDM cosmology, the authors adopt a statistical approach based on extreme value theory and the halo mass function. The presence of such massive quiescent galaxies at these redshifts appears highly improbable within the survey volume. However, if one assumes a maximal conversion efficiency of baryons into stars,

then the observed galaxies become marginally consistent with ΛCDM expectations.

3.4 Exploring a different approach in the analysis

The analysis of the galaxies in this study follows a similar approach to the existing literature, where stellar population parameters such as mass and age are determined using SED modeling codes. However, a key novelty of this work is the use of a modified implementation of the `Bagpipes` code, which removes the age limit typically imposed by the ΛCDM model. In particular, the age parameter was left free to vary up to 5 Gyr, significantly exceeding the age of the Universe at the redshift of the galaxy sample. This modification was first introduced in Jiao et al. (2023), and extensively tested both at low redshift ($z < 0.5$) and at high redshift ($z \sim 2 - 4$) in Tomasetti et al. (2023). This adjustment makes it possible to investigate SFHs without enforcing cosmological priors, thereby enabling the identification of inconsistencies with the cosmological scenario that might otherwise be suppressed.

Such flexibility is particularly relevant where observational uncertainties and degeneracies complicate the interpretation of spectral data. The aim is not to question the validity of the ΛCDM paradigm, but rather to assess whether the assumptions embedded in standard SPS models, such as SFH parameterizations, the choice of IMF, and dust attenuation prescriptions, are sufficient to accurately capture the diversity of galaxy evolution at early epochs. By combining Lick index analysis and full-spectral fitting, and by relaxing prior constraints on stellar ages, this study provides a more flexible framework to examine whether the inferred SFHs are consistent with cosmological predictions. Extending the maximum allowed age to 5 Gyr has a direct impact on the shape of the inferred SFHs, depending on the adopted parameterization.

In this work, the extension of the maximum allowed stellar age to 5 Gyr was applied only to the double power-law (DPL) and nonparametric SFH models. The delayed-τ model, being simpler and more constrained by its parameterization, was not extended to 5 Gyr. This is because the delayed-τ SFH tends to favor shorter characteristic timescales (τ), resulting in more stable and narrower star formation histories that do not necessarily benefit from a higher age limit. On the other hand, the more flexible DPL and nonparametric models can take advantage of the extended age range to explore more complex and extended SFHs, allowing for stellar mass contributions from older epochs that would

otherwise be excluded by cosmological age constraints.

In the double power-law parameterization, the shape of the SFH is controlled by the rising and declining slopes and the characteristic timescale τ, which marks the peak of star formation. Allowing the maximum stellar age to extend to 5 Gyr lets τ take larger values, effectively shifting the peak to earlier cosmic times (higher redshift), closer to the Universe's beginning. This increased flexibility enhances the model's ability to describe extended SFHs but also introduces stronger degeneracies among the parameters (α, β, and τ), making them more difficult to constrain without strong priors or complementary observations. Additionally, the DPL's analytical form is more complex than simpler models, which complicates the direct interpretation of parameters.

For the nonparametric SFHs, which distribute star formation across age bins, the impact is directly structural. The temporal grid has been extended beyond the cosmological age to include one or more bins up to 5 Gyr. This increases the number of degrees of freedom, allowing the fit to assign significant stellar mass to very old bins that would otherwise be excluded. Consequently, the inferred SFHs may feature ancient stellar components that are incompatible with ΛCDM expectations but remain consistent with the observed spectra.

Chapter 4

Constraining ages and SFHs of passive galaxies in the early Universe

In this section, we present the results obtained for the galaxy sample under examination, with the aim of deriving the main physical properties of their stellar populations, such as age, star formation history, metallicity, and dust content. The analysis is structured in two main parts. First, we measure the absorption features observable in the spectra by deriving the corresponding Lick indices. These indices are then interpreted to obtain initial estimates of the stellar age and metallicity. Second, we perform full-spectral fitting, a more comprehensive technique that combines spectroscopy and broadband photometry, allowing us to extract detailed constraints on the SFH and other physical parameters over the full wavelength range covered by both datasets.

The primary objective is to obtain robust estimates of stellar age and formation timescales for the galaxies discussed in the previous chapter. These systems represent a golden sample of the oldest passive galaxies currently known in the literature and observed with JWST. Their early quiescence and high stellar masses make them ideal laboratories for investigating the formation pathways of massive galaxies and testing the predictions of galaxy evolution models in the early Universe.

4.1 Lick Indices Analysis

The methodology based on Lick indices, as detailed in Section 2.3, is here applied to the selected galaxy sample to derive quantitative estimates of stellar age and metallicity.

In this work, although we measure a broad set of Lick indices, we focus our analysis on a selected subset—namely $H\beta$, Mgb, Fe5270, Fe5335, and the combined index [MgFe]'—because these indices have well-established diagnostic diagrams specifically designed to constrain stellar age, metallicity, and α-element enhancement. Specifically, $H\beta$ is primarily sensitive to the age of the stellar population, while Mgb and the two iron lines (Fe5270 and Fe5335) trace the overall metallicity and elemental abundance patterns.

Consequently, the tables and discussion primarily emphasize these indices, while the full set of measured indices is reported in the figures for completeness. It is important to note that not all indices are measurable in every galaxy, as their visibility depends on the wavelength coverage in the observed spectra.

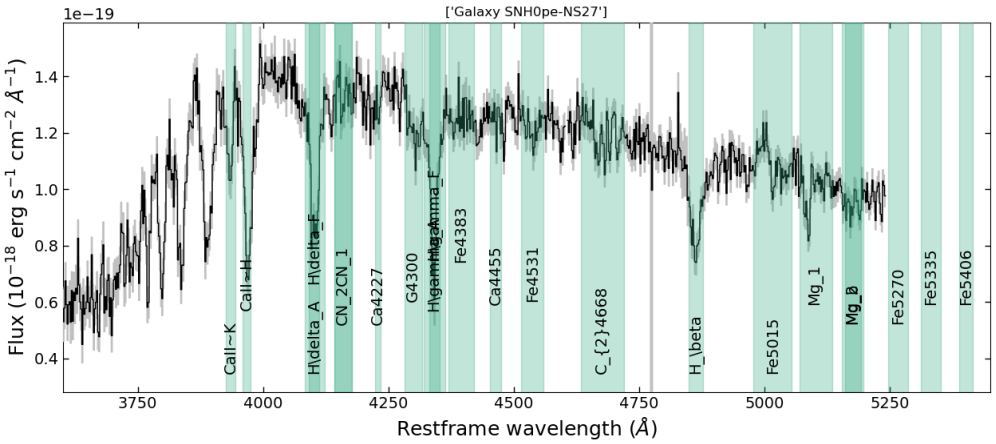

Figure 4.1: Illustrative case of a galaxy spectrum (ID=SNH0pe-NS274) showing the ranges of the observable Lick indices.

Figure 4.1 shows an example galaxy, including the spectral regions used to measure the Lick indices. The remaining galaxies are reported in the Appendix B. A summary table 4.1 is provided, reporting the measured Lick index values for the sample of galaxies analyzed.

Galaxy	Hβ [Å]	Mgb [Å]	Fe5270 [Å]	Fe5335 [Å]	[MgFe]' [Å]
07549	2.32 ± 0.54	-0.70 ± 0.65	2.05 ± 1.08	-1.84 ± 1.19	-0.68 ± 0.87
9209	5.20 ± 0.30	0.51 ± 0.40	0.25 ± 0.46	-0.01 ± 0.54	0.21 ± 0.47
109760	–	0.58 ± 0.76	1.47 ± 0.79	0.55 ± 1.02	0.64 ± 0.90
117560	4.08 ± 0.42	2.36 ± 0.53	1.12 ± 0.59	-4.46 ± 0.80	–
SNH0pe-NS274	5.32 ± 0.53	1.61 ± 0.48	–	–	-
50789	5.18 ± 0.26	1.53 ± 0.30	–	–	-
55410	0.74 ± 0.37	1.37 ± 0.39	0.91 ± 0.43	-0.42 ± 0.45	1.00 ± 0.68

Table 4.1: Measured Lick indices for the selected galaxy sample. All indices are expressed in Ångström and have been corrected to a velocity dispersion of $\sigma = 0$ km/s.

4.1.1 Diagnostic Diagrams and Velocity Dispersion Correction

Following the calculation of the Lick indices, this section presents diagnostic diagrams comparing selected features, specifically Hβ vs Mgb and Hβ vs [MgFe]$'$. [MgFe]' was originally defined by Thomas et al. (2003) to be minimally sensitive to the abundance ratio [α/Fe], making it a robust tracer of the total metallicity [Z/H]. This index was computed using the relation:

$$[\mathrm{MgFe}]' = \sqrt{\mathrm{Mgb} \times (0.72 \times \mathrm{Fe5270} + 0.28 \times \mathrm{Fe5335})},$$

and the associated uncertainties were derived by standard error propagation, taking into account the individual errors in Mgb, Fe5270, and Fe5335. The plots show in Figure 4.2 illustrate the position of each galaxy in the index–index plane with respect to theoretical model grids composed of iso-metallicity and iso-age lines. Such grids enable a joint constraint on the stellar population age and metallicity, based on the galaxy's location in the diagram.

The reference grids used in this analysis are derived from the SPS models by Thomas et al. (2011a), which span a broad range of ages, total metallicities [Z/H], and [α/Fe] abundance ratios. These models provide theoretical predictions for the Lick indices measured at zero velocity dispersion ($\sigma = 0$). However, in observed galaxy spectra, the absorption features are broadened due to the internal stellar velocity dispersion of the galaxy, which alters the measured line strengths. To allow a meaningful comparison with the models, the observed Lick indices must be corrected to their equivalent values at $\sigma = 0$. This correction is performed following the approach introduced by Carson

et al. (2010), which uses synthetic spectra broadened to a range of velocity dispersions to measure how each index varies with σ. The resulting dependence is modeled with a polynomial function, allowing the observed indices to be deconvolved and rescaled to match the zero-velocity-dispersion model predictions.

Specifically, the grids in the following plots were computed over a discrete set of values:

- Ages (in Gyr): [0.6, 1.0, 2.0, 4.0, 6.0, 8.0, 10.0, 12.0]
- Metallicities [Z/H]: [-2.25, -1.35, -0.33, 0.0, 0.35, 0.67]

To correct the measured indices for the effect of the galaxy's internal velocity dispersion, the values of σ obtained from the full-spectral fitting with `Bagpipes` (described in a later section) were adopted. The correction is based on computing a correction index $C_I(\sigma)$, which expresses how each Lick index changes as a function of σ.

For atomic indices (measured in Å), the correction index is defined as:

$$C_I(\sigma) = \frac{\text{Index}(\sigma = 0)}{\text{Index}(\sigma)}, \tag{4.1}$$

where $C_I(\sigma)$ is a third-order polynomial of the form:

$$C_I(\sigma) = \sum_{i=0}^{3} b_i \, \sigma^i, \tag{4.2}$$

where the coefficients b_i are tabulated correction in Carson and Nichol (2010) and were computed for each Lick index.

The corrected Lick index at $\sigma = 0$ is then obtained by inverting the relation:

$$\text{Index}(\sigma = 0) = \text{Index}(\sigma) \cdot C_I(\sigma), \tag{4.3}$$

At higher σ values, the absorption lines become broader and shallower, leading to a systematic decrease in the measured index. By correcting to $\sigma = 0$, one removes the effect of this broadening, and the indices become larger, as they represent intrinsically narrower and deeper absorption features. The corrected and uncorrected index values are shown in the graphs below to emphasize the impact of the correction and to ensure a reliable comparison with the theoretical grids.

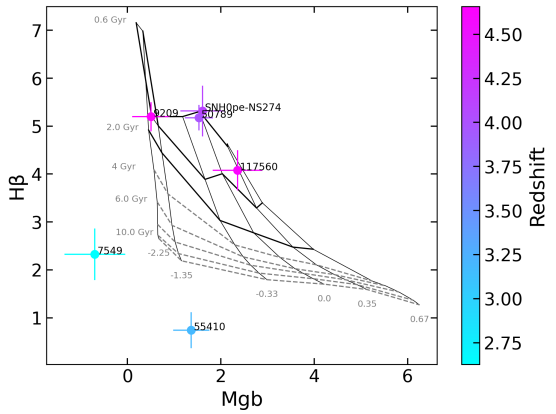

(a) $H\beta$ vs Mgb (uncorrected)

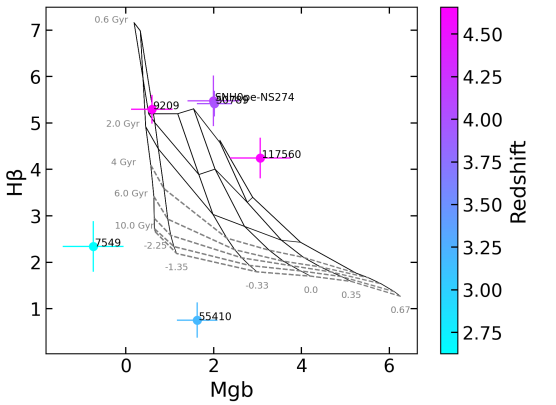

(b) $H\beta$ vs Mgb (corrected to $\sigma = 0$)

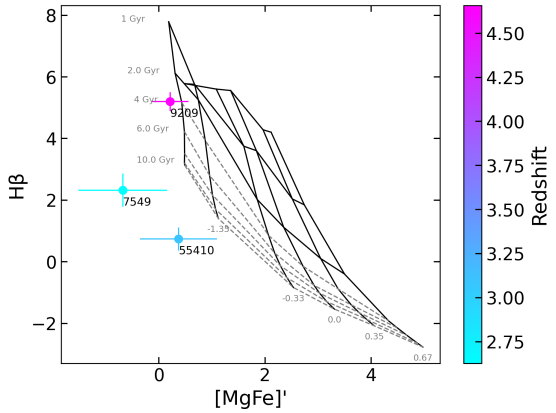

(c) $H\beta$ vs [MgFe]' (uncorrected)

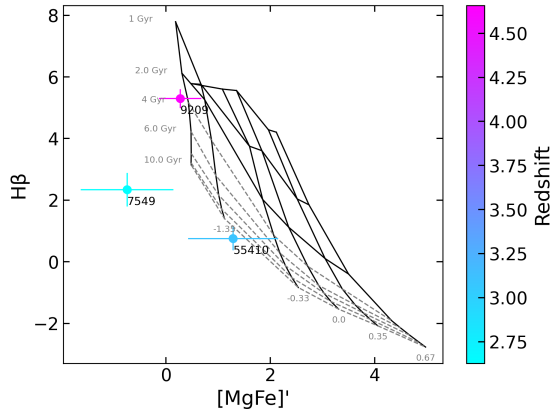

(d) $H\beta$ vs [MgFe]' (corrected to $\sigma = 0$)

Figure 4.2: Diagnostic plots comparing $H\beta$ with Mgb and [MgFe]', before and after correction to $\sigma = 0$. Galaxies are color-coded by redshift. The dashed lines indicate regions corresponding to non-physical solutions where the inferred stellar population ages exceed the age of the Universe predicted by the ΛCDM cosmological model.

The approach based on Lick indices provides an indicative first insight into the stellar properties of the galaxy sample. The results clearly reveal the presence of two distinct populations: a younger one, characterized by strong Balmer lines, and an older, more evolved population with stronger metal indices. However, these findings should be interpreted with caution. On the one hand, Balmer absorption lines may be affected by nebular emission, which reduces their observed equivalent width. On the other hand, the number of galaxies for which a reliable [MgFe]' index can be computed is limited, which

reduces the statistical robustness of the analysis. For these reasons, a more comprehensive and quantitative approach is required, based on full-spectral fitting, which allows simultaneous modeling of all components of the observed spectrum.

4.2 Full-spectral Fitting Analysis

To overcome these limitations and gain more robust constraints on stellar population parameters, a full-spectral fitting approach was adopted. With the methodology established in the previous sections, the analysis proceeded by preparing the observed spectra for fitting. This involved cleaning the data by removing bad pixels and masking specific regions of the spectrum corresponding to emission or absorption lines not due to the stellar component. These features, if not taken into account, could have adversely affected the quality of the fit.
For this reason, the following rest-frame lines were considered: [OII]λ3727.092Å, [OII]λ3729.875Å, CaII K (λ=3933.663Å), [OIII]λ4960.295Å, [OIII]λ5008.240Å, NaI (D2, λ=5890.0Å), NaI (D1, λ=5895.9Å), [NII]λ6549.86Å, Hα (λ=6564.61Å), [NII]λ6585.27Å. These lines were redshifted for each galaxy according to its spectroscopic redshift using the relation:

$$\lambda_{\rm obs} = \lambda_{\rm em} \cdot (1 + z). \tag{4.4}$$

The regions centered on the redshifted lines were masked using a window defined by:

$$\Delta\lambda = \lambda_{\rm obs} \cdot \frac{v}{c}, \tag{4.5}$$

with $v = 500$ km/s and c being the speed of light, to avoid contamination in the fitting process.

The spectra were then fitted within the rest-frame wavelength range:

$$3540\,\text{Å} < \lambda < 7350\,\text{Å}, \tag{4.6}$$

using the instruction dictionary described in section 2.4.1. For each galaxy, three different SFHs were tested: delayed, double power law, and non-parametric, resulting in three best-fit synthetic spectra. To explore the possibility that some high-redshift galaxies exhibit stellar population ages or SFHs incompatible with the ΛCDM cosmological model, the modified version of `Bagpipes` described in Section 2.5 was also used. This version removes the age constraint imposed by ΛCDM, allowing galaxy ages to exceed the age

of the Universe at the corresponding redshift. In particular, this allows testing whether the assumption that galaxy ages cannot exceed the age of the Universe holds true, or whether the data suggest potential tension with this cosmological constraint, opening the scenario described in section 1.3. Each galaxy was fitted also using this modified version, adopting both double power law and nonparametric SFHs, and allowing ages up to 5 Gyr. This process yielded two additional best-fit spectra per galaxy, for a total of five models per object.

During the fit, all synthetic spectra were rescaled (i.e. divided by $P(x)$) using a second-order Chebyshev polynomial to correct for systematic deviation as described in section 2.4.1. To quantitatively assess the fit quality, the reduced chi-squared statistic was computed:

$$\chi^2_\nu = \frac{1}{N-p} \sum_i \left(\frac{O_i - E_i}{\sigma_i} \right)^2 . \tag{4.7}$$

The test is used to evaluate how well a model fits the data, taking into account the number of degrees of freedom: N is the number of data points, p is the number of free parameters in the model, O_i are the observed values, E_i are the expected (model) values and σ_i are the uncertainties on the observed values.

To evaluate the effect of different SFH assumptions, for each galaxy, the spectra obtained with different SFHs were compared, and the normalized residuals were calculated

$$R = \frac{O_i - E_i}{\sigma_i} \tag{4.8}$$

These residuals provide a visual and quantitative indicator of how well each model reproduces the data and highlight regions with larger discrepancies as shown at the end of the section in the third panel of the Figure C.1.

Finally, contour plots were generated to compare the posterior distributions obtained using different SFH models for each galaxy (see. Figure 4.5(b)). These plots (while obtained for all the parameters included in the fit) were focused in particular on key physical parameters that are consistently defined across all SFH parameterizations: stellar mass, metallicity, dust attenuation (A_V), and velocity dispersion. This allows us to assess how different assumptions about the star formation history impact the derived properties. The contour plots are generally produced by `Bagpipes` as part of its Bayesian

inference framework, based on the sampling of the posterior distributions. However, in this analysis, the posterior chains were manually extracted from the output files for a selected subset of parameters that are common across the various models. For each parameter, the median value, as well as the 16th and 84th percentiles, were computed. They visualize the joint probability distributions between pairs of parameters, with contours representing the 68% confidence levels. This manual extraction enabled a direct and homogeneous comparison of key physical properties under investigation. Narrow contours indicate well-constrained parameters, while elongated or tilted contours reveal correlations or degeneracies. These plots, therefore, serve as a powerful diagnostic tool for evaluating the robustness of parameter estimates and understanding how they vary under different SFH assumptions.

Based on the fitting results, the galaxies in the sample were classified into two categories: those that remain compatible with the ΛCDM cosmological model, and those that potentially exhibit a tension with the model. The results for each galaxy are presented below, grouped according to this classification.

4.3 No Tension with the ΛCDM Model

In this section, the results obtained by fitting the galaxies with `Bagpipes` are presented for those galaxies that appear to be consistent with the ΛCDM model.

To maintain clarity and keep the main text concise, detailed spectral fitting results are provided in Appendix C.

The following tables (Tab. 4.2, 4.3, 4.4, 4.5, and 4.6) report the estimated values of all parameters derived from different SFH models — namely, delayed exponential, double power law, non-parametric, and both double power law and nonparametric models without the cosmological (ΛCDM) prior — to enable direct comparison.

Model	calib:0	calib:1	calib:2	noise	age	massformed	metallicity	Av	veldisp	alpha	beta	tau	B	delta	eta	z
delayed	1.05	-0.01	0.003	1.30	$0.29^{-0.08}_{+0.15}$	$10.89^{-0.04}_{+0.05}$	$2.37^{-0.38}_{+0.29}$	$0.53^{-0.10}_{+0.11}$	345^{-21}_{+20}	/	/	0.08	0.91	-0.01	4.05	4.11
dblplaw	1.05	-0.01	0.004	1.29	$0.31^{-0.15}_{+0.06}$	$10.89^{-0.03}_{+0.04}$	$2.31^{-0.33}_{+0.25}$	$0.54^{-0.09}_{+0.10}$	343^{-20}_{+21}	12.17	173.47	1.12	0.85	-0.01	3.99	4.11
nonparametric	1.07	-0.008	-0.001	1.29	$0.39^{-0.25}_{+0.69}$	$10.94^{-0.03}_{+0.03}$	$2.26^{-0.31}_{+0.30}$	$0.33^{-0.09}_{+0.09}$	347^{-18}_{+19}	/	/	/	1.00	0.10	3.22	4.11
dblplaw_nocosmo	1.05	-0.01	0.004	1.29	$0.28^{-0.14}_{+0.08}$	$10.89^{-0.04}_{+0.04}$	$2.36^{-0.31}_{+0.31}$	$0.54^{-0.09}_{+0.10}$	345^{-20}_{+22}	45.97	336.85	4.65	0.89	-0.01	3.88	4.11
nonparametric_nocosmo	1.06	-0.006	-0.000	1.29	$0.4^{-0.25}_{+0.89}$	$10.94^{-0.04}_{+0.03}$	$2.21^{-0.32}_{+0.32}$	$0.39^{-0.09}_{+0.10}$	346^{-19}_{+20}	/	/	/	0.86	0.08	3.64	4.11

Table 4.2: Parameters derived from the `Bagpipes` fit (except for the age, which is presented in subsection 2.4.2 and discussed in more detail in Appendix A) considering different SFH models. Galaxy SNH0pe-NS274

Model	calib:0	calib:1	calib:2	noise	age	massformed	metallicity	Av	veldisp	alpha	beta	tau	B	delta	eta	z
delayed	1.96	0.49	0.03	1.46	$0.12^{-0.03}_{+0.02}$	$10.80^{-0.02}_{+0.02}$	$2.07^{-0.12}_{+0.14}$	$0.61^{-0.02}_{+0.02}$	325^{-12}_{+11}	/	/	0.02	0.12	-0.29	3.04	4.66
dblplaw	1.82	-0.02	-0.10	1.49	$0.74^{0.01}_{0.06}$	$10.99^{-0.01}_{+0.01}$	$0.01^{-0.00}_{+0.00}$	$0.01^{-0.01}_{+0.02}$	288^{-12}_{+13}	176.0	4.46	0.63	2.03	0.11	2.92	4.66
nonparametric	1.90	0.32	-0.14	1.49	$0.56^{-0.30}_{+0.48}$	$10.94^{-0.02}_{+0.02}$	$0.08^{-0.01}_{+0.01}$	$0.18^{-0.04}_{+0.04}$	292^{-12}_{+12}	/	/	/	0.17	-0.22	3.08	4.66
dblplaw_nocosmo	1.82	0.24	-0.12	1.49	$0.30^{-0.04}_{+0.04}$	$10.83^{-0.01}_{+0.01}$	$0.03^{-0.01}_{+0.01}$	$0.30^{-0.01}_{+0.02}$	311^{-13}_{+14}	665.2	693.1	4.68	0.12	-0.27	2.98	4.66
nonparametric_nocosmo	1.92	0.39	-0.14	1.48	$0.48^{-0.24}_{+1.39}$	$10.95^{-0.02}_{+0.02}$	$0.08^{-0.01}_{+0.01}$	$0.26^{-0.03}_{+0.03}$	295^{-11}_{+11}	/	/	/	0.10	-0.28	3.25	4.66

Table 4.3: Same as 4.2, Galaxy 9209

Model	calib:0	calib:1	calib:2	noise	age	massformed	metallicity	Av	veldisp	alpha	beta	tau	B	delta	eta	z
delayed	2.13	-0.26	0.07	1.49	$0.32^{-0.10}_{+0.05}$	$11.17^{-0.04}_{+0.04}$	$2.60^{-0.14}_{+0.19}$	$0.56^{-0.09}_{+0.09}$	400^{-18}_{+17}	/	/	0.04	4.29	0.19	1.98	3.99
dblplaw	2.14	-0.24	0.07	1.48	$0.4^{-0.12}_{+0.28}$	$11.20^{-0.03}_{+0.03}$	$2.48^{-0.14}_{+0.14}$	$0.58^{-0.07}_{+0.07}$	395^{-17}_{+17}	349.37	5.00	1.35	3.96	0.24	2.96	3.99
nonparametric	2.13	-0.25	0.07	1.48	$0.32^{-0.10}_{+0.26}$	$11.17^{-0.03}_{+0.03}$	$2.54^{-0.15}_{+0.15}$	$0.51^{-0.08}_{+0.08}$	397^{-14}_{+14}	/	/	/	4.35	0.21	1.52	3.99
dblplaw_nocosmo	2.11	-0.23	0.07	1.49	$0.32^{-0.10}_{+0.06}$	$11.19^{-0.03}_{+0.03}$	$2.52^{-0.11}_{+0.12}$	$0.65^{-0.08}_{+0.07}$	398^{-16}_{+16}	83.95	374.98	4.64	4.25	0.22	1.64	3.99
nonparametric_nocosmo	2.14	-0.25	0.07	1.47	$0.39^{-0.11}_{+0.13}$	$11.17^{-0.03}_{+0.03}$	$2.48^{-0.15}_{+0.12}$	$0.52^{-0.08}_{+0.07}$	395^{-13}_{+13}	/	/	/	4.46	0.21	1.42	3.99

Table 4.4: Same as 4.2, Galaxy 50789

Model	calib:0	calib:1	calib:2	noise	age	massformed	metallicity	Av	veldisp	alpha	beta	tau	B	delta	eta	redshift
delayed	1.02	0.01	-0.07	1.48	$0.57^{-0.18}_{+0.09}$	$11.25^{-0.04}_{+0.06}$	$0.06^{-0.02}_{+0.02}$	$1.16^{-0.11}_{+0.12}$	271^{-30}_{+32}	/	/	0.08	3.42	-0.22	3.02	4.62
dblplaw	1.03	-0.00	-0.07	1.48	$0.54^{-0.15}_{+0.29}$	$11.24^{-0.05}_{+0.06}$	$0.06^{-0.02}_{+0.02}$	$1.14^{-0.10}_{+0.13}$	266^{-31}_{+34}	172.91	2.31	0.94	3.41	-0.21	3.03	4.62
nonparametric	1.02	-0.00	-0.06	1.48	$0.54^{-0.28}_{+0.30}$	$11.22^{-0.04}_{+0.04}$	$0.06^{-0.02}_{+0.02}$	$1.15^{-0.08}_{+0.10}$	263^{-29}_{+28}	/	/	/	3.62	-0.24	3.08	4.62
dblplaw_nocosmo	1.01	0.01	-0.07	1.47	$0.51^{-0.21}_{+0.09}$	$11.22^{-0.03}_{+0.03}$	$0.06^{-0.02}_{+0.02}$	$1.22^{-0.10}_{+0.11}$	260^{-23}_{+22}	33.37	315.62	4.39	3.65	-0.26	3.20	4.62
nonparametric_nocosmo	1.02	0.00	-0.06	1.47	$0.54^{-0.24}_{+0.22}$	$11.22^{-0.03}_{+0.04}$	$0.06^{-0.02}_{+0.03}$	$1.17^{-0.08}_{+0.10}$	261^{-28}_{+30}	/	/	/	3.69	-0.25	3.20	4.62

Table 4.5: Same as 4.2, Galaxy 109760

Model	calib:0	calib:1	calib:2	noise	age	massformed	metallicity	Av	veldisp	alpha	beta	tau	B	delta	eta	redshift
delayed	1.75	-0.003	-0.01	1.37	$0.62^{-0.10}_{+0.05}$	$11.25^{-0.03}_{+0.05}$	$0.54^{-0.07}_{+0.08}$	$0.57^{-0.09}_{+0.13}$	389^{-20}_{+21}	/	/	0.047	3.18	-0.09	2.97	4.62
dblplaw	1.76	-0.004	-0.004	1.37	$0.63^{-0.13}_{+0.26}$	$11.25^{-0.03}_{+0.05}$	$0.52^{-0.07}_{+0.10}$	$0.56^{-0.09}_{+0.12}$	384^{-23}_{+26}	174.15	2.29	0.83	3.11	-0.09	2.96	4.62
nonparametric	1.73	-0.01	0.02	1.38	$0.65^{-0.33}_{+0.44}$	$11.25^{-0.03}_{+0.03}$	$0.63^{-0.10}_{+0.11}$	$0.59^{-0.07}_{+0.09}$	389^{-21}_{+23}	/	/	/	3.57	-0.20	3.17	4.62
dblplaw_nocosmo	1.63	-0.04	0.08	1.40	$0.47^{-0.29}_{+0.14}$	$11.27^{-0.04}_{+0.04}$	$0.63^{-0.08}_{+0.08}$	$1.13^{-0.08}_{+0.09}$	383^{-15}_{+16}	18.51	293.91	4.37	3.04	-0.16	3.60	4.62
nonparametric_nocosmo	1.75	-0.01	0.01	1.38	$0.68^{-0.21}_{+0.52}$	$11.24^{-0.03}_{+0.03}$	$0.58^{-0.09}_{+0.11}$	$0.57^{-0.07}_{+0.09}$	389^{-21}_{+23}	/	/	/	3.30	-0.19	3.22	4.62

Table 4.6: Same as 4.2, Galaxy 117560

4.3.1 Consistency Across Different SFH Models

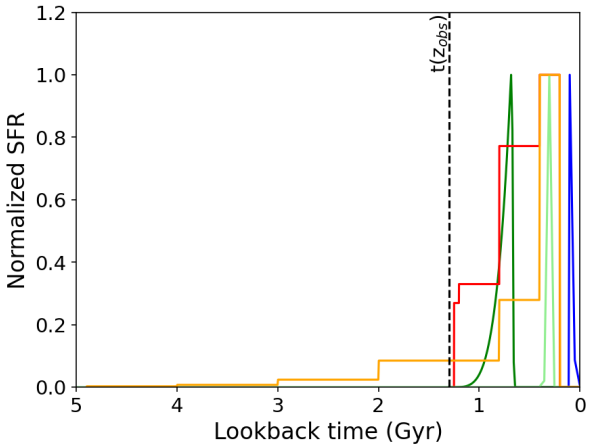

(a) SFHs comparison, Galaxy 9209

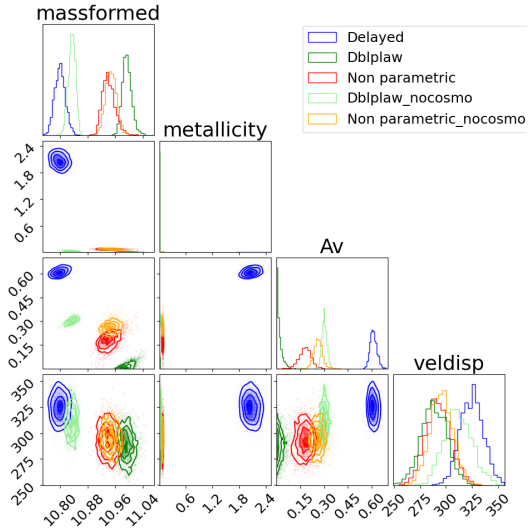

(b) Contour plot comparison, Galaxy 9209

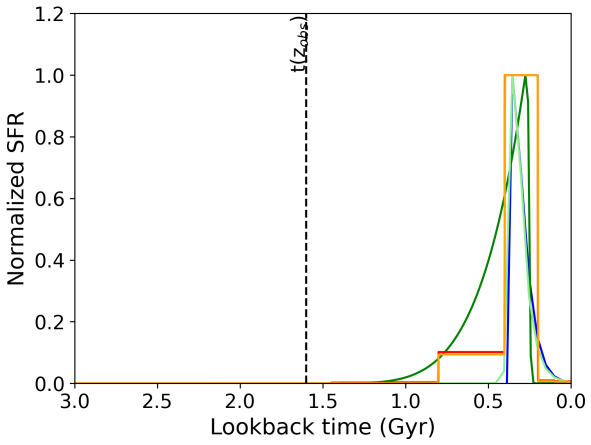

(c) SFHs comparison, Galaxy 50789

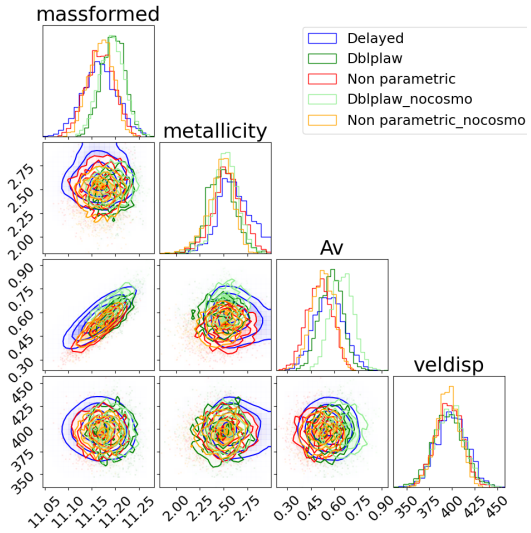

(d) Contour plot comparison, Galaxy 50789

Figure 4.3: Comparison between the star formation histories and the posterior distributions of key physical parameters obtained using the five models described in the thesis. The left panel shows the SFHs, derived from `Bagpipes` best-fit solutions, as a function of lookback time and normalized to their peak value, in order to highlight differences in shape. The right panel displays contour plots comparing the posterior distributions of total stellar mass formed, stellar metallicity, dust attenuation (A_V), and velocity dispersion across the different SFH models. In both panels, the colors correspond to the SFH model used, as indicated in the legend.

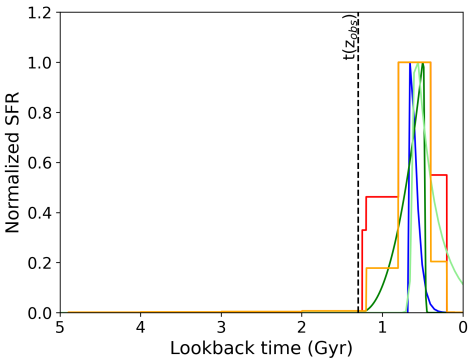

(a) SFHs comparison, Galaxy 117560

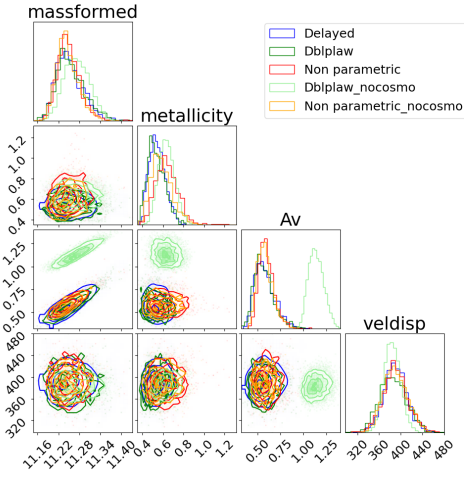

(b) Contour plot comparison, Galaxy 117560

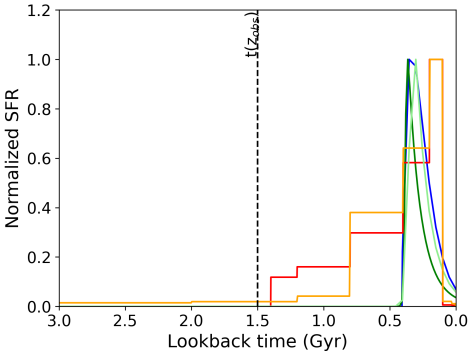

(c) SFHs comparison, Galaxy SNH0pe-NS274

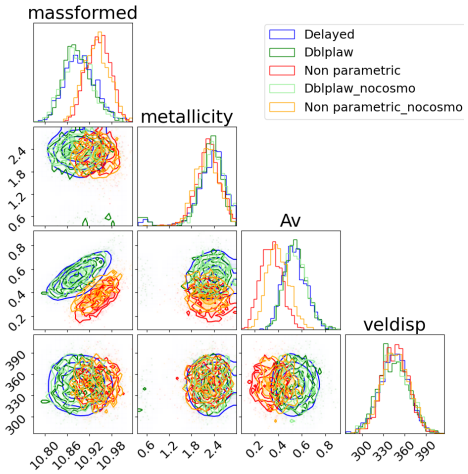

(d) Contour plot comparison, Galaxy SNH0pe-NS274

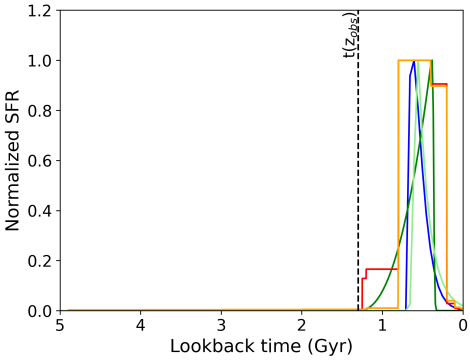

(e) SFHs comparison, Galaxy 109760

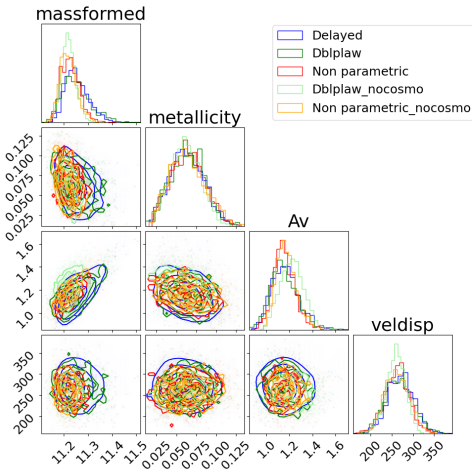

(f) Contour plot comparison, Galaxy

Figure 4.4: Same as Fig 4.3

For galaxies that do not show tension with the ΛCDM model – specifically 50789, 109760, 117560, and SNH0pe-NS274 – the estimated parameters obtained from different SFHs are highly consistent, as shown by the tables above (see Tables 4.4, 4.5, 4.6, 4.2). Despite the intrinsic differences between the functional forms used (e.g., delayed, double power-law, non-parametric), the resulting SFHs all consistently peak at the same epoch and provide a coherent picture of the stellar mass assembly independent of the assumed SFH functional form.

This consistency is clearly visible both in the SFH plots and in the posterior distributions of the contour plots (shown in Fig. 4.3, 4.4), where parameters such as age, mass, metallicity, and dust attenuation are in excellent agreement across all SFH models. This is a significant result, because it means that the ages and SFH for this population can be very robustly retrieved, independently of the choice of SFH or the fact that the age could vary independently of any cosmological prior.

It is worth noting that in the case of galaxy SNH0pe-NS274 (see Fig. 4.4(c), the non-parametric SFHs are more extended in time compared to the delayed or DPL models, but the peaks still coincide well, suggesting a robust estimate of the formation epoch. The tabulated values also reflect this agreement, with age estimates converging to similar values regardless of the chosen SFH, which enhances the reliability of the derived stellar population properties.

Galaxy 9209 represents a more complex case (see Fig. 4.3(a)). Here, the various SFHs give quite different results: the delayed and DPL models produce very narrow and early-peaking SFHs, while the nonparametric models are more extended in time and peak at later epochs. This inconsistency among the SFHs results in significant discrepancies in the estimated physical parameters, especially metallicity and dust attenuation. The contour plots for this galaxy highlight a lack of convergence, with each SFH tracing different regions of parameter space, likely due to stronger degeneracies between age, dust, and metallicity. In this case, the choice of SFH has a major impact on inferred properties, making it harder to robustly constrain the evolutionary history of the galaxy.

Interestingly, regardless of the consistency or inconsistency among the SFH models, the spectral fits remain remarkably good for all galaxies (see Appendix C). The best-fit spectra generated by each SFH, once calibrated using the polynomial correction, closely match the observed spectra. This is reflected in reduced values of χ^2 that typically range from ~ 1.5 to 2.5, indicating a good fit to the data.

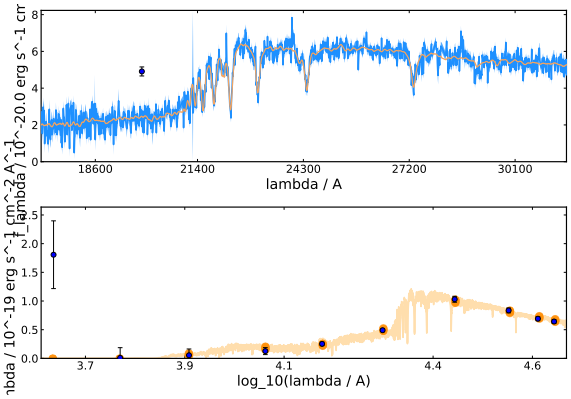

(a) Fit obtained with a double power-law SFH model without applying a cosmological prior, for galaxy 117560.

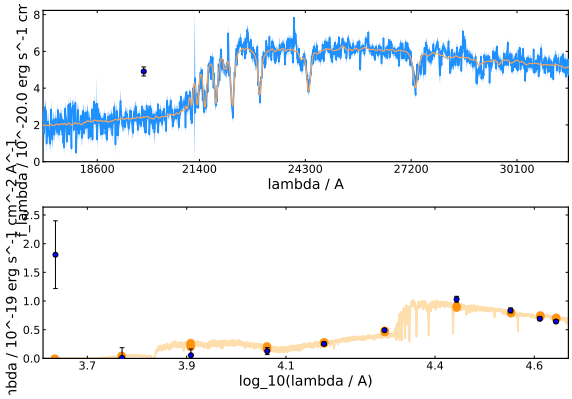

(b) Fit obtained with a double power-law SFH model applying a cosmological prior, for galaxy 117560.

Figure 4.5: Comparison of the photometric fits for galaxy 117560. The fit with the cosmological prior (left) better matches the photometric data, while the fit without the prior (rigth) shows a poorer agreement. This difference explains the divergent results obtained using the double power-law SFH model without the cosmological prior.

A noteworthy case is galaxy 117560 (see spectral results illustrated in Appendix C), where the best-fit model produced using a double power-law SFH without cosmological prior appears significantly lower than the others before calibration. This is due to a poor fit to certain photometric points, which leads to an underestimated flux level as shown in Figure 4.5. As a consequence, the model compensates for this discrepancy by favoring significantly higher dust attenuation (A_V), in order to reconcile the model spectrum with the data. This leads to a dust value that is noticeably higher compared to those derived from the other SFH assumptions, and it also impacts the derived mass and metallicity (see 4.4(b)). This behavior is reflected in the parameter contours, where the estimates from this model are clearly offset with respect to the others. However, after calibration, the spectrum becomes consistent with the others.

These findings suggest that when SFHs converge, they provide reliable and physically consistent interpretations of galaxy evolution, supporting the idea that for some galaxies the inference is relatively insensitive to the exact SFH parametrization. Conversely, for galaxies like 9209, the degeneracy among parameters remains strong, and additional constraints may be required to break it.

Comparison with Existing Results

The galaxies 117560, 109760, and 50789 all exhibit high stellar masses, on the order of $10^{11}\,M_{\odot}$. However, they show significant differences in terms of metallicity, dust content, and velocity dispersion. 117560 has a super-solar metallicity of approximately $2.2\,Z_{\odot}$, moderate dust attenuation ($A_V \approx 0.38$), and a very high stellar velocity dispersion of 360 km/s. In contrast, 109760 displays sub-solar metallicity, around $0.39\,Z_{\odot}$, with a relatively high dust attenuation ($A_V \approx 0.84$) and a much lower velocity dispersion of 140 km/s. Finally, 50789 shows similarly super-solar metallicity ($\sim 2.1\,Z_{\odot}$), intermediate dust attenuation ($A_V \approx 0.49$), and a velocity dispersion of 370 km/s.

When compared with our results, we find good agreement for the stellar masses, which are consistently above $10^{11}\,M_{\odot}$. The velocity dispersions for galaxies 117560 and 50789 are in line with the values reported in the literature. Galaxy 109760 shows a lower velocity dispersion but slightly higher with respect to the one estimated by Carnall et al. (2024b). Similarly, the dust attenuation values are consistent in trend but tend to be higher in our results. The same holds for stellar metallicities, which are slightly overestimated in our fits.

Additional comparison with the galaxies NH0pe-NS274 and 9209 also shows good overall consistency. Both galaxies have slightly lower stellar masses, around $\log(M_*/M_{\odot}) \approx 10.8$, which agrees well with our estimates. In terms of metallicity, NS274 has a reported $\log(Z/Z_{\odot}) = 0.46$, in agreement with our value grater than $2\,Z_{\odot}$. For 9209, the metallicity is $\log(Z/Z_{\odot}) = 0.11$, also consistent with our findings. The dust attenuation values are similarly well matched: NS274 has $A_V = 0.44$, and 9209 shows a very low attenuation of $A_V = 0.02$, which is compatible with our results for the specific double power law model. The velocity dispersions of these two galaxies, 330 km/s for NS274 and 270 km/s for 9209, are also consistent with those obtained in our analysis.

It is important to note that this comparison is indicative, as the literature values are derived from a specific set of assumptions. In particular, they do not explore the full range of SFHs tested in our work.

4.4 Tension with ΛCDM

This section presents results for the two galaxies that seem to be in tension with the ΛCDM model. The findings are presented using the same set of graphs and tables as in

the previous section. The full-spectral analysis is included in Appendix C.

These galaxies exhibit age estimates that approach or exceed the age of the Universe at their observed redshifts, creating tensions with the ΛCDM model, which imposes limits on the maximum possible age of any object. This motivates a deeper investigation into the role of SFH parametrization, model degeneracies, and the influence of priors.

The following tables (tab. 4.7, 4.8) report the estimates of all parameters to allow for comparison.

Model	calib:0	calib:1	calib:2	noise	age	massformed	metallicity	Av	veldisp	alpha	beta	tau	B	delta	eta	z
delayed	1.89	-0.14	0.19	2.66	$1.59\ ^{-0.55}_{+0.29}$	$10.93\ ^{-0.05}_{+0.05}$	$0.26\ ^{-0.07}_{+0.07}$	$0.89\ ^{-0.11}_{+0.13}$	$187\ ^{-41}_{+49}$	/	/	0.25	2.62	-0.11	3.17	2.63
dblplaw	1.90	-0.14	0.19	2.67	$1.60\ ^{-0.65}_{+0.68}$	$10.96\ ^{-0.04}_{+0.05}$	$0.23\ ^{-0.08}_{+0.08}$	$0.92\ ^{-0.12}_{+0.12}$	$177\ ^{-39}_{+43}$	140.40	0.05	1.68	2.38	-0.04	3.00	2.63
nonparametric	1.89	-0.15	0.19	2.67	$1.63\ ^{-0.73}_{+0.54}$	$10.96\ ^{-0.04}_{+0.05}$	$0.28\ ^{-0.07}_{+0.07}$	$0.93\ ^{-0.11}_{+0.14}$	$184\ ^{-40}_{+49}$	/	/	/	2.60	-0.04	3.21	2.38
dblplaw_nocosmo	1.90	-0.15	0.19	2.66	$2.62\ ^{-1.53}_{+1.87}$	$11.05\ ^{-0.04}_{+0.04}$	$0.26\ ^{-0.09}_{+0.08}$	$0.91\ ^{-0.13}_{+0.12}$	$177\ ^{-35}_{+43}$	212.03	0.28	4.50	2.46	-0.02	3.04	2.63
nonparametric_nocosmo	1.89	-0.15	0.19	2.67	$2.42\ ^{-1.48}_{+1.79}$	$11.05\ ^{-0.04}_{+0.05}$	$0.27\ ^{-0.08}_{+0.09}$	$0.89\ ^{-0.12}_{+0.13}$	$184\ ^{-41}_{+49}$	/	/	/	2.63	-0.08	3.06	2.63

Table 4.7: Parameters derived from the `Bagpipes` fit (except for the age, which is presented in subsection 2.4.2 and discussed in more detail in Appendix A) considering different SFH models. Galaxy 7549

Model	calib:0	calib:1	calib:2	noise	age	massformed	metallicity	Av	veldisp	alpha	beta	tau	B	delta	eta	z
delayed	1.26	-0.04	-0.007	1.36	$1.56\ ^{-0.35}_{+0.18}$	$11.41\ ^{-0.02}_{+0.02}$	$1.98\ ^{-0.13}_{+0.11}$	$0.17\ ^{-0.05}_{+0.06}$	$308\ ^{-18}_{+20}$	/	/	0.16	2.71	-0.15	3.34	3.20
dblplaw	1.27	-0.05	-0.006	1.36	$1.5\ ^{-0.38}_{+0.39}$	$11.40\ ^{-0.02}_{+0.02}$	$1.94\ ^{-0.14}_{+0.19}$	$0.16\ ^{-0.05}_{+0.06}$	$305\ ^{-18}_{+19}$	112.81	0.03	0.97	2.45	-0.12	2.89	3.20
nonparametric	1.26	-0.09	0.002	1.35	$1.41\ ^{-0.54}_{+0.45}$	$11.38\ ^{-0.02}_{+0.02}$	$2.96\ ^{-0.05}_{+0.03}$	$0.09\ ^{-0.04}_{+0.04}$	$318\ ^{-15}_{+15}$	/	/	/	2.52	-0.07	3.07	3.20
dblplaw_nocosmo	1.26	-0.06	0.001	1.35	$2.77\ ^{-1.71}_{+1.75}$	$11.54\ ^{-0.02}_{+0.02}$	$1.80\ ^{-0.22}_{+0.18}$	$0.12\ ^{-0.05}_{+0.06}$	$308\ ^{-17}_{+19}$	269.58	0.03	4.37	2.73	-0.07	2.90	3.20
nonparametric_nocosmo	1.26	-0.09	0.003	1.35	$1.78\ ^{-0.80}_{+0.95}$	$11.38\ ^{-0.02}_{+0.02}$	$2.95\ ^{-0.07}_{+0.03}$	$0.11\ ^{-0.05}_{+0.05}$	$320\ ^{-18}_{+18}$	/	/	/	2.38	-0.08	3.24	3.20

Table 4.8: Parameters derived from the `Bagpipes` fit ((except for the age, which is presented in subsection 2.4.2 and discussed in more detail in Appendix A) considering different SFH models. Galaxy 55410

4.4.1 Consistency Across Different SFH Models

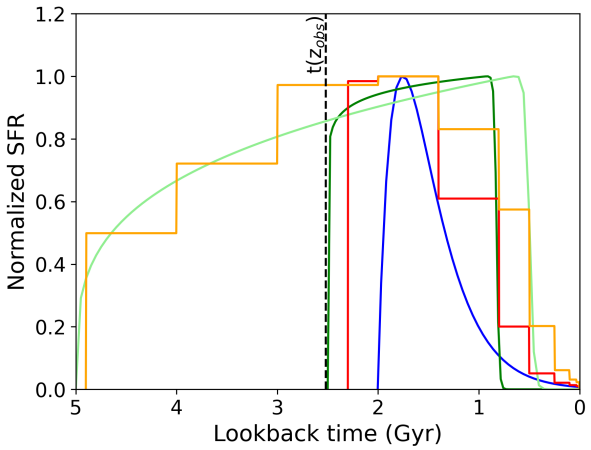

(a) SFHs comparison, Galaxy 7549

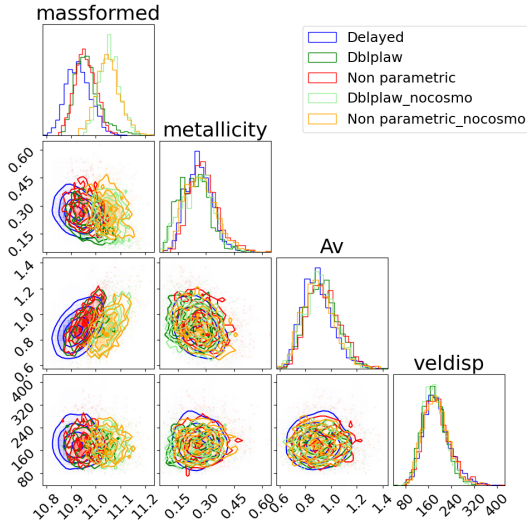

(b) Contour plot comparison, Galaxy 7549

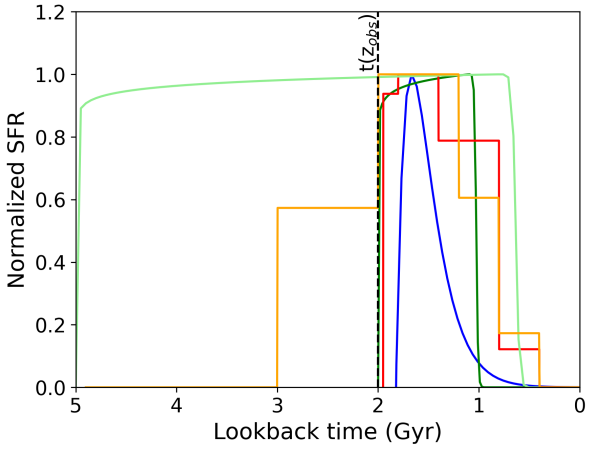

(c) SFHs comparison, Galaxy 55410

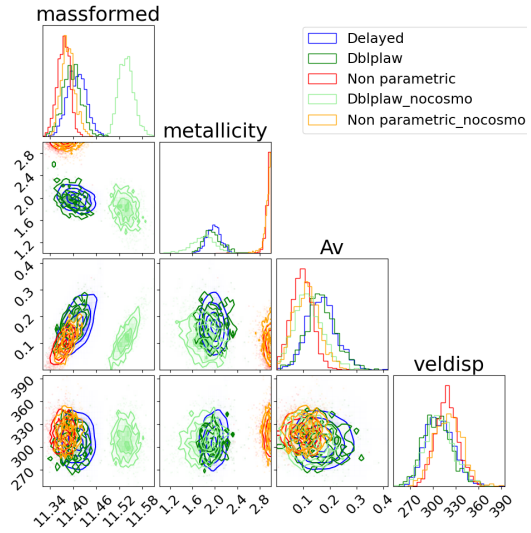

(d) Contour plot comparison, Galaxy 55410

Figure 4.6: Same as Fig. 4.3

Among the analyzed sample, galaxies 55410 and 7549 stand out due to their inferred stellar population ages and formation epochs, which appear in tension with the standard ΛCDM cosmological model. For both galaxies, the SFHs that include a cosmological prior (namely the delayed, double power-law, and nonparametric models with a formation time constraint) yield consistent results. Despite differences in functional form, these SFHs all converge toward a peak of star formation at approximately the same epoch, suggesting a relatively well-constrained formation history under cosmological assumptions. However, when the cosmological prior is removed, the resulting SFHs become substantially more extended in time, with significant star formation persisting up to ~ 5 Gyr. This extension leads to a broader range of allowed ages. Differently from other galaxies in the sample, here the SFHs appear to be strongly influenced by the prior on age, effectively pushing the inferred formation redshifts to very high values, often beyond what is typically expected in a ΛCDM framework.

In galaxy 7549, the parameter estimates remain broadly consistent across all SFHs, as shown by both the contour plots (Fig. 4.6(a), 4.6(b)) and the tabulated values (Tab. 4.7). Some variation is observed in the stellar mass formed, which depends on the adopted SFH shape. For galaxy 55410, the situation is more degenerate (see Fig. 4.6(c), 4.6(d)): metallicity and mass estimates vary more substantially among the different models, indicating that the inferred properties are more sensitive to the SFH assumptions.

Despite these variations in the SFHs and physical parameters, the spectral fits remain of high quality for both galaxies (as shown in the Appendix C. The best-fit spectra closely match the observed data, with reduced χ^2 values indicating good fits across all models. It should be noted, however, that the spectrum of galaxy 7549 is significantly noisier than the others, which results in a higher χ^2 value.

Nonetheless, the consistency of the fits reinforces the idea that multiple SFHs can reproduce the observed spectra equally well, even when the underlying physical interpretations diverge. This observation opens up the issue of degeneracy: very different star formation histories can produce nearly identical spectra by combining a dominant old stellar population with a smaller fraction of younger stars (as shown by SFHs without cosmological prior). This degeneracy complicates the interpretation of physical parameters such as age and mass assembly timescale.

Comparison with Existing Results

The findings for galaxy 55410 agree with Carnall et al. (2024b). They found it to be ultra-massive with $\log(M_*/M_\odot) \approx 11.2$, having formed most of its stars rapidly within 0.25 Gyr at $z \sim 4.7$. The stellar population is α-enhanced ([Mg/Fe] ≈ 0.4) and shows high metallicity ($\log_{10}(Z_*/Z_\odot) = 0.35^{+0.07}_{-0.08}$, about twice solar), indicating fast chemical enrichment.

Our results are consistent with these findings, with stellar masses greater than $10^{11} M_\odot$ and metallicities around twice solar. Such early, rapid formation and quenching challenge the standard ΛCDM model, which predicts more extended growth for massive galaxies. To reconcile such rapid formation with the constraints of the standard ΛCDM cosmological framework, Carnall et al. (2024a) suggest an extremely high efficiency of gas-to-star conversion, close to 100%, which enables the assembly of this massive stellar population within a very short timescale. This scenario supports the interpretation of 55410 as an extreme case of early galaxy formation.

Similarly, galaxy 7549 shows a rapid assembly and early quenching as described in Park et al. (2024a). 7549 is a massive quiescent galaxy with a stellar mass of $\log(M_*/M_\odot) \approx 11.0$ and a metallicity close to solar, consistent with the values we find in our analysis as summarized in Table 4.7.

4.5 Age-Redshift relation

The analysis of this sample of galaxies within the redshift range $3 \lesssim z \lesssim 5$ reveals a wide diversity of results. Some galaxies exhibit SFHs and ages or stellar masses that tend to challenge or push the limits of the ΛCDM cosmological model, while others remain fully consistent with it. This variation is due to differences in parameter degeneracies. In some galaxies, the full-spectral fitting yields well-constrained SFHs and ages, with minimal degeneracy, making the results–especially the stellar age–robust and consistent with the ΛCDM model. In other cases, stronger degeneracies lead to less reliable parameter estimates, which can artificially produce tensions with cosmological expectations.

The results are summarized in Figure 4.7: In each panel, the black dashed curve represents the age of the Universe as a function of redshift, calculated using the standard cosmological parameters ($H_0 = 67.7$ km/s/Mpc,$\Omega_b = 0.05$, $\Omega_m = 0.31$, $\Omega_\Lambda = 0.68$). Valid physical solutions must lie below this curve, as no galaxy can be older than the

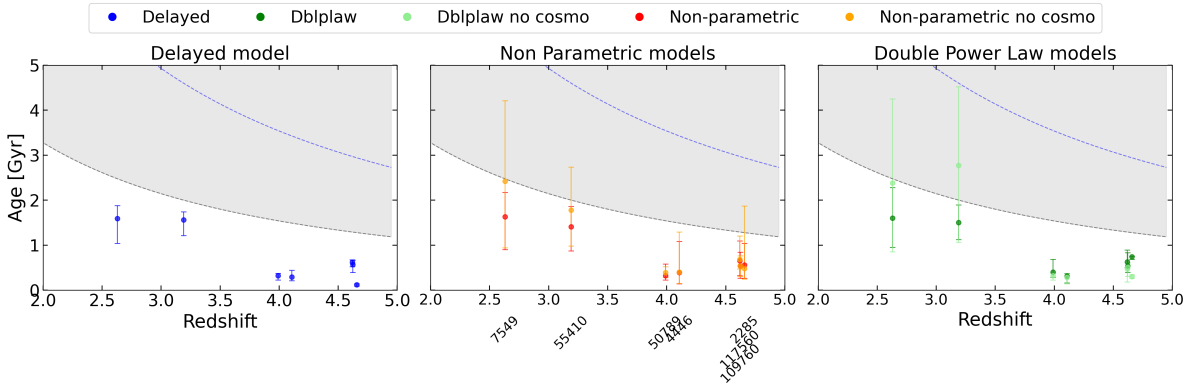

Figure 4.7: Mass-weighted ages as a function of redshift derived considering different SFH, with and without a cosmological prior. The left panel shows the results considering a delayed-τ model, the central one a nonparametric model, and the right one a double power-law model. The grey shaded area shows the range of ages not allowed considering a standard ΛCDM cosmology. The black dashed line shows the age–redshift relation assuming a fiducial ΛCDM model with $H_0 = 67.7$ km s^{-1} Mpc^{-1} and $\Omega_m = 0.31$. The blue line corresponds to an extreme cosmological scenario with a lower Hubble constant ($H_0 = 30$ km s^{-1} Mpc^{-1}), which allows for significantly older cosmic ages at a given redshift.

Universe at its observed redshift (if the cosmological model and the age determinations are correct). These results offer a critical perspective on the so-called "ΛCDM-breaking" galaxies often reported in the literature. These galaxies are claimed to challenge the standard cosmological model by showing SFHs that peak at extremely high redshifts, forming large stellar masses when the Universe was still very young. However, the present analysis suggests that such extreme star formation scenarios may often be artifacts induced by the choice of cosmological priors. When a prior on cosmic age is imposed, the SFH can be artificially compressed against this boundary, forcing the model to fit a significant fraction of stellar mass formation at unphysically high redshifts.

By relaxing the cosmological prior and allowing the age of the stellar population to vary freely, it is found that in some cases the model prefers ages that even exceed the age of the Universe, clearly an unphysical solution. Rather than indicating a real tension with ΛCDM, this effect likely reflects the model's difficulty in constraining the onset of star formation. In these situations, the fitting procedure pushes the solution toward the edge of the prior space.

Moreover, if one were to assume that the inferred stellar ages are accurate and that the underlying models and assumptions are fully valid, such early star formation would imply a Universe significantly older than that allowed by the standard ΛCDM cosmology. For example, reconciling the onset of SFH at 3 or 5 Gyr, such as in the extreme cases at redshifts $z \sim 2.6-3.1$, where the cosmic age is only $\sim 2.1-2.5$ Gyr, would require an extremely low Hubble constant, on the order of $H_0 \sim 30$ km/s/Mpc (as shown by the blue dashed line in Fig 4.7). This would correspond to a Universe over 30 Gyr old – an age completely inconsistent with the wealth of cosmological observations, which robustly constrain H_0 to values around 70 km/s/Mpc. This highlights that the extreme SFHs inferred in some cases are not plausible indicators of cosmological inconsistency, but are instead byproducts of modeling degeneracies.

The contrast opens up a broader discussion. In some cases, different SFH parameterizations, such as various parametric forms, lead to consistent and similar results that match the observed spectrum. In other cases, particularly those where the nonparametric SFH suggests a tension with ΛCDM, there appears to be a strong spectral degeneracy. This means that different SFH shapes, corresponding to different combinations of young and old stellar populations, can produce nearly indistinguishable spectra, making it difficult to discriminate between distinct star formation scenarios.

Galaxies 7549 and 55410 provide clear examples that illustrate all of the aforementioned behavior. The core of the degeneracy resides in the fact that fully consistent spectral and physical parameter results can be obtained from significantly different SFH shapes. This suggests that the inclusion of an older stellar population does not necessarily alter the resulting spectrum. The explanation lies in the limited contribution of old stars to the observed light, due to their intrinsic faintness. As a result, their presence can be effectively masked by a sufficiently young and luminous stellar population that dominates the galaxy's light output.

But how young must this population be to effectively balance the contribution of the older stars? The younger component must be both recent and bright enough to counteract the faint emission from the older population, ensuring that the overall SED remains consistent with the observations.

Notably, even when removing the cosmological prior leads to SFHs extending beyond the age of the Universe, the median stellar age remains relatively stable. This suggests that while the onset of star formation is often poorly constrained, the average age–and especially its evolution with redshift–emerges as a more robust quantity. This provides

encouraging prospects for using these galaxies as cosmological tracers up to $z \sim 5$ with the cosmic chronometer approach (Moresco, 2024).

Chapter 5

Too old, too early?

5.1 A heuristic model

To interpret the results obtained in the previous chapter, we developed a few simple, heuristic models to explore and quantify the potential degeneracies between parameters and SFHs found in the analysis of galaxies presented in Sect. 4.4, 4.3. The goal of this test is to construct theoretical models combining a fraction of old and young stellar populations, to investigate whether such composite spectra can mimic that of a single intermediate-age population. This analysis aims to determine whether the simultaneous presence of older and younger stars is distinguishable from a purely intermediate population, and in what proportion. To do so, we started from a set of reference models, based on SSPs. In particular, we used galaxy 7549 as a reference case, generating its spectrum at z=0 using a simple burst SFH.

A dictionary of instructions is defined to construct the spectrum using `Bagpipes` (Carnall et al., 2018). The initial "original" spectrum depends on the choice of input parameters, which were set to match the best-fit values obtained for galaxy 7549. The age was fixed to 2 Gyr, and the other parameters—such as stellar mass formed, metallicity, velocity dispersion, and dust attenuation were likewise fixed to their respective best-fit values for that galaxy. This setup provides a reference SSP model from which to explore combinations with older and younger stellar components. To further investigate the degeneracy, the same procedure is repeated for different initial ages, decreasing from 2 Gyr down to 0.5 Gyr. The aim is to investigate how different combinations of young and old stellar populations influence the resulting spectrum.

The reference spectrum is then compared with a combined spectrum generated as follows:

$$f_{\lambda,combined} = 0.5 \cdot f_{\lambda}(age - \Delta t_{young}) + 0.5 \cdot f_{\lambda}(age + \Delta t_{old}), \tag{5.1}$$

where Δt_{old} is considered being 50% older than the reference age (i.e., 1 Gyr for age = 2 Gyr) and Δt_{young} is varied between values ranging from 0 to Δt_{old}, sampling at 10 points. Therefore, this combined spectrum corresponds to the sum of two populations, each one weighted equally. This approach allows us to test how young a stellar population needs to be in order to compensate for the presence of an older one, and still produce a spectrum that is degenerate with the reference case, if such a configuration is possible.

This toy model is built in the simplest form, where both the old and young populations contribute equally. Although this assumption is restrictive, it does not limit the interpretation of the results. If the degeneracy could be explained in this simplest case, it would also hold when parameters such as the fraction of young and old stars are allowed to vary, as long as the sum of these fractions equals 1. Another assumption considered is that parameters such as metallicity and dust attenuation are kept fixed in the combined spectra. This choice is based on the evidence obtained from the analysis, which shows that key parameters like metallicity, dust content, stellar mass, and velocity dispersion remain effectively constant across the explored SFHs. Incorporating these effects would add significant complexity beyond the scope of this initial study where the aim is to isolate the effects of age variations on the combined spectrum.

The resulting spectra are compared by calculating the relative residuals, defined as:

$$\text{residual} = \frac{f_{\lambda,\text{original}} - f_{\lambda,\text{combined}}}{f_{\lambda,\text{original}}}. \tag{5.2}$$

This comparison allows one to quantify how different configurations of stellar populations impact the overall spectrum and whether truly degenerate solutions can arise.

To assess if the residuals found in the analysis could be detectable (and hence different models distinguished), a threshold in signal-to-noise ratio was estimated based on the actual S/N values of the galaxy sample analyzed. The median noise level of the JWST spectra considered in this work is approximately 4% of the signal, i.e., $\frac{S}{N} \sim 25$. To visually represent this threshold in the residual plots, a gray horizontal band spanning ± 0.04 has been plotted.

Therefore, spectral residuals that fall entirely within this gray band indicate that the two spectra, original and combined, are observationally indistinguishable, thus confirming

the presence of a degeneracy. This threshold not only illustrates the noise level but also provides a physically meaningful criterion for defining when two different star formation histories result in effectively identical observable spectra.

To further test the robustness of the observed degeneracy and explore more extreme configurations, additional models are constructed by considering the same set of reference ages (2 Gyr, 1.5 Gyr, 1 Gyr, and 0.5 Gyr), but setting Δt_{old} equal to the age of the reference spectrum, and sampling 20 points in Δt_{young}. This choice increases the temporal separation between the young and old components, creating more extreme cases that better mimic the star formation history of galaxy 7549 and help verify whether the degeneracy still holds under such conditions.

The figures presented in the following sections show the various combined spectra and the corresponding relative residuals for each age configuration. These plots are grouped into two sets: the first four correspond to the case where $\Delta t_{\text{old}} = 0.5 \cdot \text{Age}$, while the remaining ones refer to the more extreme case in which $\Delta t_{\text{old}} = \text{Age}$. These represent different versions of the same analysis, designed to test the effect of increasing the separation between the two stellar components.

5.2 Models with $\Delta t_{old} = 0.5 \cdot$ age

The analysis begins with the toy models constructed by setting $\Delta t_{\text{old}} = 0.5 \cdot \text{Age}$, which serves as a reference scenario to study the effects of spectral degeneracy. These models are presented in order of decreasing age, specifically for initial ages of 2, 1.5, 1, and 0.5 Gyr (see Fig. 5.1, 5.2, 5.3, 5.4). The final figure in this section shows an example of the star formation histories used to generate the toy spectral models presented above. These SFHs consist of two bursts representing young and old stellar populations.

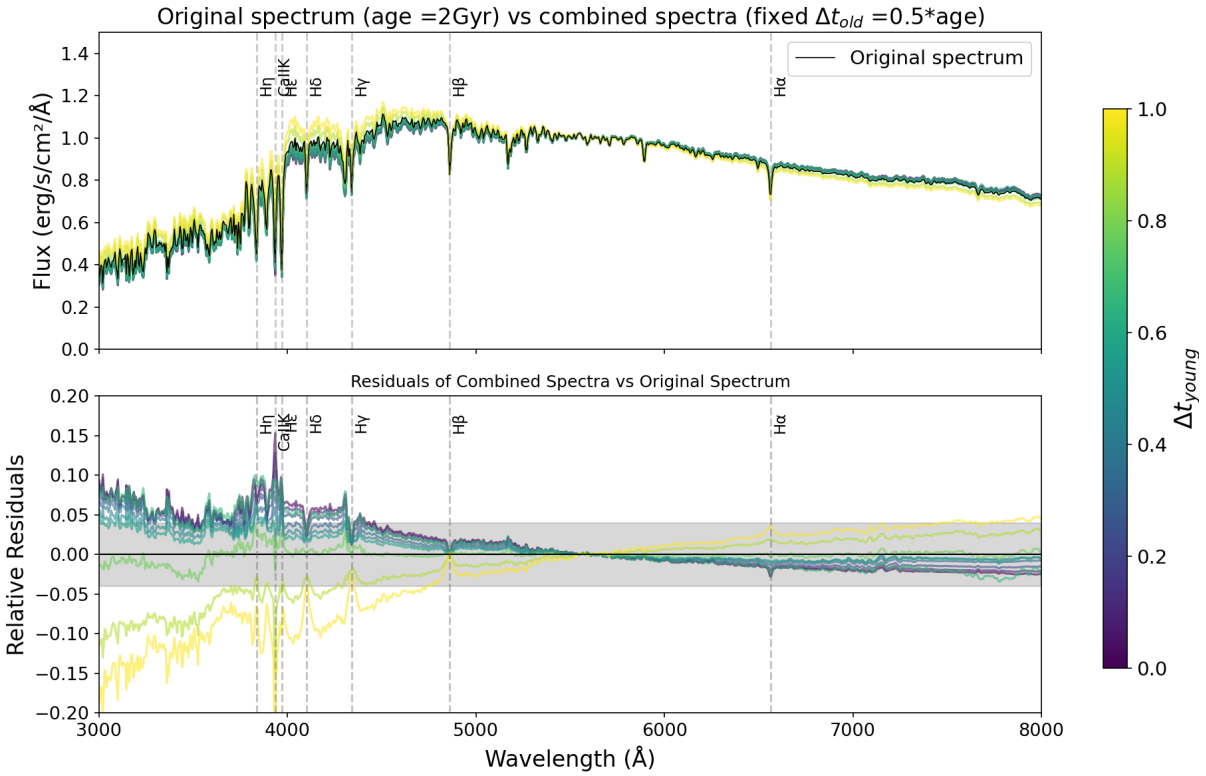

Figure 5.1: Top panel: original spectrum (black) generated with a burst at 2 Gyr, compared to combined spectra (color) built by adding two bursts. Here, $\Delta t_{\rm old}$ is fixed at 1 Gyr, while $\Delta t_{\rm young}$ varies from 0 to 1 Gyr, as shown by the color bar. Main absorption features are marked with dashed vertical lines.
The bottom panel shows relative residuals. The $y = 0$ line marks perfect agreement, and the shaded gray area indicates the ± 0.04 region, corresponding to the typical 1/SNR of JWST spectra. Residuals within this range are considered observationally indistinguishable.

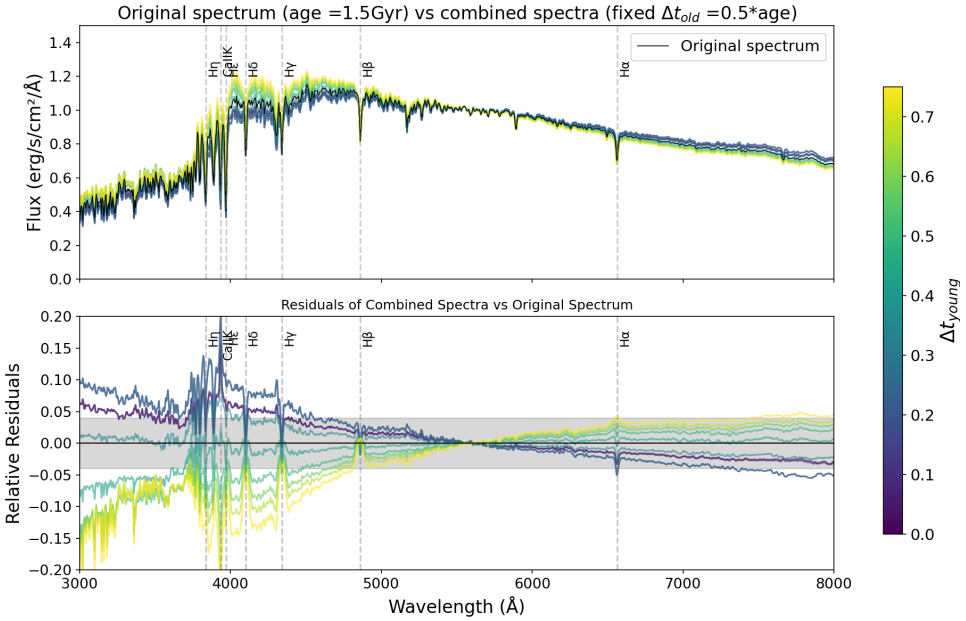

Figure 5.2: Same as Fig. 5.1, but considering a reference age of 1.5 Gyr.

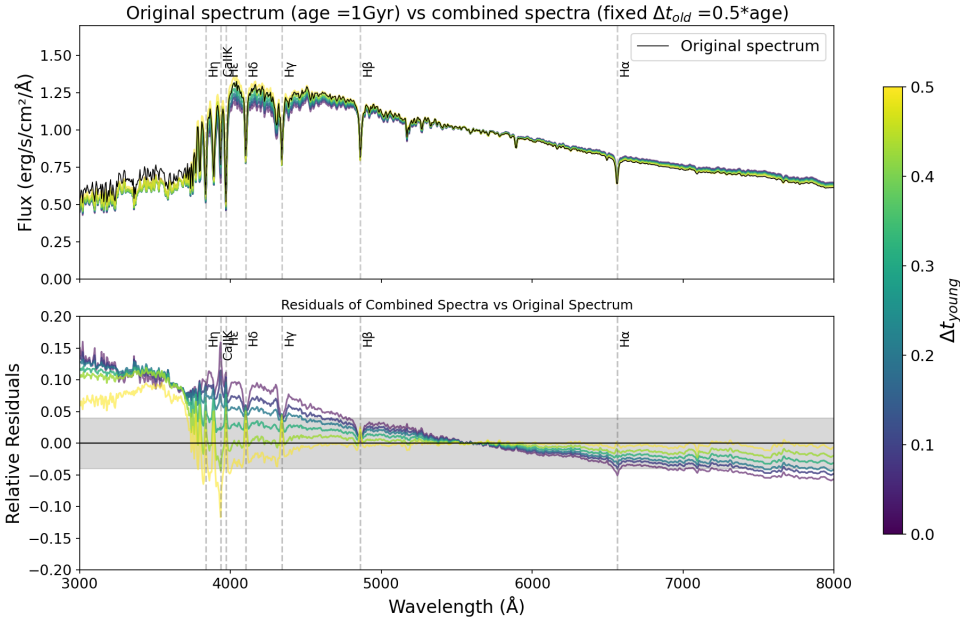

Figure 5.3: Same as Fig. 5.1, but considering a reference age of 1 Gyr.

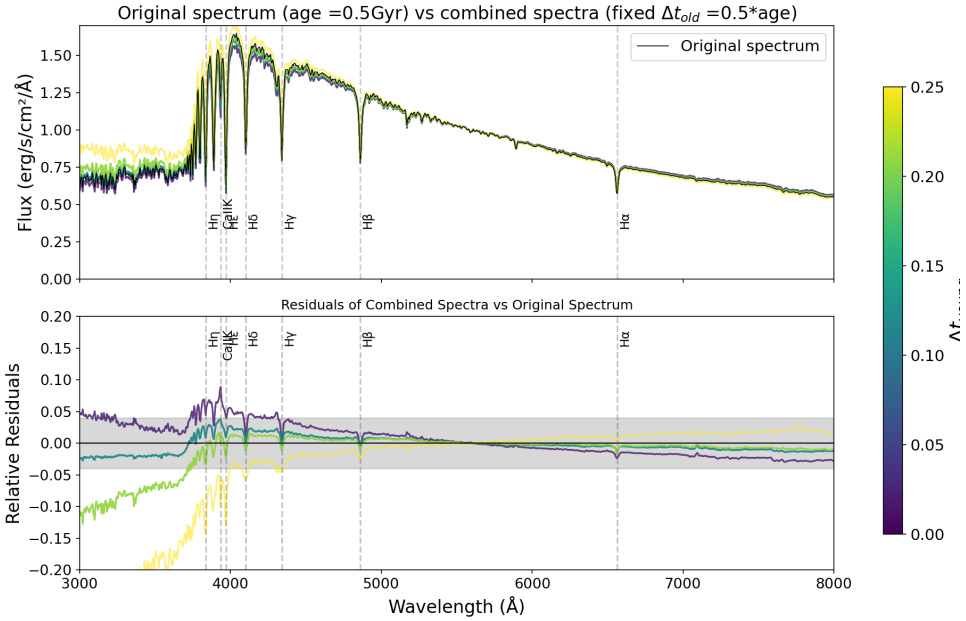

Figure 5.4: Same as Fig. 5.1, but considering a reference age of 0.5 Gyr.

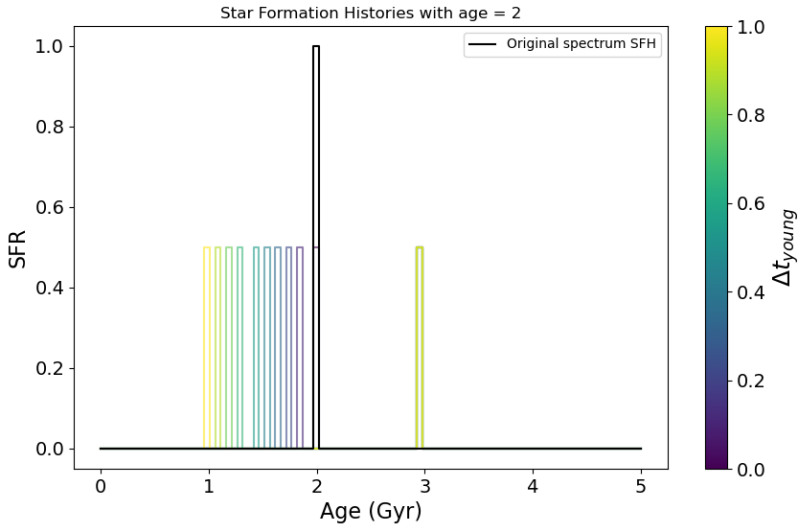

Figure 5.5: The black line shows SFH of the original spectrum, modeled as a single burst at 2 Gyr. Colored lines represent combined SFHs consisting of two bursts: one fixed at 1 Gyr, and one at varying younger ages, $\Delta t_{\rm young}$, as indicated by the color bar.

5.3 Models with Δt_{old} = age

As previously mentioned, this section examines the most extreme case in which $\Delta t_{\rm old}$ = Age. The goal is to test whether the spectral degeneracy observed in more moderate configurations still holds when the two stellar populations are maximally separated in time.

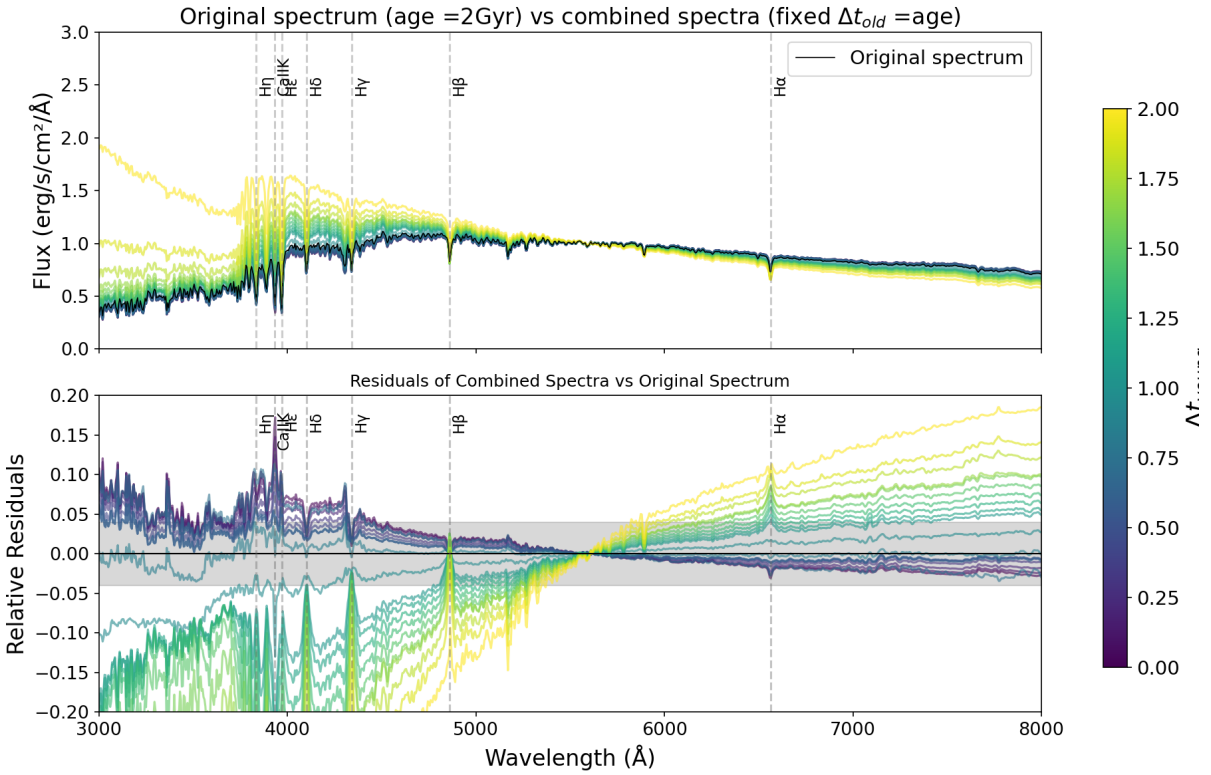

Figure 5.6: Top panel: original spectrum (black) generated with a burst at 2 Gyr, compared to combined spectra (color) built by adding two bursts. Here, $\Delta t_{\rm old}$ is fixed at 2 Gyr, while $\Delta t_{\rm young}$ varies from 0 to 2 Gyr, as shown by the color bar. Main absorption features are marked with dashed vertical lines.
Bottom panel: relative residuals, computed as $(f_{\lambda,\rm original} - f_{\lambda,\rm combined})/f_{\lambda,\rm original}$. The $y = 0$ line marks perfect agreement, and the shaded gray area indicates the ± 0.04 region, corresponding to the typical 1/SNR of JWST spectra. Residuals within this range are considered observationally indistinguishable, revealing spectral degeneracy.

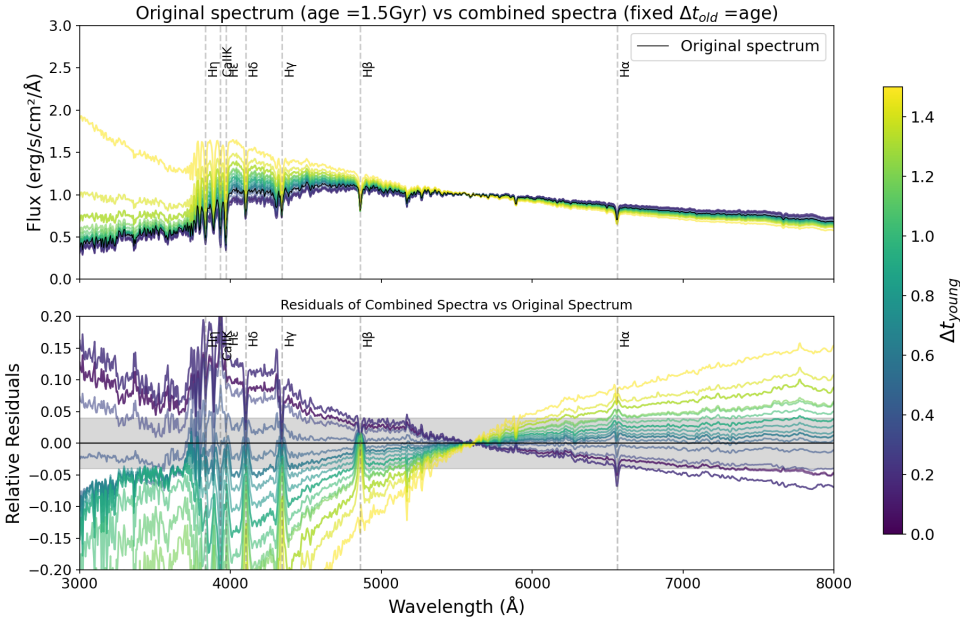

Figure 5.7: Same as Fig. 5.6, but considering a reference age of 1.5 Gyr.

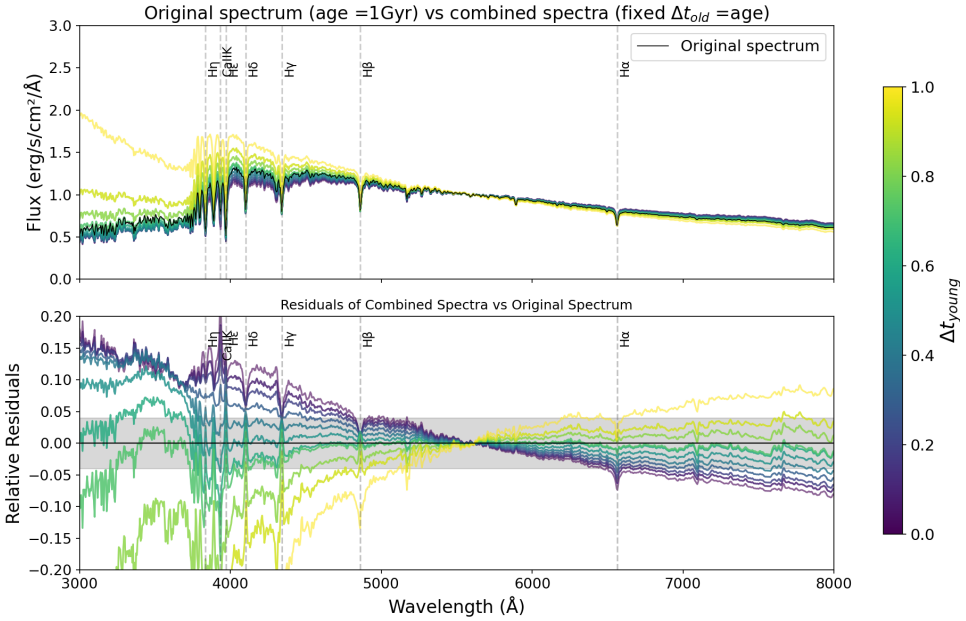

Figure 5.8: Same as Fig. 5.6, but considering a reference age of 1 Gyr

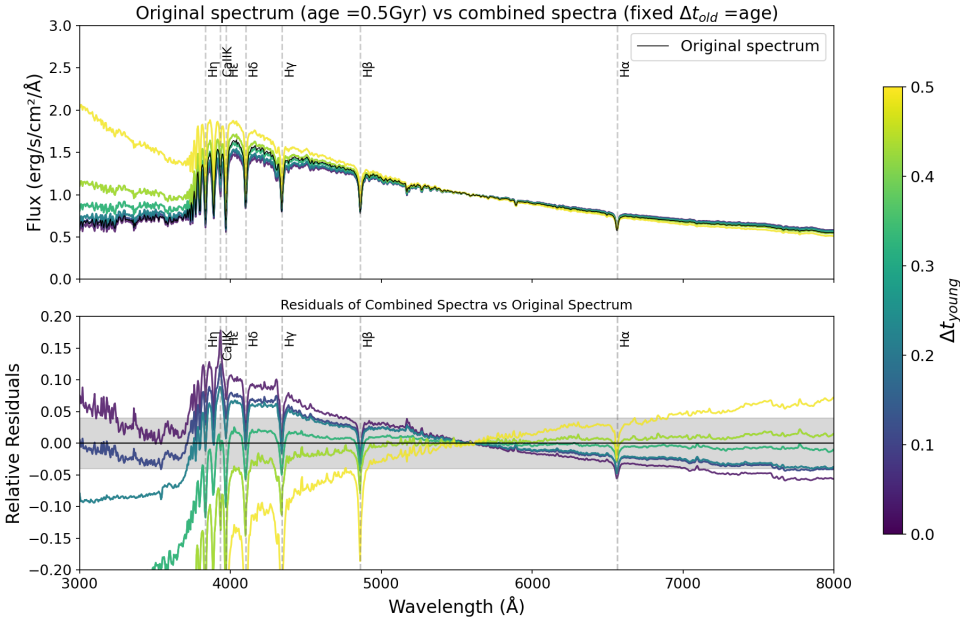

Figure 5.9: Same as Fig. 5.6, but considering a reference age of 0.5 Gyr

5.4 Interpretation of the results

The results from the models presented in the previous sections indicate that the degeneracy between spectra with young and old stellar components is closely linked to the age of the galaxy. This is clearly illustrated in the first test case with an initial age of 2 Gyr, shown in Figure 5.1. In this example, the light green spectrum (that falls within the gray region) corresponds to a combination of a young component with $\Delta t_{\rm young} \sim 0.7$ Gyr and an old component fixed at $\Delta t_{\rm old} = 1$ Gyr. It is worth noting that other spectra also fall within this shaded region, indicating that they are all degenerate. These correspond to values of $\Delta t_{\rm young}$ approximately between 0.5 and 0.8 Gyr. This toy model explores how young a stellar component must be to compensate for the presence of an older one. In this case, we conclude that adding a 1 Gyr old population can be offset by including a younger component just 0.7 Gyr younger, resulting in a spectrum nearly indistinguishable from that of a single age population.

In particular, the older the galaxy, the easier it becomes to hide an older stellar component, as their contribution to the total light becomes increasingly negligible in comparison to that of younger, more luminous stars.

As seen in Figure 5.5, which displays the SFH, this combination corresponds to a scenario in which two distinct bursts — one younger and one older — contribute to the overall light. The degeneracy between the spectra is clearly illustrated by the residuals, shown in the second panel of Figure 5.1. In particular, the flat residuals across both continuum and spectral features (e.g., absorption lines) show that the combined model closely reproduces the original spectrum at all scales.

To further test the limits of this degeneracy, we analyzed an extreme scenario in which the old stellar component formed at the very beginning of the galaxy's history, i.e., $\Delta t_{\rm old} = \text{Age}$. Despite the maximum separation in age between the two populations, some of the combined spectra still fall within the observational uncertainty level, reinforcing the conclusion that such degeneracies persist even under extreme conditions. In particular, as shown in Figure 5.6 the petroleum-colored line—corresponding to a young component added with $\Delta t_{\rm young} \sim 1\,\text{Gyr}$ and $\Delta t_{\rm old} = 2\,\text{Gyr}$—is indistinguishable from the original spectrum.

When the galaxy is younger (e.g., 1.5 Gyr or less), as shown starting from the Figure 5.2, the young component must be extremely young to balance the contribution of the older population and reproduce the original spectrum. However, in these cases, the required young component becomes too young, and discrepancies arise — particularly in the absorption lines (such as Ca H and Ca K), which cannot be masked effectively. Differences also emerge in the continuum. This limits the degeneracy in younger systems, and the reconstruction of the star formation history becomes more constrained at younger ages. On the other hand, this degeneracy becomes more prominent for older systems, where the light from younger stars dominates and can effectively mask the presence of older populations, thus complicating the interpretation of galaxy formation timescales.

It is important to note that in cases where the spectra are nearly indistinguishable, the luminosity-weighted average age of the stellar populations remains close to that of the original model. For example, in the case of a galaxy with an age of 2 Gyr and $\Delta t_{\rm old} = 0.5\text{Age} = 1\,\text{Gyr}$ as shown in Figure 5.1, a combination of a younger component at 1.3 Gyr and an older one at 3 Gyr results in an average age of 2.15 Gyr. This value is very close to the original input age of 2 Gyr. Similarly, in the most extreme scenario — where $\Delta t_{\rm old} = \text{Age} = 2\,\text{Gyr}$ (Figure 5.6)— the younger and older components are at 1 Gyr and 4 Gyr, respectively, yielding an age of 2.5 Gyr. This proximity between the combined and the original ages suggests that, although spectral fitting may not uniquely constrain the full star formation history, the derived average age remains a

robust indicator of the global stellar population age.

These results, when interpreted alongside the cosmology-free fits, reveal two important trends in the high-redshift sample:

1. In galaxies whose stellar populations are relatively young, the inferred age remains stable across different SFH parameterizations—both parametric and nonparametric—and regardless of whether cosmological priors are applied. This stability reflects the fact that, below a certain age threshold (less than 2 Gyr), the addition of an older component would require the simultaneous presence of a very young population to reproduce the observed spectrum. However, such young stars would imprint strong absorption features or induce a continuum slope incompatible with the data, making degenerate solutions unviable.

2. In contrast, for older ages, the removal of cosmological priors leads to an apparent increase in both the maximum age of the population and SFH duration, with the nonparametric SFH often suggesting significant stellar mass formation at very early times. However, the model analysis shows that such scenarios are subject to strong degeneracies: a spectrum attributed to an extended SFH starting very early can be nearly indistinguishable from that of a galaxy formed later, with a younger and more luminous stellar population masking the older component. This implies that, in these cases, the inferred early onset of star formation are less robust. Nevertheless, also in this case it is interesting to notice that the average age of the population is fairly stable, suggesting that while it is difficult for this populations to identify the onset of star formation, their average age can still be retrieved relatively consistently, shedding a positive light in the use of galaxies age as cosmological tracers (Moresco, 2024)

Chapter 6

Conclusions

Understanding how galaxies form and evolve over cosmic time remains one of the fundamental questions in modern astrophysics. The current ΛCDM model provides a remarkably successful framework for describing the expansion history of the Universe and the formation of large-scale structures. Recent advances made possible by the JWST have revolutionized our observational capabilities, providing unprecedented sensitivity and resolution. These high-quality observations enable detailed studies of the earliest galaxies in the Universe, including populations of massive, quiescent galaxies at unexpectedly high redshifts. However, such findings pose new challenges for our theoretical understanding and for the consistency of the ΛCDM framework with the observed galaxy population, as the presence of such mature galaxies at early cosmic times appears difficult to reconcile with the predicted timescales for galaxy formation.

In light of these tensions, this thesis focuses on the analysis of a sample of quiescent galaxies observed with the JWST, deriving their physical properties — such as stellar mass, age, metallicity, and dust content — with a full-spectral fitting approach using the `Bagpipes` code, with particular emphasis on their star formation histories and their compatibility with the ΛCDM cosmological model. The selected galaxies span a redshift range of approximately $z \sim 3$ to $z \sim 5$, with one additional source at $z \sim 2.63$ from the Blue Jay survey.

The analysis begins with the identification of a preselected sample of old and passive galaxies, for which high-quality spectroscopic data were retrieved from the MAST archive. These spectra provide the spectral resolution and signal-to-noise ratios required

for precise analysis. Complementary deep photometric observations were acquired across a broad set of filters, including both Hubble Space Telescope bands and JWST/NIRCam bands, providing broad wavelength coverage to support robust modeling.

Building upon this dataset, the next step involved applying a full-spectral fitting technique to the galaxies, employing multiple parameterizations of the SFH to explore the full range of plausible evolutionary scenarios. A key methodological choice in this analysis was the removal of the cosmological prior on stellar ages. This step was crucial to avoid artificially restricting the formation epochs of galaxies and to investigate the extent of degeneracies that might affect the determination of the onset of star formation, particularly at older ages close to 3 billion years, where the observational constraints tend to weaken.

This flexible approach revealed a robust and consistent agreement across different SFH models for the younger stellar populations (ages around 1.5 billion years), suggesting that their properties are well constrained despite the varying assumptions in the models. However, degeneracies remained for older ages. To better understand and quantify these effects, simple theoretical models were constructed by combining two distinct stellar populations: one old and one young. These models served as a controlled framework to test how different combinations can produce nearly identical spectra, thus highlighting the intrinsic limitations in uniquely recovering the full evolutionary history of a galaxy from its present-day light.

Finally, to evaluate whether the stellar ages inferred from the star formation histories (as detailed in Appendix A) are consistent with the ΛCDM framework, the mass-weighted ages of the galaxies were plotted as a function of redshift and compared to the cosmic age of the Universe predicted by the standard model. This comparison provides a direct and quantitative test of the compatibility between observed galaxy properties and the fundamental timeline of structure formation in ΛCDM cosmology.

In Figure 6.1, each point represents an individual galaxy. The error bars correspond to the 10th and 90th percentiles of the cumulative mass-weighted age distribution derived from the SFH, computed in terms of cosmic time. The central value (50th percentile) indicates the lookback time at which the galaxy formed half of its stellar mass.

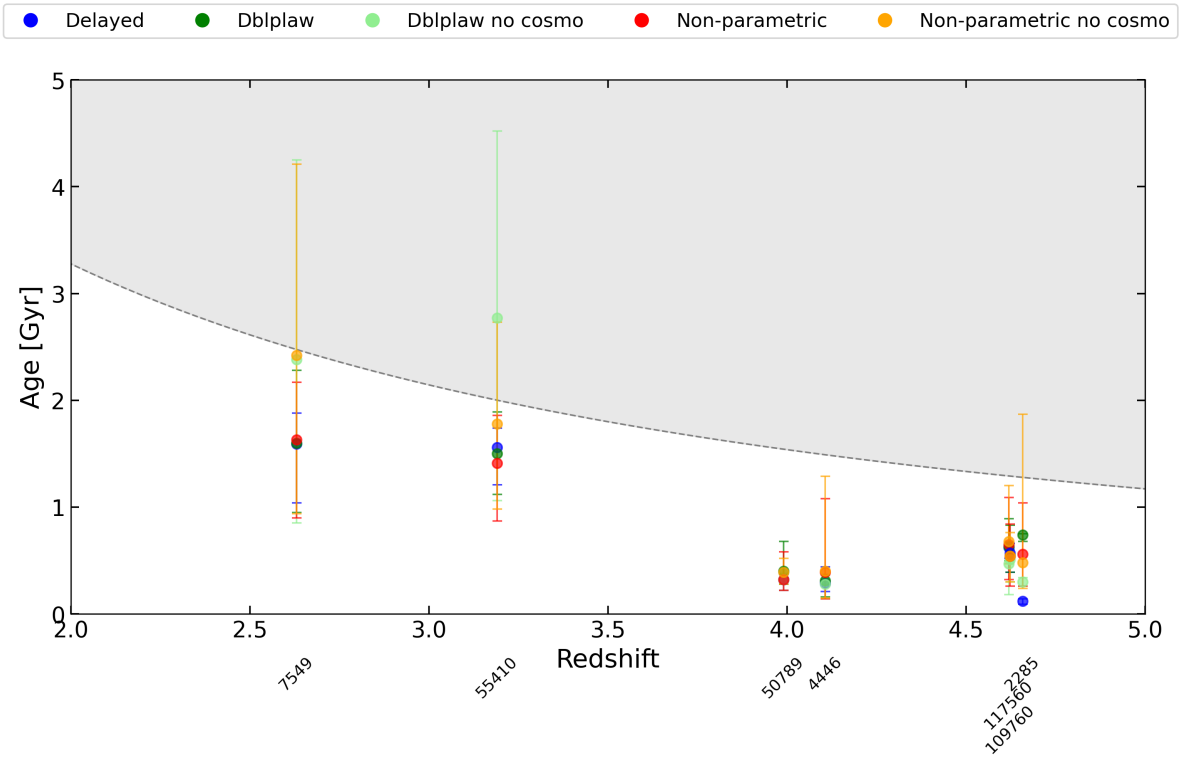

Figure 6.1: Summary plot showing the mass-weighted ages of all galaxies in the sample as a function of redshift, for all SFH models considered in this work. The dashed line shows the age of the Universe as a function of redshift in a standard ΛCDM cosmology, and the shaded region marks the unphysical regime where the inferred stellar ages exceed the cosmic age limit.

Galaxies at lower redshifts (and larger ages, e.g., IDs 7549 and 55410) show mass-weighted ages that approach or even exceed the cosmic age when constraints from cosmology are relaxed. This is particularly evident in the nonparametric (orange) and double power-law (light green) models without cosmological priors, indicating a potential tension with ΛCDM.

In contrast, galaxies at higher redshifts (and correspondingly younger ages, $z > 4$) exhibit remarkable consistency in age estimates despite significant variations in the parameterizations used. Even when using flexible SFH models without cosmological constraints, the inferred ages remain well below the age of the Universe at the corresponding redshifts and are robustly consistent with each other. This stability in the age estimates is further supported by the results of the "toy models". At such young inferred ages, it appears

challenging to mimic the observed spectral features–such as strong absorption lines and continuum shape–by simply balancing the contribution of a young population with an older one. These spectral features act to break the degeneracies that otherwise affect age determinations, enhancing the robustness of the fits.

This is consistent with recent works, such as Tacchella et al. (2022), which show that massive galaxies at $z \gtrsim 4$ typically exhibit recent, rapid star formation episodes, with little evidence for long-duration or very old stellar populations.

For all the galaxies in the sample, even in cases where the SFHs are determined with greater uncertainties due to parameter degeneracies, the median mass-weighted ages remain stable across different models. This stability implies that the evolution of the ages of these galaxies can be robustly estimated, providing a solid basis for applications such as the cosmic chronometers method. Furthermore, focusing on absolute age estimates, it has been demonstrated that as observations move towards higher redshifts and correspondingly younger stellar ages, the degeneracies affecting age and SFH determinations are progressively lifted. This results in a significantly more robust estimation of ages and SFHs in the early Universe. Therefore, while the apparent challenges posed by galaxies at intermediate redshifts ($z \sim 2$–3) to the ΛCDM model must be interpreted with caution due to these modeling ambiguities, the improved reliability of age determinations at higher redshifts ($z > 4$) makes the study of massive, passive galaxies in this regime particularly promising as a stringent test of cosmological models.

These findings offer an encouraging outlook: the so-called "cosmic age tension" appears primarily in intermediate-redshift galaxies ($z \sim 2 - 3$), where parameter degeneracies and uncertainties in SFH modeling are more severe. Moving to higher redshifts—where these degeneracies are less problematic and star formation histories are more sharply constrained—provides a clearer window into early galaxy evolution and cosmology. This motivates continued efforts to study galaxies at the highest accessible redshifts.

Beyond the stellar ages, another dimension of potential tension with ΛCDM arises when considering the stellar masses derived for these galaxies. Many objects in the sample exhibit high stellar masses, on the order of $M_* \sim 10^{11}\, M_\odot$, already assembled at redshifts $z \gtrsim 4$.

According to the stellar-to-halo mass relation (SHMR), such stellar masses would require host dark matter halos of M $\gtrsim 10^{12.5}\, M_\odot$, which are expected to be exceedingly rare at these redshifts in standard ΛCDM cosmology. Moreover, theoretical models predict

a decline in star formation efficiency in massive halos at earlier cosmic times, further complicating the formation of such massive galaxies at $z \gtrsim 4$.

This mass-based tension strengthens the case that certain galaxies may challenge the standard paradigm in terms of the efficiency and timing of their mass assembly. However, stellar mass estimates at high redshift rely on several model-dependent assumptions that become increasingly uncertain in the early Universe. In particular, masses are typically derived from SED fitting, which depends on the choice of initial mass function, the parametrization of the star formation history, dust attenuation laws, and stellar population synthesis models. These assumptions can introduce significant uncertainties. Furthermore, high-redshift galaxies may follow different physical prescriptions than those calibrated at lower redshift, potentially biasing mass estimates. Therefore, these interpretations must be approached with caution, given the systematic uncertainties involved.

The issue remains an open question, and future studies with deeper observations and more accurate modeling will be crucial to determine whether these high masses and seemingly old ages truly represent a tension with the standard cosmological framework.

6.1 Future Prospects

Looking forward, several directions can be taken to build on the results presented in this thesis. First, the current analysis is based on a small, preselected sample of seven galaxies previously studied in the literature, in which some had been identified as potentially exhibiting ΛCDM tension. Expanding the statistical sample, for example by systematically analyzing a larger number of high-redshift quiescent galaxies from upcoming JWST surveys, will be crucial to assess the prevalence and robustness of the cosmic age tension. In particular, surveys such as RUBIES (de Graaff et al., 2025) and DeepDive (Ito et al., 2025) will provide rich datasets that are well suited to this goal.

Second, future JWST observations will provide deeper and higher-resolution spectroscopic data over a broader wavelength range. Combining NIRSpec with MIRI data will allow for improved constraints on stellar populations, dust attenuation, and emission lines, thereby refining stellar age estimates and star formation history reconstructions.

Third, improving the physical assumptions underlying full-spectral fitting is an important avenue. In particular, most current stellar population synthesis models assume solar abundance patterns (e.g., $[\alpha/\mathrm{Fe}]= 0$). However, at high redshifts, this assumption may

not hold, since galaxies are expected to exhibit α-enhanced chemical compositions due to shorter enrichment timescales. New-generation SPS models, such as those developed by Park et al. (2024a), include variable [α/Fe] and individual elemental abundances, and represent a promising tool for more physically accurate modeling of high-redshift galaxies. While these models are not yet widely integrated into fitting codes such as `Bagpipes`, their adoption in future studies will likely provide a better handle on abundance-driven systematics in age determinations.

Finally, the simple theoretical models used in this thesis to explore spectral degeneracies are built under simplifying assumptions, such as equal weighting between stellar populations and limited age configurations. A more realistic approach would involve expanding the parameter space explored, using Monte Carlo techniques to model a wider range of burst scenarios, age separations, and mass fractions. Such efforts would allow for a more systematic quantification of degeneracies and their impact on the derived galaxy parameters.

Overall, the combination of richer datasets, improved theoretical models, and larger samples will provide a clearer picture of galaxy evolution at early cosmic times and will help assess whether the apparent tensions with ΛCDM are real, systematic, or methodological in nature.

Appendix A

Mass-weighted Age Determination from SFHs

In this appendix, the method used to estimate the stellar ages of the galaxies in the sample is described. For each galaxy, five different star formation histories are shown, corresponding to the models described in the main text: delayed exponential, double power law, double power law without cosmological constraints, non-parametric, and nonparametric without cosmological constraints.

Each plot presents the SFH as a function of cosmic time (in Gyr), from the Big Bang up to the age of the Universe. The age of the stellar population is defined as the mass-weighted formation time, computed as the time when the galaxy had formed half of its final stellar mass. This value corresponds to the 50th percentile of the cumulative curve(t50), obtained by integrating the SFH over time. The vertical lines indicate the 10th, 50th and 90th percentiles of the cumulative mass formed.

$M(t)$ is computed by integrating the SFH, $\psi(t)$, using the trapezoidal method on a uniform time grid from 0 to 5 Gyr with 1000 points:

$$M(t) = \int_0^t \psi(t')\, dt',$$

The 10th and 90th percentiles (t_{10} and t_{90}) are used to quantify the age span of the stellar populations: negative error is given by $t_{50} - t_{10}$, and the positive error by $t_{90} - t_{50}$. These values are reported in the tables in the main text for each galaxy.

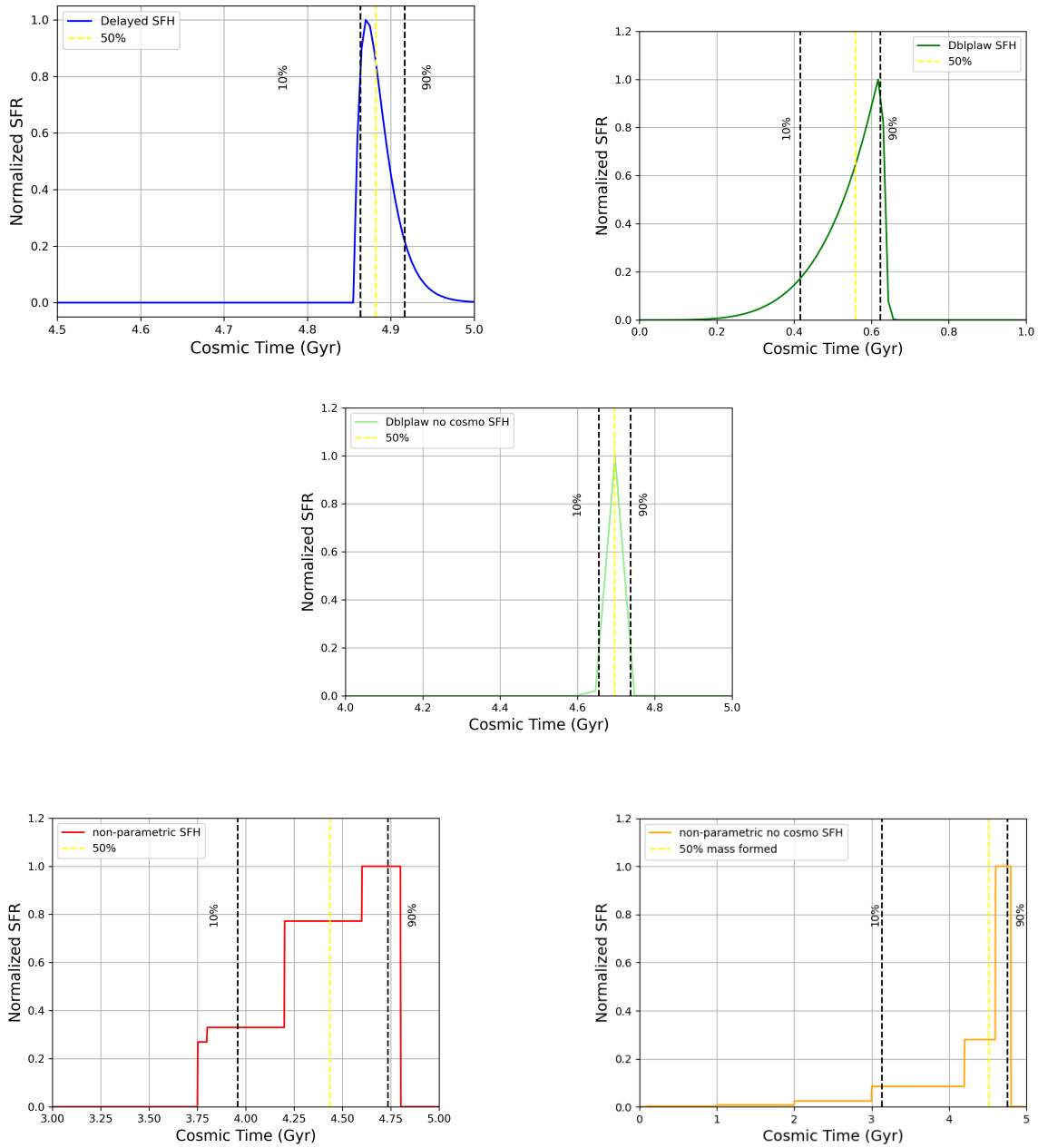

Figure A.1: Galaxy 9209: SFHs corresponding to five different model configurations, each providing an age estimate for the galaxy.

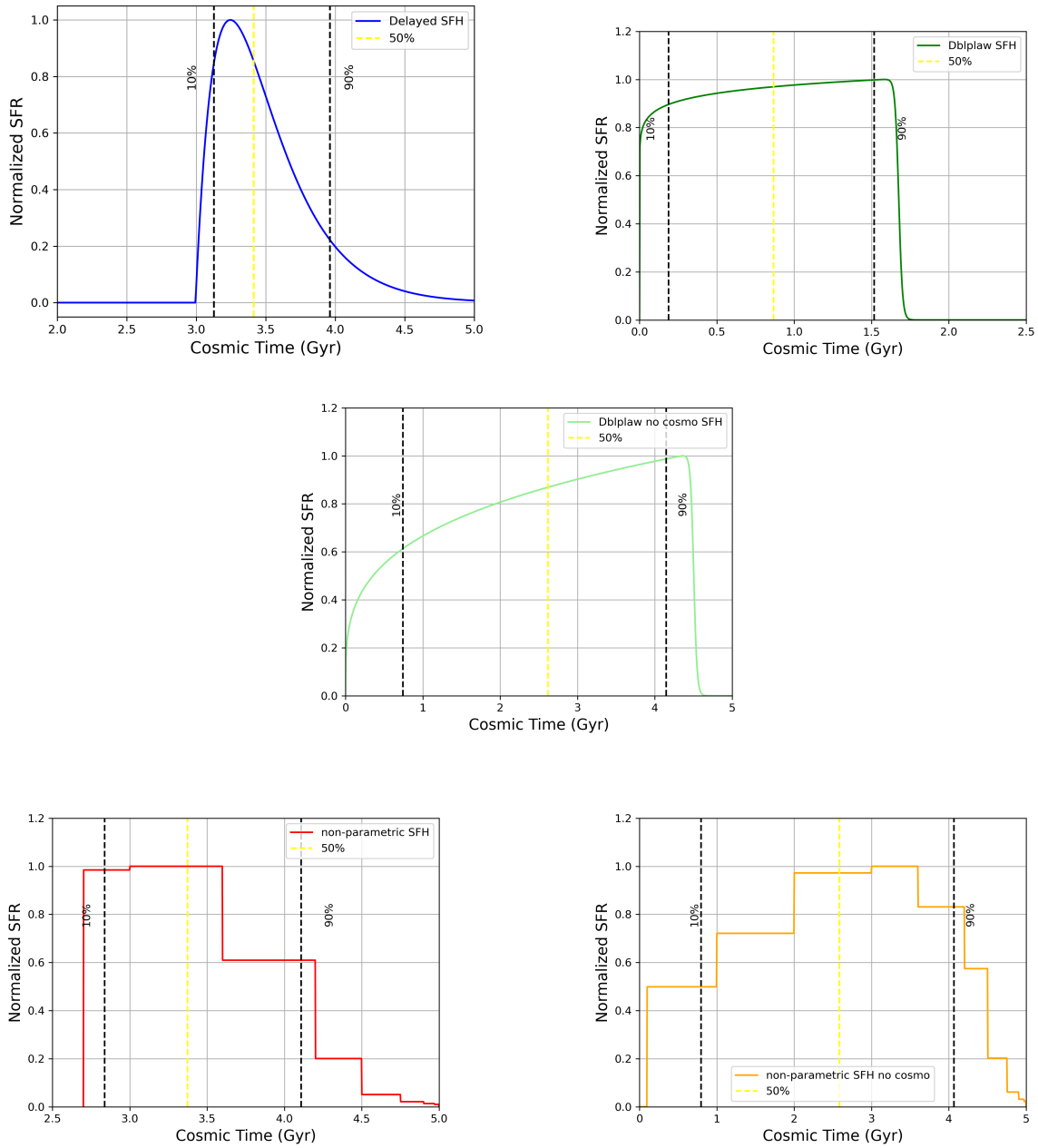

Figure A.2: Galaxy 7549: SFHs corresponding to five different model configurations, each providing an age estimate for the galaxy.

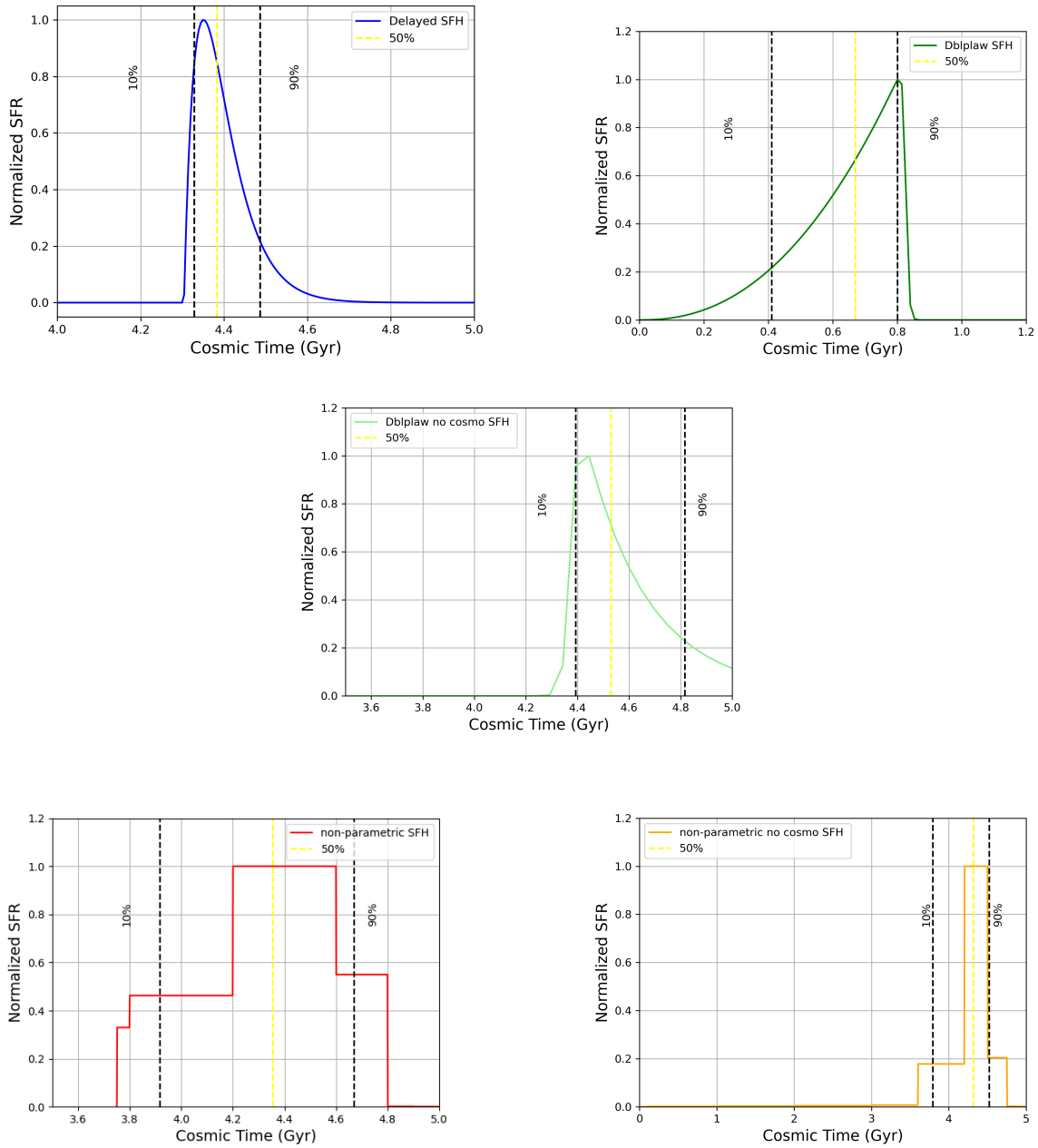

Figure A.3: Galaxy 117560: SFHs corresponding to five different model configurations, each providing an age estimate for the galaxy.

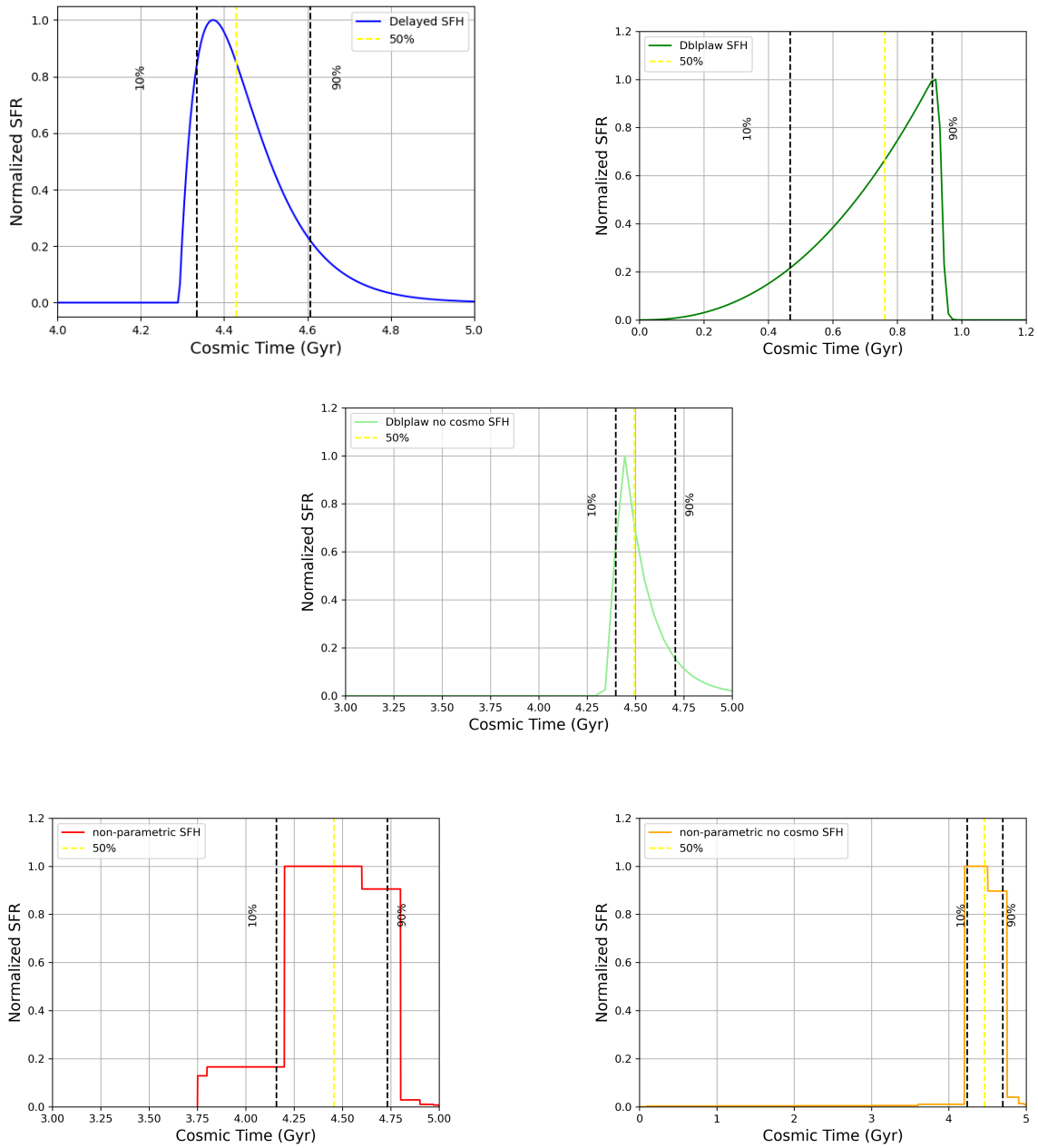

Figure A.4: Galaxy 109760: SFHs corresponding to five different model configurations, each providing an age estimate for the galaxy.

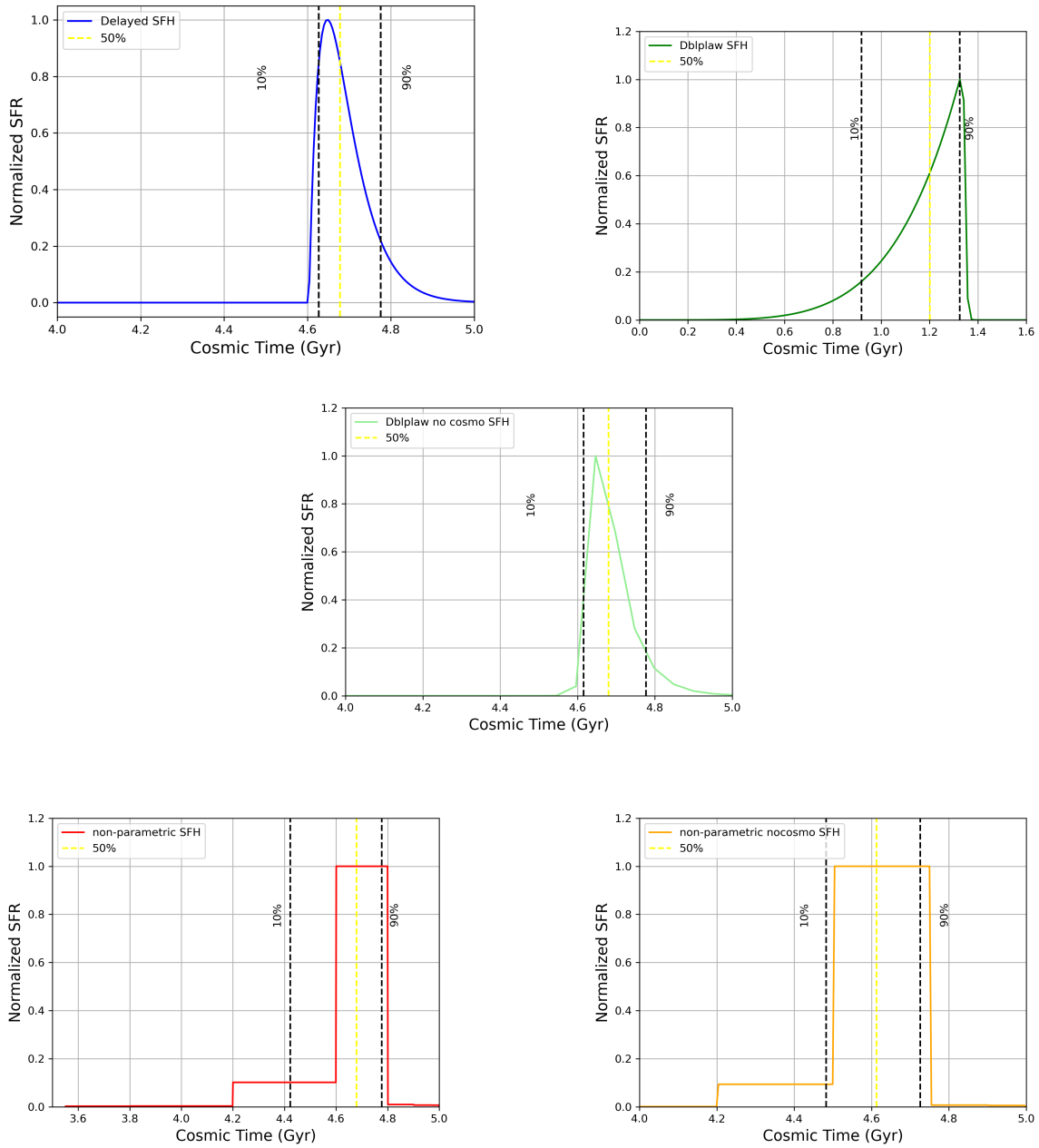

Figure A.5: Galaxy 50789: SFHs corresponding to five different model configurations, each providing an age estimate for the galaxy.

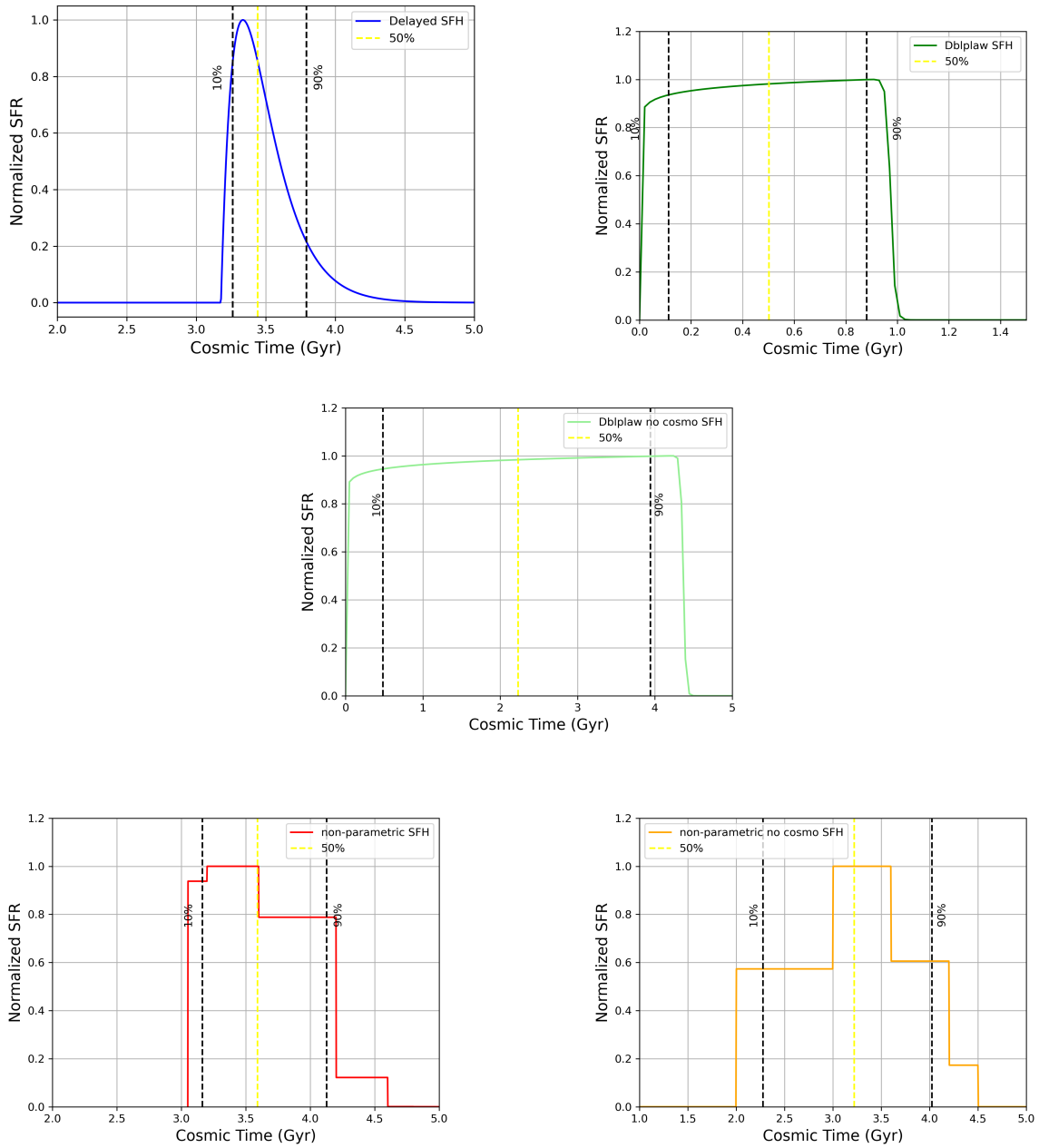

Figure A.6: Galaxy 55410: SFHs corresponding to five different model configurations, each providing an age estimate for the galaxy.

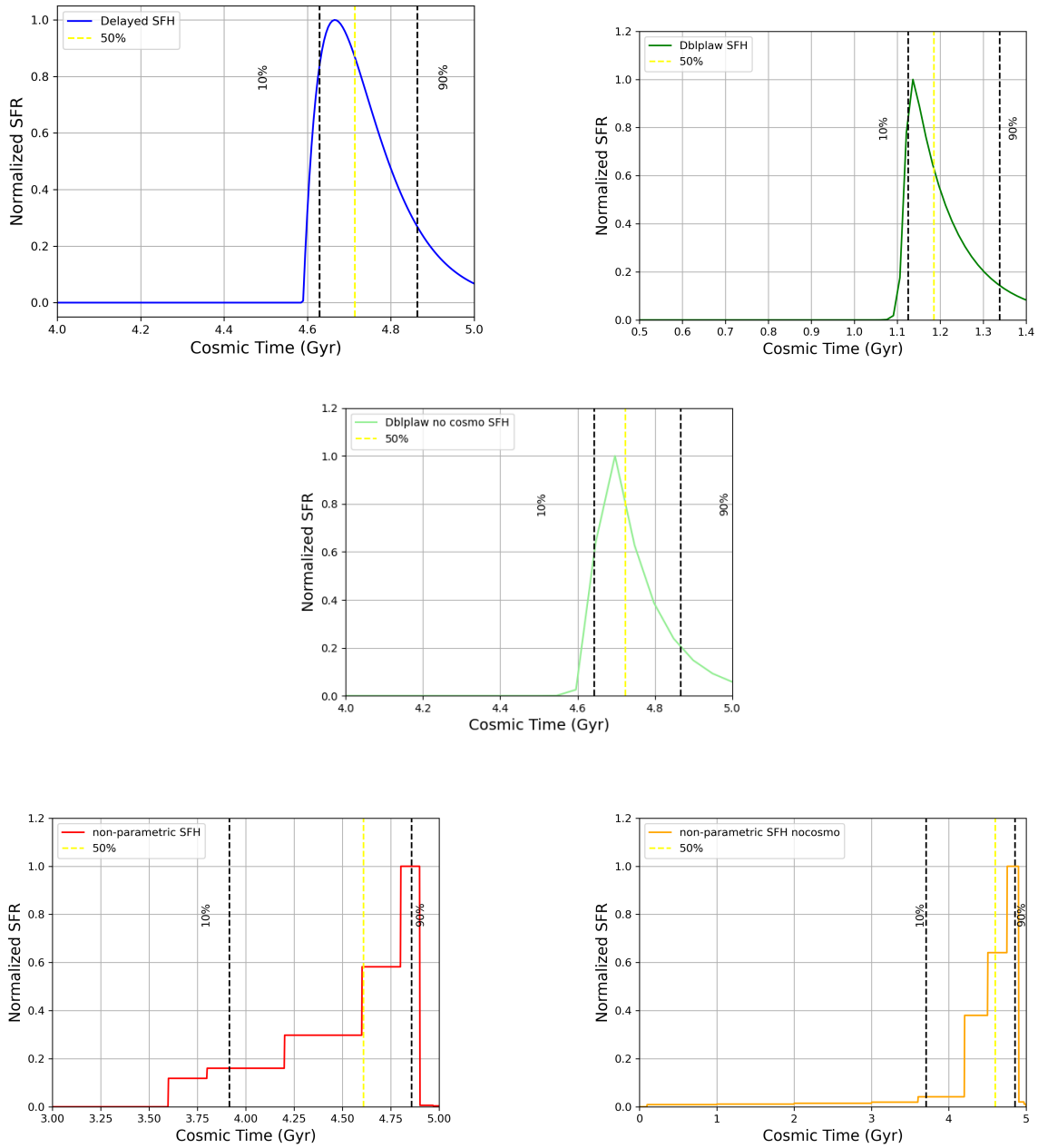

Figure A.7: Galaxy SNH0pe-NS274: SFHs corresponding to five different model configurations, each providing an age estimate for the galaxy.

Appendix B

Lick indices estimation

This appendix provides the full set of plots showing the Lick indices measured for each galaxy in the sample. These indices, derived from the rest-frame optical spectra obtained with JWST/NIRSpec, offer a qualitative insight into the stellar population properties, such as age, metallicity, and chemical abundance ratios, of quiescent galaxies at high redshift.

One representative example has been discussed in detail in the main text to illustrate the measurement procedure and the interpretation of the indices. The remaining galaxies are presented here for completeness, following the same methodology. Each figure shows the observed spectrum and the spectral regions used for the computation of the indices.

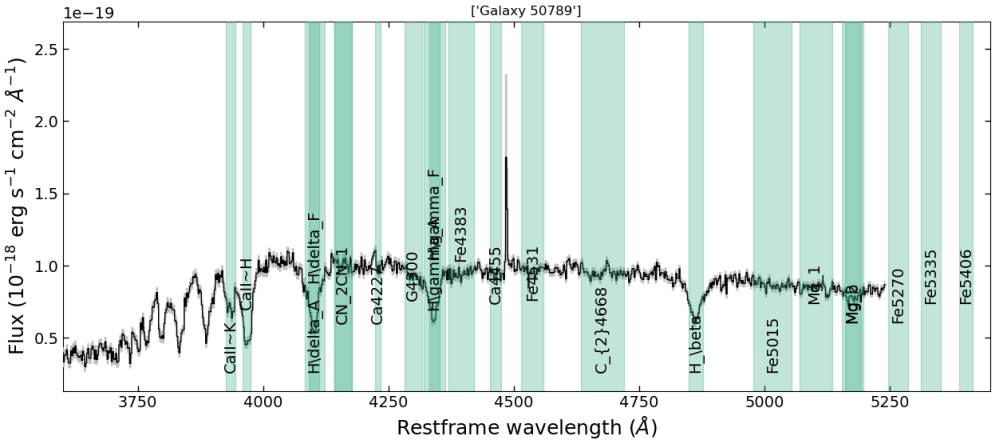

Figure B.2: Lick indices: Galaxy 50789

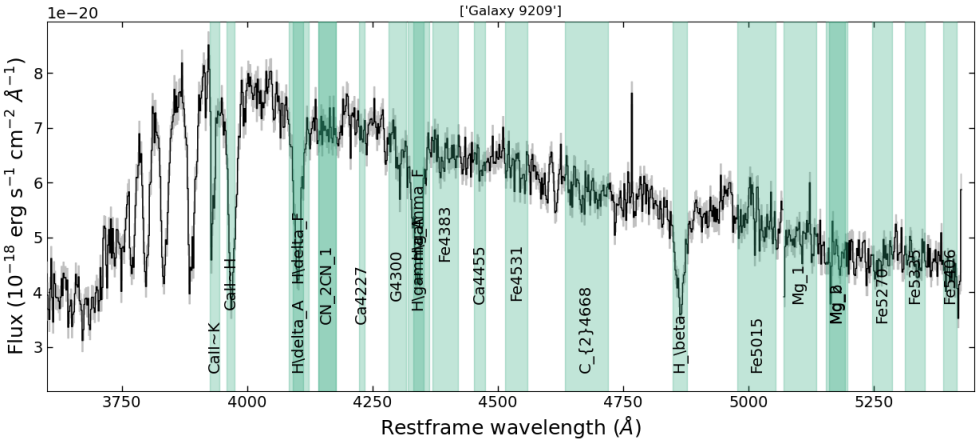

Figure B.1: Lick indices: Galaxy 9209

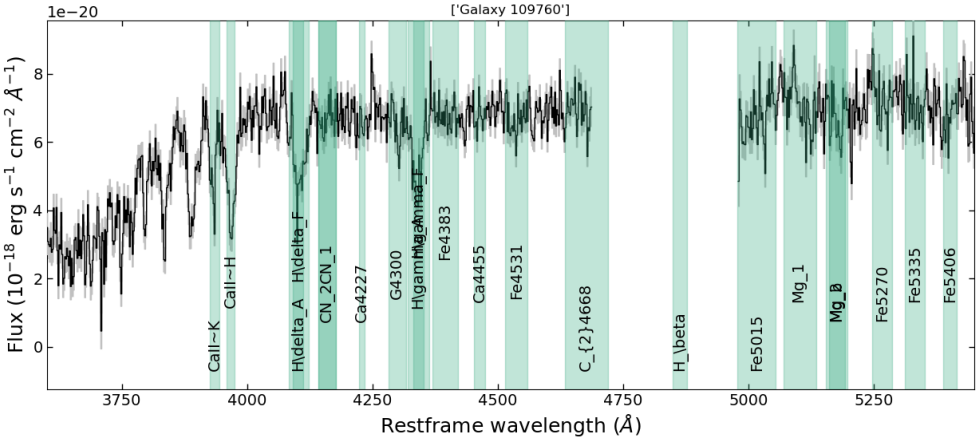

Figure B.3: Lick indices: Galaxy 109760

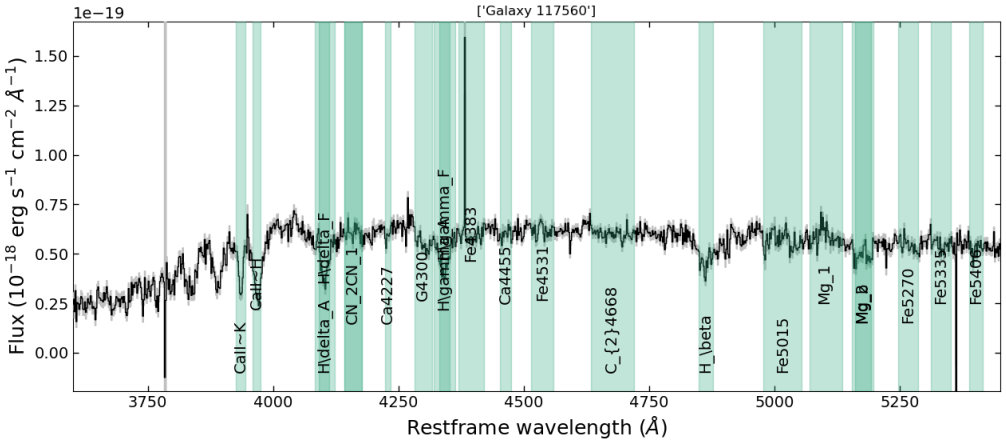

Figure B.4: Lick indices: Galaxy 117560

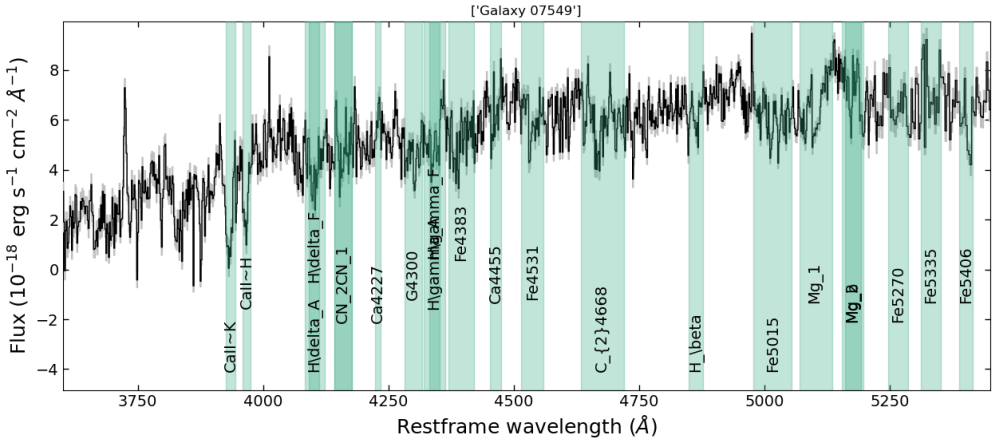

Figure B.5: Lick indices: Galaxy 7549

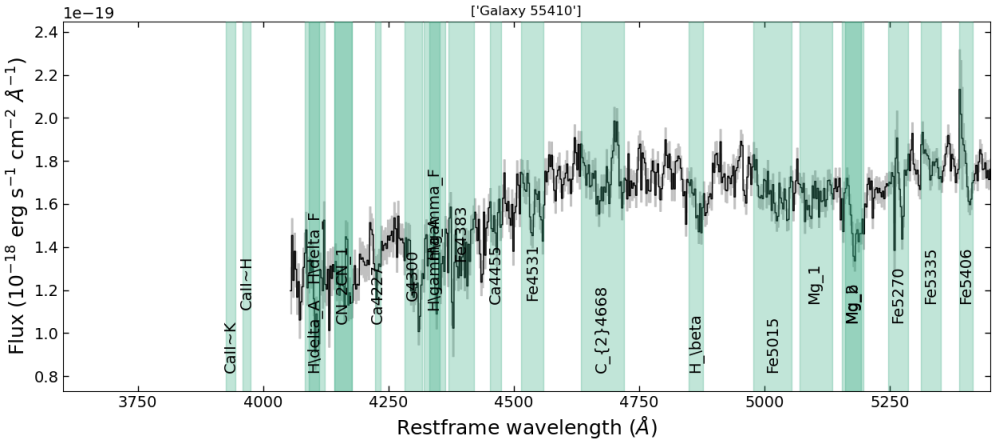

Figure B.6: Lick indices: Galaxy 55410

Appendix C

Results of the Full-Spectral Fitting analysis

This appendix provides the complete set of spectral results for all galaxies included in the analysis.

Each galaxy is presented through a three-panel figure showing: (1) the five model spectra generated using different star formation histories — delayed, double power law, and nonparametric (the latter two also shown with and without a cosmological prior on the age) — along with their corresponding χ^2 values, which quantify the goodness of fit; (2) a comparison between the model and observed spectra, rescaled using the polynomial calibration function derived from the fit; and (3) the residuals, defined as the difference between the observed and model spectra, normalized by the flux uncertainty. These residuals highlight any systematic discrepancies and help assess the quality of the spectral reconstruction.

Galaxy NH0pe-NS274

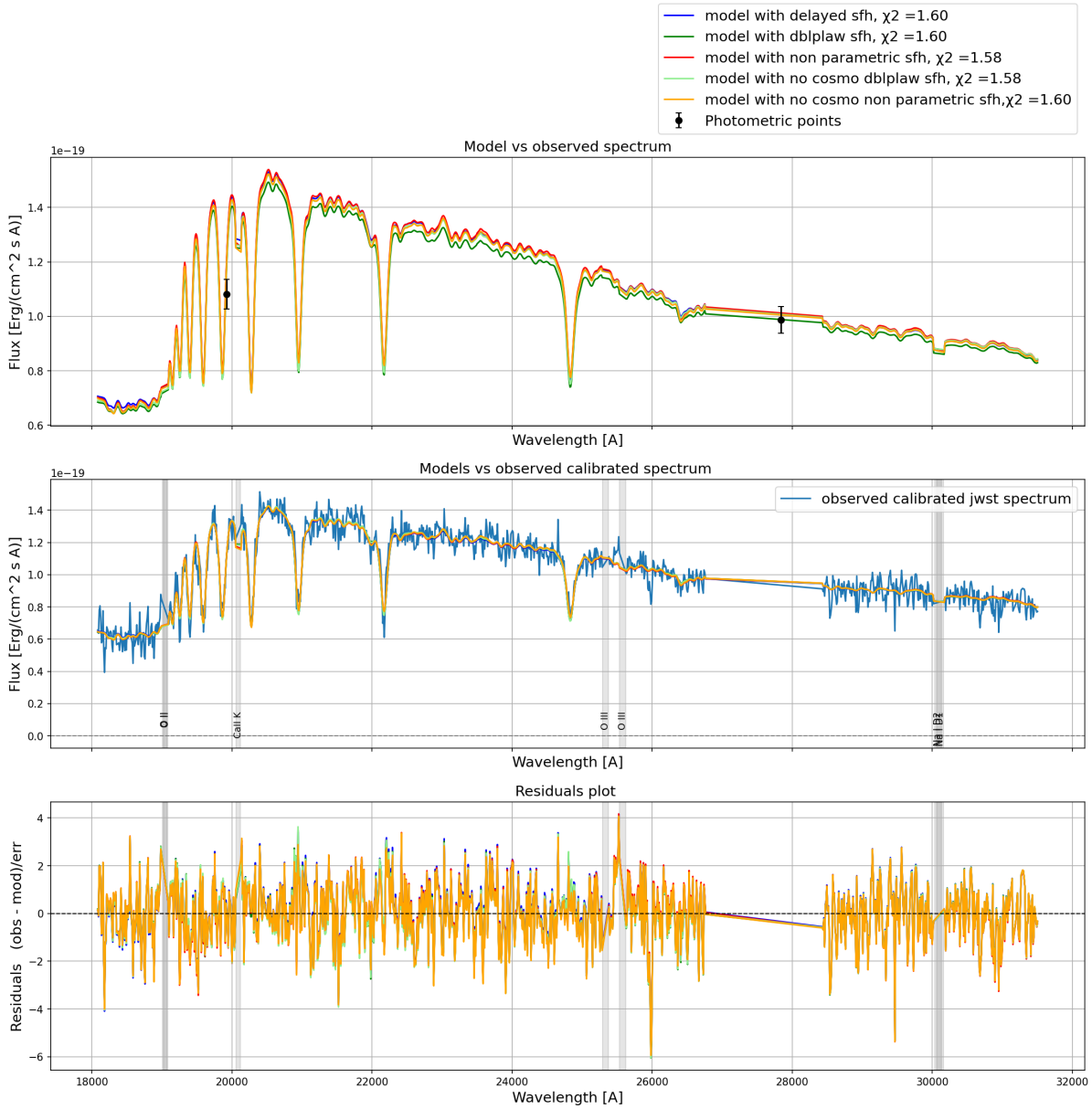

Figure C.1: In the first panel, the comparison between the different models is shown, together with the photometric data points; the second panel displays the comparison between the models and the observed spectrum; and the third panel shows the residuals, computed as the difference between the model and the observed data normalized by the observational uncertainties. The models correspond to different star formation histories fitted with `Bagpipes` .

Galaxy 9209

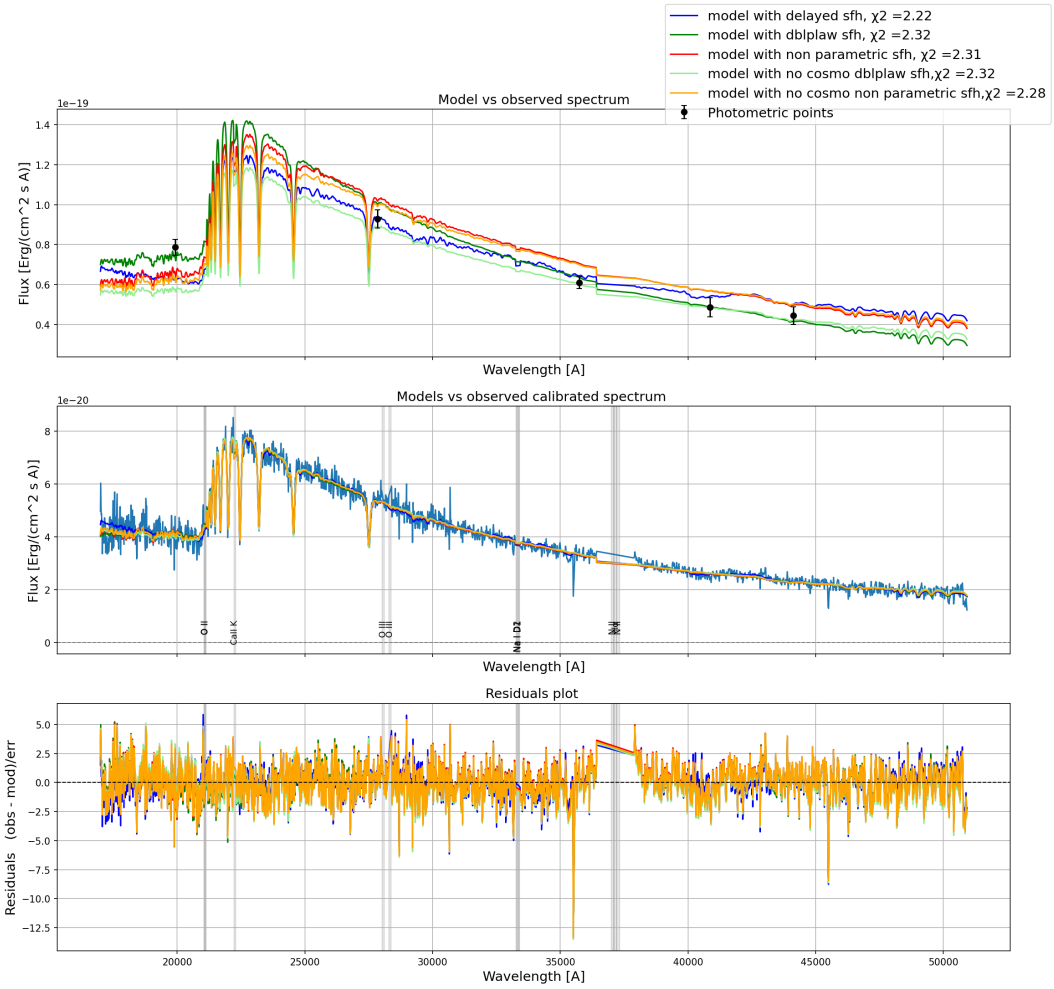

Figure C.2: Same as Fig. C.1.

Galaxy 50789

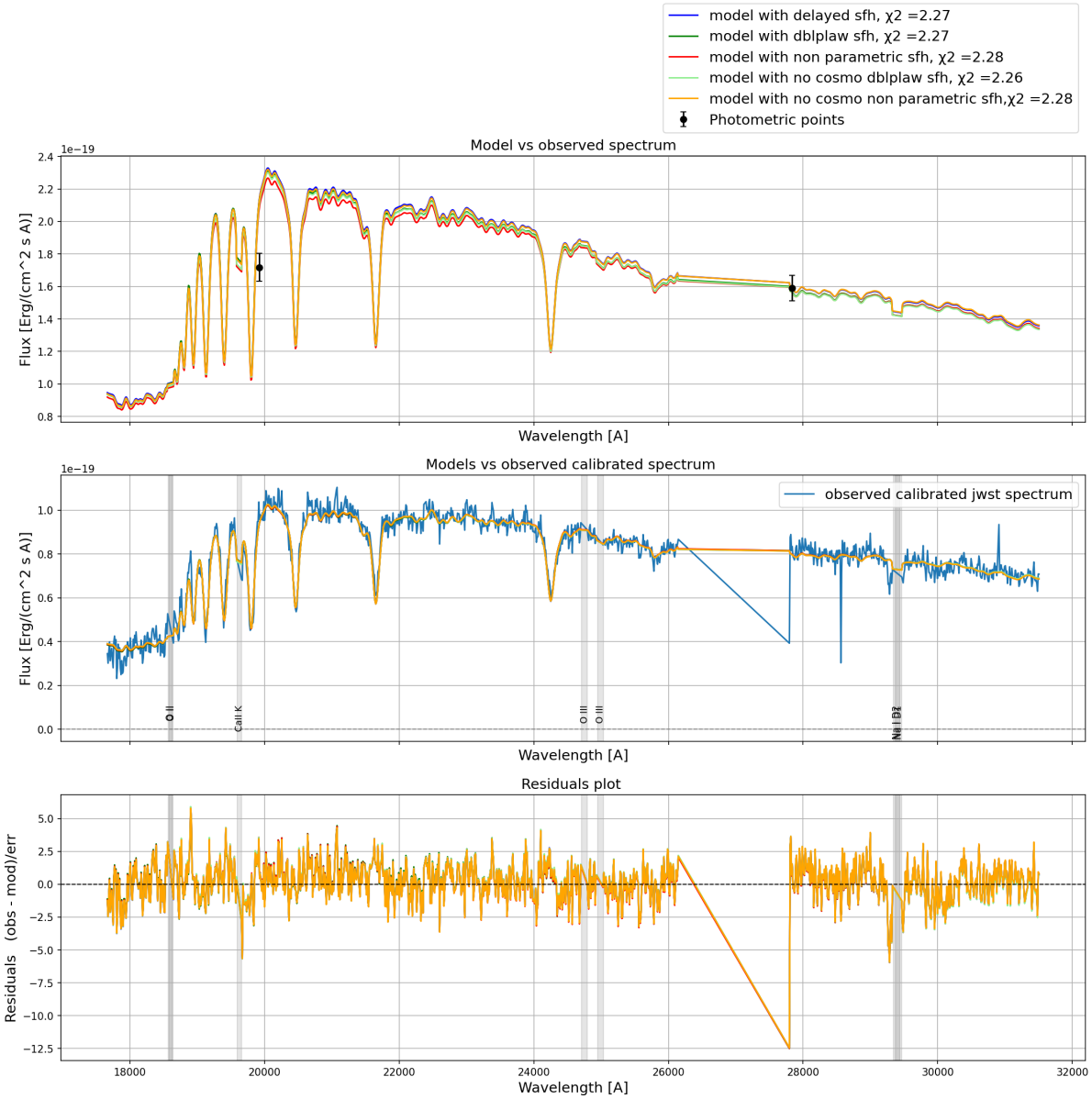

Figure C.3: Same as Fig. C.1.

Galaxy 109760

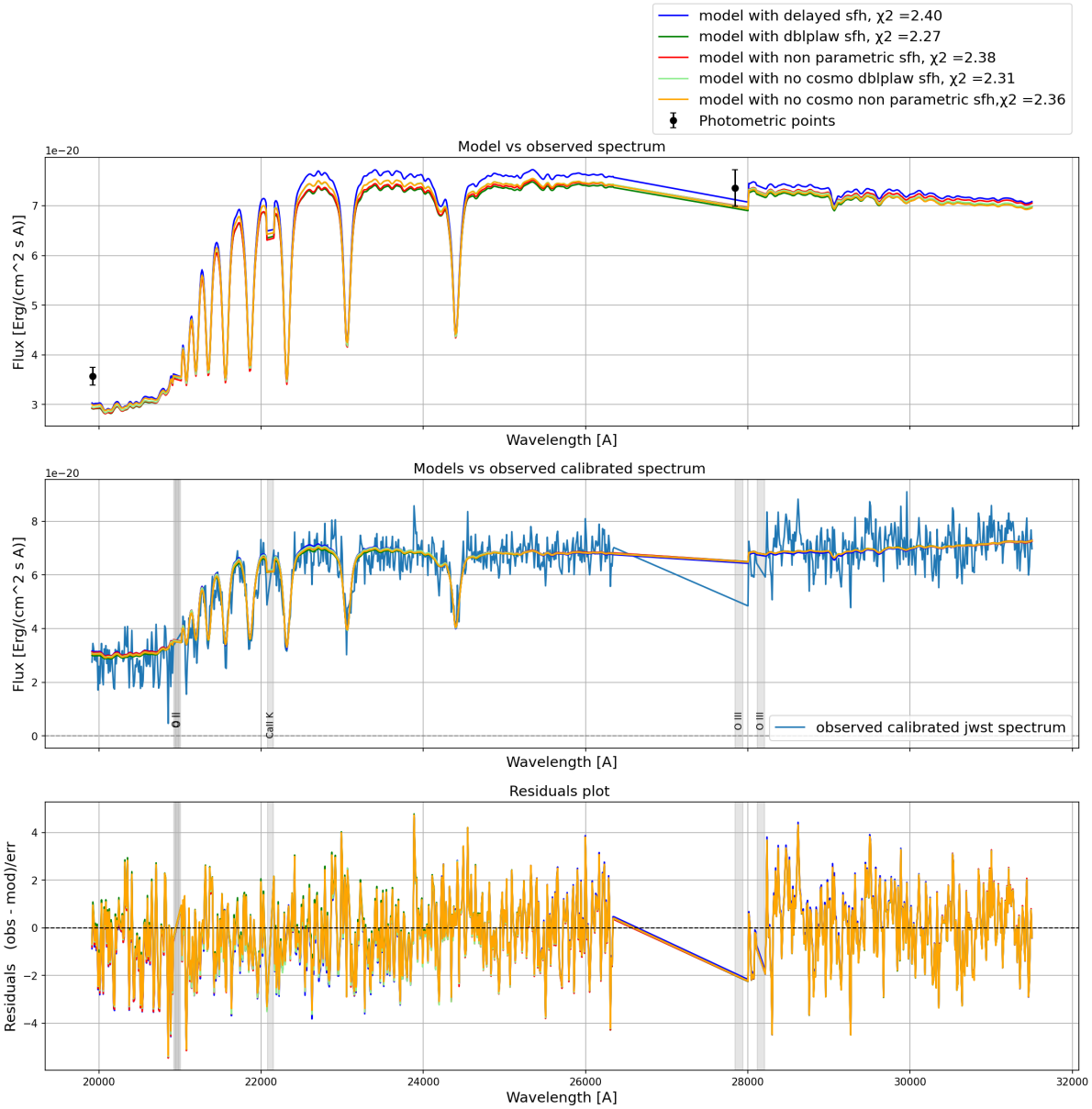

Figure C.4: Same as Fig. C.1.

Galaxy 117560

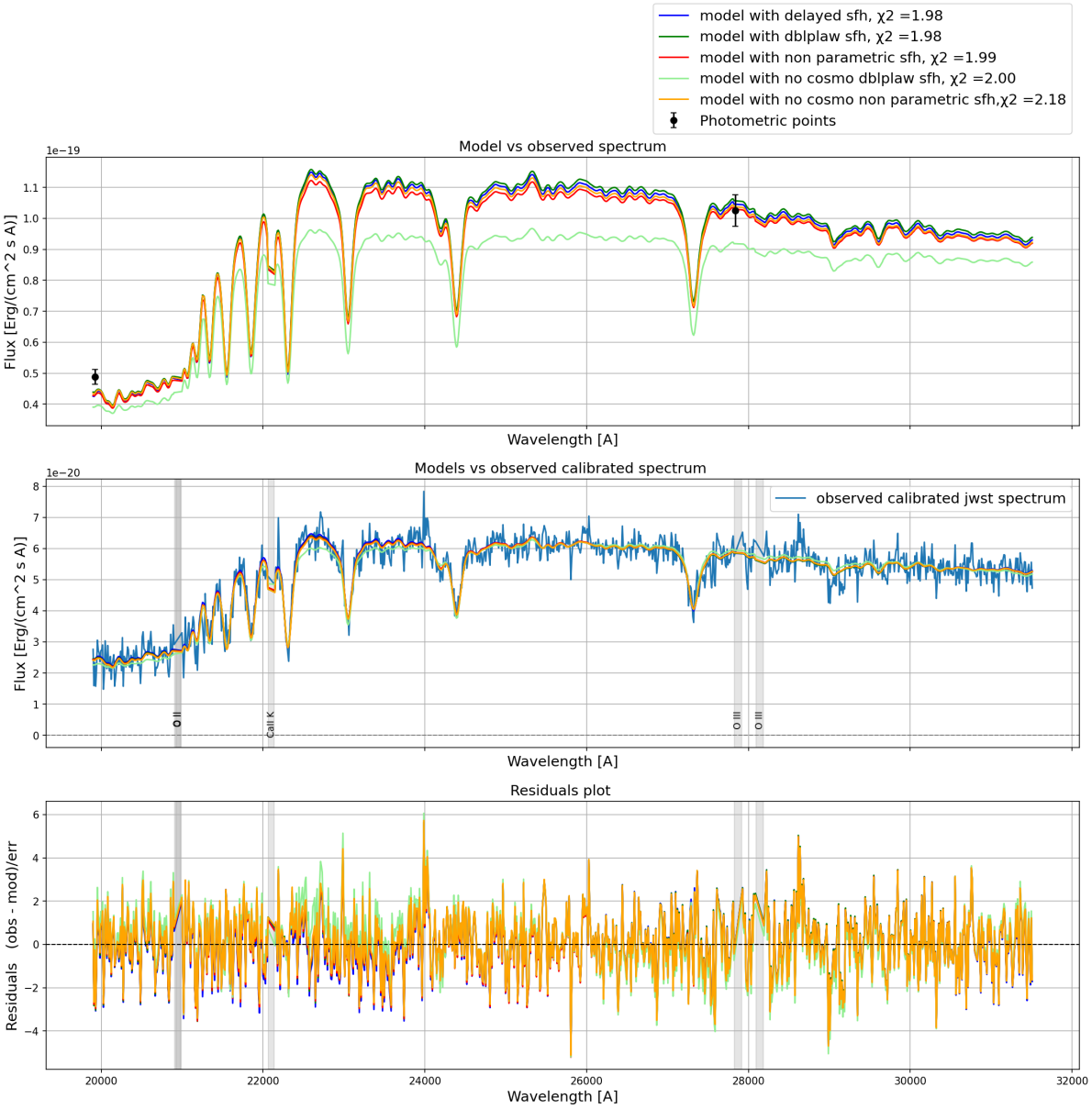

Figure C.5: Same as Fig. C.1.

Galaxy 55410

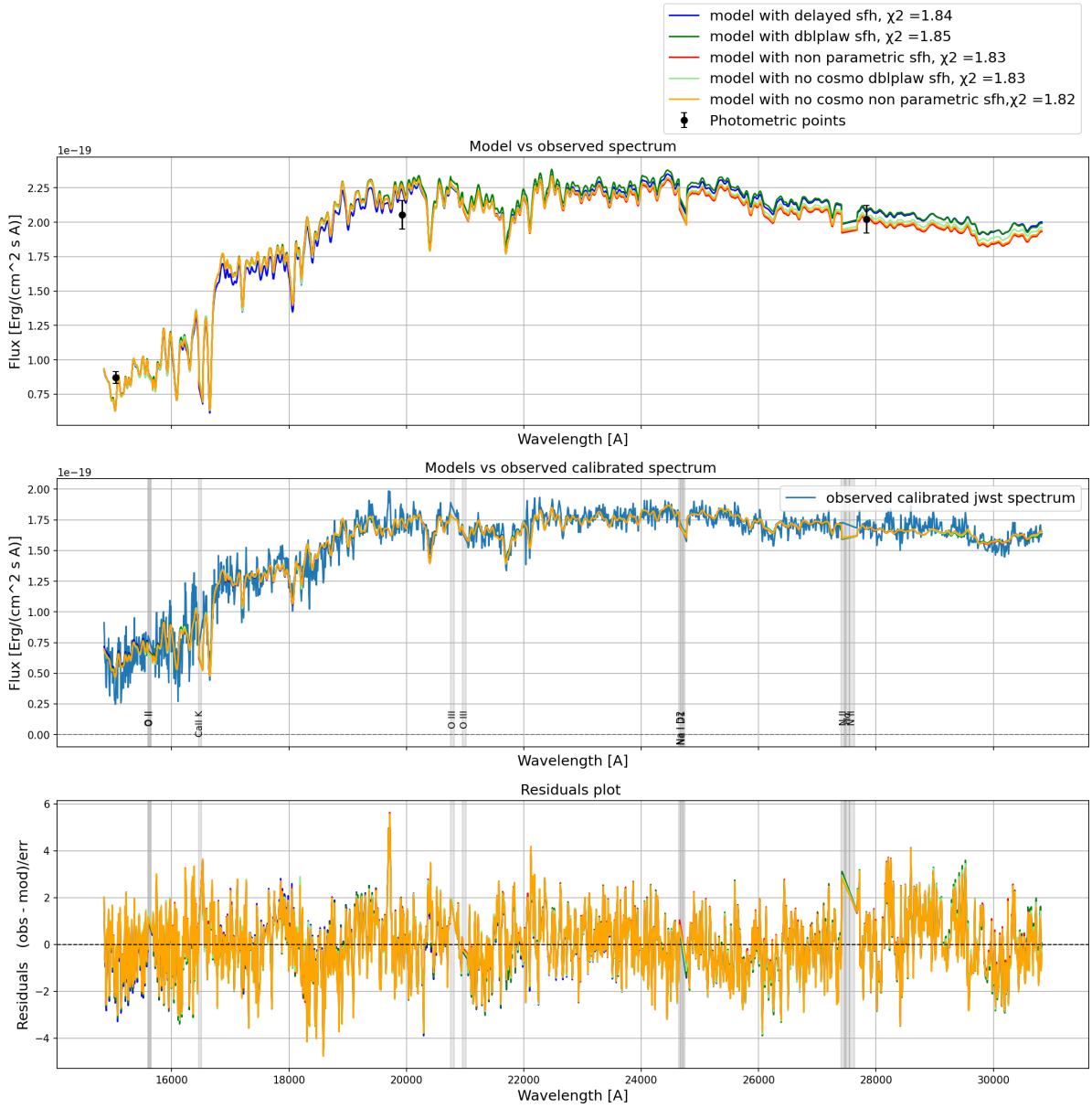

Figure C.6: Same as Fig. C.1.

Galaxy 7549

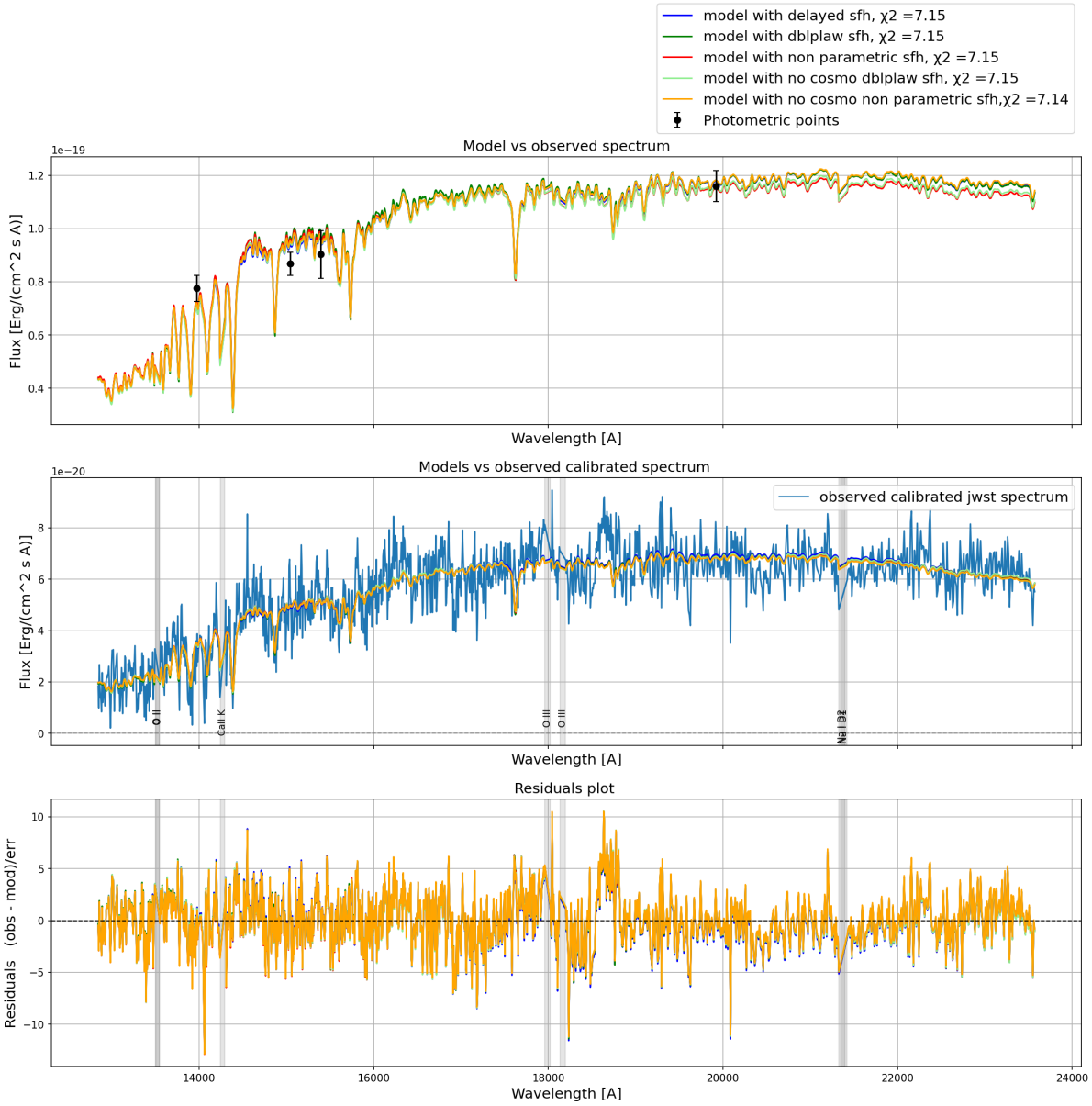

Figure C.7: Same as Fig. C.1.

Bibliography

Shadab Alam, Metin Ata, Stephen Bailey, Florian Beutler, Dmitry Bizyaev, Jonathan A Blazek, Adam S Bolton, Joel R Brownstein, Angela Burden, Chia-Hsun Chuang, et al. The clustering of galaxies in the completed sdss-iii baryon oscillation spectroscopic survey: cosmological analysis of the dr12 galaxy sample. *Monthly Notices of the Royal Astronomical Society*, 470(3):2617–2652, 2017.

Ivan K. Baldry, Karl Glazebrook, Joss Bland-Hawthorn, Michael R. Beasley, Richard J. Ellis, Carlton M. Baugh, Shaun Cole, and Carlos S. Frenk. Quantifying the bimodal color–magnitude distribution of galaxies. *The Astrophysical Journal*, 2004.

M. Borghi, F. Belfiore, R. L. Davies, et al. Pylick: A python package to measure lick indices from galaxy spectra. *Astronomy and Computing*, 43:101629, 2023. doi: 10.1016/j.ascom.2023.101629.

Alessandro Bressan, Paola Marigo, Léo Girardi, Bernardo Salasnich, Chiara Dal Cero, Stefano Rubele, and Ambra Nanni. Parsec: stellar tracks and isochrones. *Monthly Notices of the Royal Astronomical Society*, 2012.

Dillon Brout, Dan Scolnic, Brodie Popovic, Adam G Riess, Anthony Carr, Joe Zuntz, Rick Kessler, Tamara M Davis, Samuel Hinton, David Jones, et al. The pantheon+ analysis: cosmological constraints. *The Astrophysical Journal*, 938(2):110, 2022.

James S Bullock and Michael Boylan-Kolchin. Small-scale challenges to the λ cdm paradigm. *Annual Review of Astronomy and Astrophysics*, 55(1):343–387, 2017.

D. Calzetti, L. Armus, R. C. Bohlin, A. L. Kinney, J. Koornneef, and T. Storchi-Bergmann. The dust content and opacity of actively star-forming galaxies. *The Astrophysical Journal*, 533:682–695, 2000. doi: 10.1086/308692.

Michele Cappellari. Structure and kinematics of early-type galaxies from integral field spectroscopy. *Annual Review of Astronomy and Astrophysics*, 54:597–665, 2016. doi: 10.1146/annurev-astro-082214-122432. URL `https://doi.org/10.1146/annurev-astro-082214-122432`.

Michele Cappellari and Eric Emsellem. Parametric recovery of line-of-sight velocity distributions from absorption-line spectra of galaxies via penalized likelihood. *Publications of the Astronomical Society of the Pacific*, 2004.

A. C. Carnall, J. Leja, B. D. Johnson, R. J. McLure, J. S. Dunlop, and C. Conroy. Inferring the star formation histories of quiescent galaxies with bagpipes. *Monthly Notices of the Royal Astronomical Society*, 2018.

A. C. Carnall et al. A massive quiescent galaxy at z = 4 with suppressed star formation driven by an agn outflow. *Nature*, 627:295–299, 2024a. doi: 10.1038/s41586-023-06158-6.

AC Carnall, F Cullen, RJ McLure, DJ McLeod, R Begley, CT Donnan, JS Dunlop, AE Shapley, K Rowlands, O Almaini, et al. The jwst excels survey: too much, too young, too fast? ultra-massive quiescent galaxies at 3< z< 5. *Monthly Notices of the Royal Astronomical Society*, 534(1):325–348, 2024b.

Adam C Carnall, Ross J McLure, James S Dunlop, Derek J McLeod, Vivienne Wild, Fergus Cullen, Dan Magee, Ryan Begley, Andrea Cimatti, Callum T Donnan, et al. A massive quiescent galaxy at redshift 4.658. *Nature*, 619(7971):716–719, 2023.

Dan P Carson and Robert C Nichol. The age–redshift relation for luminous red galaxies in the sloan digital sky survey. *Monthly Notices of the Royal Astronomical Society*, 408(1):213–233, 2010.

Daniel P. Carson, Harald Kuntschner, and Roger L. Davies. A robust method to correct lick indices for velocity dispersion. *Monthly Notices of the Royal Astronomical Society*, 408(4):2339–2351, 2010. doi: 10.1111/j.1365-2966.2010.17293.x.

C. M. Casey et al. Cosmos-web: The largest contiguous jwst nircam survey. *ApJ*, 951 (1):L43, 2023. doi: 10.3847/2041-8213/acd09b.

R. Cid Fernandes, A. Mateus, L. Sodré, G. Stasińska, and J. M. Gomes. Semi-empirical analysis of sloan digital sky survey galaxies – i. spectral synthesis method. *Monthly Notices of the Royal Astronomical Society*, 2005.

A. Cimatti, E. Daddi, and A. Renzini. Mass downsizing and 'top-down' assembly of early-type galaxies. *AA*, 453:L29, 2006.

Andrea Cimatti, Filippo Fraternali, and Carlo Nipoti. *Introduction to galaxy formation and evolution*. Cambridge University, 2020.

Planck Collaboration. Planck 2018 results. vi. cosmological parameters. *Astronomy & Astrophysics*, 641:A6, 2020. doi: 10.1051/0004-6361/201833910.

C. Conroy and P. G. van Dokkum. The stellar initial mass function in early-type galaxies from absorption line spectroscopy. ii. results. *The Astrophysical Journal*, 2012.

Charlie Conroy. Modeling the panchromatic spectral energy distributions of galaxies. *Annual Review of Astronomy and Astrophysics*, 51(1):393–455, 2013.

Charlie Conroy, Alexa Villaume, Pieter van Dokkum, and Karin Lind. Absorption line fitter (alf): Detailed stellar population and abundance modeling. *The Astrophysical Journal*, 2018.

L. L. Cowie, A. Songaila, E. M. Hu, and J. G. Cohen. New insight on galaxy formation and evolution from keck spectroscopy of the hawaii deep fields. *AJ*, 112:839, 1996.

A. de Graaff et al. Rubies: Revealing unseen bright infrared-excess sources with jwst. *Astronomy Astrophysics*, 2025.

Anna de Graaff, David J Setton, Gabriel Brammer, Sam Cutler, Katherine A Suess, Ivo Labbe, Joel Leja, Andrea Weibel, Michael V Maseda, Katherine E Whitaker, et al. Efficient formation of a massive quiescent galaxy at redshift 4.9. *arXiv preprint arXiv:2404.05683*, 2024.

Scott Dodelson and Fabian Schmidt. *Modern cosmology*. Elsevier, 2024.

James S. Dunlop, Ross J. McLure, Rebecca J. Bowler, Baptiste Schuler, Caroline S. Straatman, William R. Cowley, Fergus Cullen, Hanae Inami, John S. Kartaltepe, Kristan Boyett, Márió Molnár, William I. Clarkson, and the PRIMER collaboration. PRIMER: Public Release IMaging for Extragalactic Research with JWST. *arXiv e-prints*, 2023.

S. Ekström, C. Georgy, P. Eggenberger, et al. Grids of stellar models with rotation i. models from 0.8 to 120 m at solar metallicity (z= 0.014). *Astronomy & Astrophysics*, 2012.

Eric Emsellem, Michele Cappellari, Davor Krajnović, Richard M. McDermid, Nicholas Scott, Anne-Marie Weijmans, et al. The atlas3d project – iii. a census of the stellar angular momentum in early-type galaxies: unveiling the distribution of fast and slow rotators. *Monthly Notices of the Royal Astronomical Society*, 414(2):888–912, 2011. doi: 10.1111/j.1365-2966.2011.18469.x. URL `https://doi.org/10.1111/j.1365-2966.2011.18469.x`.

Karl Glazebrook, Themiya Nanayakkara, Corentin Schreiber, Claudia Lagos, Lalitwadee Kawinwanichakij, Colin Jacobs, Harry Chittenden, Gabriel Brammer, Glenn G Kacprzak, Ivo Labbe, et al. A massive galaxy that formed its stars at z 11. *Nature*, 628(8007):277–281, 2024.

Nagisa Hiroshima et al. Semi-analytical frameworks for subhalos from the smallest to the largest scale. *arXiv preprint*, 2023. Preprint available at `https://arxiv.org/abs/2301.XXXXX`.

Edwin Hubble. A relation between distance and radial velocity among extra-galactic nebulae. *Proceedings of the national academy of sciences*, 15(3):168–173, 1929.

K. Ito et al. Deepdive: A jwst survey of massive quiescent galaxies at z $>$ 3. *arXiv preprint*, 2025.

Kieran Iyer, Eric Gawiser, Henry C. Ferguson, Casey Papovich, Guillermo Barro, Lucia Guaita, S. M. Faber, Daniel Kocevski, Chien Koo, Pablo G. Pérez-González, Vimal Tilvi, Weijia Wang, Benjamin Weiner, and Stijn Wuyts. Robust constraints on the star formation histories of massive quiescent galaxies from the large early release science survey. *The Astrophysical Journal*, 870(2):L24, 2019. doi: 10.3847/2041-8213/aafefb.

Tianxing Jiao, Takahiro Morishita, Lara J. Furtak, Christina C. Williams, Steven L. Finkelstein, Xiaohui Wang, Leonardo Ferreira, Megan B. Bagley, Sandro Tacchella, Anton Koekemoer, L. Y. Aaron Yung, Allison Kirkpatrick, Casey Papovich, Norbert Pirzkal, Marcia Rieke, Christopher Willmer, and Stephen M. Wilkins. Cosmic Spring: The Star Formation Histories of Quiescent Galaxies at $z < 0.5$. *The Astrophysical Journal Supplement Series*, 2023.

Andrea Lapi, Paolo Salucci, and Luigi Danese. Statistics of dark matter halos from the excursion set approach. *The Astrophysical Journal*, 772(2):85, 2013.

Joel Leja, Benjamin D. Johnson, Charlie Conroy, Pieter van Dokkum, and Nell Byler. Deriving physical properties from broadband photometry with prospector. *The Astrophysical Journal*, 2017.

Amanda J Moffett, Stephen A Ingarfield, Simon P Driver, Aaron SG Robotham, Lee S Kelvin, Rebecca Lange, Uroš Meštrić, Mehmet Alpaslan, Ivan K Baldry, Joss Bland-Hawthorn, et al. Galaxy and mass assembly (gama): the stellar mass budget by galaxy type. *Monthly Notices of the Royal Astronomical Society*, 457(2):1308–1319, 2016.

M. Moresco, A. Cimatti, R. Jimenez, L. Pozzetti, and et al. Improved constraints on the expansion rate of the universe up to z 1.1 from the spectroscopic evolution of cosmic chronometers. *Journal of Cosmology and Astroparticle Physics*, 2012.

Michele Moresco. Measuring the expansion history of the universe with cosmic chronometers. *arXiv preprint arXiv:2412.01994*, 2024.

Lauro Moscardini. Cosmology notes, 2023.

Stella S. R. Offner, Paul C. Clark, Patrick Hennebelle, Nathan Bastian, Matthew R. Bate, Philip F. Hopkins, Estelle Moraux, and Anthony P. Whitworth. The origin and universality of the stellar initial mass function. *ArXiv e-prints*, 2013.

Jieun Park, Charlie Conroy, Alexa Villaume, Benjamin D. Johnson, Phillip Cargile, Katherine A. Suess, and Benjamin D. Johnson. The next generation of stellar population synthesis models. iii. spectral models with variable abundance patterns. *The Astrophysical Journal*, 959(1):33, 2024a. doi: 10.3847/1538-4357/ad2ebf. URL `https://doi.org/10.3847/1538-4357/ad2ebf`.

Minjung Park, Sirio Belli, Charlie Conroy, Benjamin D Johnson, Rebecca L Davies, Joel Leja, Sandro Tacchella, J Trevor Mendel, Chloë Benton, Letizia Bugiani, et al. Widespread rapid quenching at cosmic noon revealed by jwst deep spectroscopy. *The Astrophysical Journal*, 976(1):72, 2024b.

Saul Perlmutter, Greg Aldering, Gerson Goldhaber, Robert A Knop, Peter Nugent, Peter G Castro, Susana Deustua, Sebastien Fabbro, Ariel Goobar, Donald E Groom, et al. Measurements of ω and λ from 42 high-redshift supernovae. *The Astrophysical Journal*, 517(2):565, 1999.

Francesco Lucchin Peters Coles. *Cosmology The Origin and Evolution of cosmic structure*. Wiley, 2003.

Adam G Riess, Alexei V Filippenko, Peter Challis, Alejandro Clocchiatti, Alan Diercks, Peter M Garnavich, Ronald L Gilliland, Craig J Hogan, Saurabh Jha, Robert P Kirshner, et al. Observational evidence from supernovae for an accelerating universe and a cosmological constant. *The Astronomical Journal*, 116(3):1009, 1998.

Adam G Riess, Wenlong Yuan, Lucas M Macri, Dan Scolnic, Dillon Brout, Stefano Casertano, David O Jones, Yukei Murakami, Gagandeep S Anand, Louise Breuval, et al. A comprehensive measurement of the local value of the hubble constant with 1 km s- 1 mpc- 1 uncertainty from the hubble space telescope and the sh0es team. *The Astrophysical journal letters*, 934(1):L7, 2022.

S. Salim, M. Boquien, and J. C. Lee. Dust attenuation curves in the local universe: Demographics and new laws for star-forming galaxies and high-redshift analogs. *The Astrophysical Journal*, 859(1):11, 2018. doi: 10.3847/1538-4357/aabfdf.

Kevin Schawinski, C Megan Urry, Brooke D Simmons, Lucy Fortson, Sugata Kaviraj, William C Keel, Chris J Lintott, Karen L Masters, Robert C Nichol, Marc Sarzi, et al. The green valley is a red herring: Galaxy zoo reveals two evolutionary pathways towards quenching of star formation in early-and late-type galaxies. *Monthly Notices of the Royal Astronomical Society*, 440(1):889–907, 2014.

Charles L Steinhardt, Peter Capak, Dan Masters, and Josh S Speagle. The impossibly early galaxy problem. *The Astrophysical Journal*, 824(1):21, 2016.

Sandro Tacchella, Benjamin D. Johnson, Brant E. Robertson, Alicia C. Carnall, Rohan Endsley, Desika Narayanan, and et al. Jwst/nircam+nirspec: Interstellar medium and stellar populations of young galaxies with rising star formation and evolving gas reservoirs. *The Astrophysical Journal Letters*, 927:L17, 2022. doi: 10.3847/2041-8213/ac4b1e.

D. Thomas, C. Maraston, and R. Bender. Stellar population models of lick indices with variable element abundance ratios. *Monthly Notices of the Royal Astronomical Society*, 2003.

D. Thomas, C. Maraston, R. Bender, and C. Mendes de Oliveira. The epochs of early-type galaxy formation as a function of environment. *ApJ*, 621:673, 2005.

D. Thomas, C. Maraston, and J. Johansson. Flux-calibrated stellar population models of lick indices with variable element abundance ratios. *Monthly Notices of the Royal Astronomical Society*, 2011a.

Daniel Thomas, Claudia Maraston, and Jonas Johansson. Flux-calibrated stellar population models of lick absorption-line indices with variable element abundance ratios. *Monthly Notices of the Royal Astronomical Society*, 412(4):2183–2198, 2011b.

Livia Tomasetti, Raphael Gobat, Victoria Strait, Lorenzo Franco, Yuchen Zhou, Francesco Valentino, Andrea Cimatti, Arti Saxena, Linhua Jiang, Fabio Loiacono, Jingwen Wu, and Haojing Yan. Testing Galaxy Evolution Models with JWST: Quiescent Galaxies at $z = 2{-}4$. *Astronomy & Astrophysics*, 2023.

A. Vazdekis, P. Coelho, S. Cassisi, E. Ricciardelli, and et al. Evolutionary stellar population synthesis with miles - ii. scaled-solar and -enhanced models. *Monthly Notices of the Royal Astronomical Society*, 2015.

C. J. Walcher, B. Groves, R. Cid Fernandes, and N. M. F. Schreiber. Fitting the integrated spectral energy distributions of galaxies. *Astrophysics and Space Science*, 331: 1–52, 2011. doi: 10.1007/s10509-010-0585-0.

G. Worthey. Comprehensive stellar population models and the disentanglement of age and metallicity effects. *The Astrophysical Journal Supplement Series*, 1994.

G. Worthey and D. L. Ottaviani. H and h absorption features in stars and stellar populations. *The Astrophysical Journal Supplement Series*, 1997.

Po-Feng Wu. Agn-driven outflow shuts down star formation in a $z = 4$ recently quenched galaxy. *arXiv preprint arXiv:2409.00471*, 2024.